Università degli Studi di Padova
Dipartimento di Ingegneria Civile, Edile ed Ambientale
Corso di Laurea Specialistica in Ingegneria Civile
Indirizzo Strutture

Tesi di Laurea

Damage Tolerant Strengthening based on Engineered Cementitious Composites and Super-Elastic Reinforcement

Relatori:
Università di Padova: **Prof. Ing. Carlo Pellegrino**
Universidade do Minho: **Prof. Ing. Eduardo Pereira**

Laureando: **Dario Mirza**
Matricola: 105845

Anno Accademico: 2014/15

Acknowledgments

Eu queria agradecer em primeiro lugar ao meu coordenador, Prof. Eduardo Pereira, pela grande disponibilidade e encorajamento do meu trabalho durante estes 7 meses e pelos inúmeros conselhos e ideias inovadoras.
Também queria agradecer ao Eng. João Almeida por toda a ajuda no laboratório, nomeadamente na produção, corte, retificação e teste das amostras e aprendizagem na utilização do equipamento.
Aos técnicos Sr. Matos, Sr. Marco, Sr. Carlos, Sr. Pokee, Sr. Cesar e Sr. Edgar por toda a ajuda durante o meu trabalho no laboratório.
Por último, queria agradecer também a todos os estudantes e pessoas de Guimarães e Braga que me ajudaram durante o meu período de Erasmus.

Summary

Seismic actions, in some regions of the world, are critical in the design process of structures. However, a large number of structures have been constructed according to design codes that were based in excessively simplified approaches to seismic action. These structures, which include for example bridges built before 1970, may require retrofitting operations. By considering all the retrofitting approaches already developed in the past decades, including for example the strengthening, the increasing of the displacement capacity and the limitation of the seismic force by the response modification, this research focuses on the first two approaches and investigates new strategies based on the combination of two innovative materials: Engineered Cementitious Composites and Shape Memory Alloys.

ECC is a family of cementitious materials containing PVA fibers that can be designed to develop a tensile strain-hardening behaviour in tension, by allowing the formation of multiple micro-cracks. With ECC it is possible not only to reach tensile strains between 3% and 6%, but also to increase the durability by decreasing crack widths and increasing damage tolerance.

SMAs are a family of alloys that, depending on the temperature at which the load is applied, may show the Shape Memory Effect or the Super-Elastic Effect. The Shape Memory Effect allows the material to recover the initial shape, even after undergoing large deformations, through the heating of the material until a characteristic temperature is reached. In contrast, the Super-Elastic effect allows the material to undergo very large deformations, up to 6% strain, in the elastic region.

In this research one ECC mixture that can reach 5% strain in direct tension has been developed and characterized in tension, compression and flexure. A Super-elastic Nitinol has been also characterized in order to develop a composite that could be used for strengthening or designing structural elements. The hybrid composite resulting from the combination of the previous two materials has been also tested in direct tension considering two different volume percentages of Nitinol reinforcement. The first composite, that included smooth Nitinol wires at a volumetric percentage of 0,47%, underperformed the original unreinforced ECC due to the low adherence between the Nitinol and the matrix, that has been confirmed by a series pull-out tests. The second composite, that included twisted wires at a percentage of 0,94% in volume, showed an increase of the tensile strength and the ultimate strain exceeded 3,5%. This last hybrid composite showed also the ability to recover most of the accumulated deformation for large displacements. Finally, this hybrid composite was compared with a typical reinforced concrete solution, in a model example that simulated the seismic action on two scaled model columns. The hybrid composite solution showed greater strength, greater displacement capacity, the ability to recover accumulated deformations and a high damage tolerance in the regions where the structural elements experience the largest deformations.

In general, it was possible to conclude that the combination of the two innovative materials studied in this research can result in new and very efficient strategies both for the strengthening of existing structures and the design of new structures subjected to extreme events.

Index

List of Figures

List of Tables

1. Introduction

1.1 General Overview

An important field of civil engineering deals with the *design* of constructions subjected to horizontal loading, in particular the *seismic action* that in some regions of the world can be determinant in the design of structural elements. A large number of existing constructions were designed before the development of a reliable design code dealing with seismic action, which guarantees an ultimate level of serviceability and resistance after seismic events. Therefore, most of these constructions require *retrofitting* or replacement [1].

In the case of *bridges* this topic assumes special relevance, because these special structures have to remain usable after catastrophic events due to their important role in transportation and connection in general. In addition, bridges normally have limited redundancy in their structural system so, if a structural element or a connection fails, all the structure may collapse. It is possible to find in the recent decades some examples of bridges that didn't perform well under seismic action, mostly in California, Japan and South America. These examples justify the need to increase the research on the prediction of the behaviour of structures under seismic loading and on better understanding the involved collapse mechanisms [3].

Considering all the structural elements of the bridge, the *column* is the one that needs more attention. Bridge columns assume a particularly relevant role in the transversal behaviour of the structure, their stiffness and ductility influence directly the forces and displacements occurring in the bridge during seismic events.

Seismic retrofitting of old bridges is generally more challenging than the design of new bridges. Nevertheless the need for bridge retrofitting towards the fulfilment of the new design code requirements has led to the increase of the scientific knowledge about the retrofitting techniques, mostly during the last 30 years. Seismic retrofitting also presents various restrictions which determine the level up to which a bridge can be retrofitted: the need to retrofit the structure in a short period to avoid the suspension of the traffic, the impossibility or difficulty to replace or alter the main structural component, and the costs associated with the retrofitting operations, that sometimes can exceed the costs of the construction of a new bridge. All these restrictions sometimes require the validation of new construction methods and the use of innovative high performance materials, as an alternative to the use of common retrofitting techniques. Examples of such techniques include the increase of the resistance of the piles with steel reinforcements, the increase of the reinforced concrete sections, the use of carbon fibre reinforced polymers (FRP) reinforcements, plastic reinforcement, glass FRP (GFRP) reinforcements or precast concrete jacketing [1].

At the level of the structural behaviour, two interesting alternative strategies were developed with the aim of protecting the bridge's columns during the seismic action and avoiding their excessive damage or failure. The first one consists on modifying artificially the first period of vibration of the structure, by increasing it with specific isolating devices positioned between the piers and the deck. These devices also isolate the columns from the deck and reduce the acceleration applied to the deck's masses. The second strategy consists on increasing the energy dissipation capacity during the seismic event with devices that provide supplemental damping to the structure. These devices reduce the plastic displacement of the piers and concentrate the energy dissipation at the level of the columns. After the seismic event it is possible to replace these devices. These *isolators* and *dissipators* can be used both in the design of new bridges and in retrofitting of existing bridges in order to protect the structural elements subjected to future seismic actions.

Typical retrofit approaches include the strengthening and the increasing of the displacement capacity of the deficient structural elements. In the case of the columns in bridges, this is possible to achieve for example by jacketing the damaged or deficient column, selecting the materials to be applied among a series different options. Steel and Fiber-Reinforced Polymers are commonly used to retrofit bridges and other structures, but also glass or ceramic based materials are used. All these materials, if applied correctly, are able to improve the performance of the retrofitted elements by exploiting their high stiffness and strength, especially in the *elastic* tensile regime. Following these two retrofit approaches, in this thesis new retrofit techniques will be studied, based on replacing the use of common retrofit materials with the recently developed cementitious composites that can undergo high tensile deformations while preserving the integrity of the structural elements.

1.2 Objectives

The objectives of this thesis are several and include:

- The study the *behaviour of ECC,* which is a *strain-hardening cementitious material*, by designing its composition aiming at increasing the properties of structural elements.
- The study and test the tensile behaviour of *Nitinol*, a Shape-Memory Alloy, which presents two characteristic and different tensile behaviours depending on the temperature at which the loading is applied: *shape memory effect* and *super-elastic effect*.

These two innovative materials will be combined in order to obtain two *hybrid composites* that exhibit strain-hardening in tension and shape recovery features.

The third objective is to *characterize in tension* the properties of these composites, and study the behaviour of the composite at the level of the interface. In the end, one of these composites will be *compared* with the common steel reinforced concrete in order to distinguish and quantify the advantages of its application in the design and retrofit of bridges and buildings.

1.3 Structure of the Thesis

This thesis includes seven chapters. The *first chapter* presents a general overview of the seismic action hazard in existing and newly designed bridges, introducing the existing retrofit strategies and defining the objectives of this thesis.

The *second chapter* focus on the performance of the bridges piers during the past earthquakes, presenting some examples of damaged piers and exploring the typical deficiencies and failure mechanisms occurring during seismic events, as well as presenting some retrofit approaches and strategies that have been already used in the past.

The *third chapter* includes the state-of-the-art on Engineered Cementitious Composites, exploring their physical properties, their mechanical features and presenting some retrofit applications already studied by other researchers.

The *fourth chapter* presents the state-of-the-art on Shape Memory Alloys and in particular on Nitinol alloy, showing how the shape-memory and super-elastic effects could be used in structural applications.

In the *fifth chapter*, ECC and a Shape Memory Alloys are tested: ten ECC mixtures developed are tested in direct tension in order to select the one that shows better tensile properties. Subsequently this mixture is characterized in direct tension in more detail, as well as in compression and flexure. Two different Nitinol wires are also characterized in direct tension.

In the *sixth chapter* two hybrid composites that combine ECC matrix and Nitinol reinforcement are developed and characterized in direct tension, considering both monotonic and cyclic loading. Pull-out tests are also conducted in order to characterize the adherence between these two materials. In the end two scaled model columns were produced, one with steel reinforced concrete and one with one of the hybrid composites developed. These models were tested in order to assess and quantify their performance under cyclic loading.

The last chapter includes a summary of the results obtained and the final conclusions, trying to present the future perspectives for the strategies explored and discussing how the characteristics of the hybrid composites studied could be improved envisaging their application in civil engineering problems.

2. Seismic Retrofit of Bridge Columns

2.1 Performance of Bridge Columns during past Earthquakes

Bridges built before 1971 San Fernando earthquake typically contain insufficient percentages of reinforcements in transverse direction (0,2% or less), according to the elastic design philosophy adopted for seismic design of bridges prior to 1970. In the US there are 575000 bridges and 60% of them were built before 1970. The main faults in this approach were:

- A low seismic design force that led to an under-estimation of the seismic deflection.
- An incorrect ratio between gravity and the seismic design load.
- The absence of a concept of ductility and capacity design, that are crucial to the inelastic response of non-redundant systems.
- A low confinement of concrete in reinforced concrete (RC) column. In fact the codes allowed a distance between the stirrups of 30 cm.

All these design insufficiencies caused undesirable flexural and shear behaviour that led to catastrophic collapse of the columns in many cases.

As an example, during the *San Fernando earthquake* (6.6 magnitude on 9 February 1971 in Sylmar, California) [2, 3, 4] more than 60 bridges have been damaged or collapsed due to the excessive damage on RC columns. The retrofitting costs exceeded 100 million dollars. In the figure 2.1 is possible to observe a RC column on Interstate 5, that due to *inadequate transversal reinforcement*, was severely damaged with a *buckling of the longitudinal reinforcement* in the plastic hinge.

Figure 2.1: Damaged reinforced concrete column during San Fernando earthquake in 1971 [2].

On October 1989, *Loma Prieta earthquake* (in California) [2, 4] reached a magnitude of 6.9 and devastated several buildings and 80 transportation infrastructures including two major bridges in California. The collapse of the Cypress Street Viaduct caused the death of 42 people. The repairing costs reached 1,8 billion dollars. In the figures 2.2, 2.3 and 2.4 it is possible to observe the typical failure mode of RC columns due to insufficient transversal reinforcement, that caused also the collapse of the upper deck of the structure.

Figure 2.2: Cypress Street Viaduct of Interstate 880 [2].

Figure 2.3: Failure at the bottom of a RC column after Loma Prieta earthquake, 1989[3].

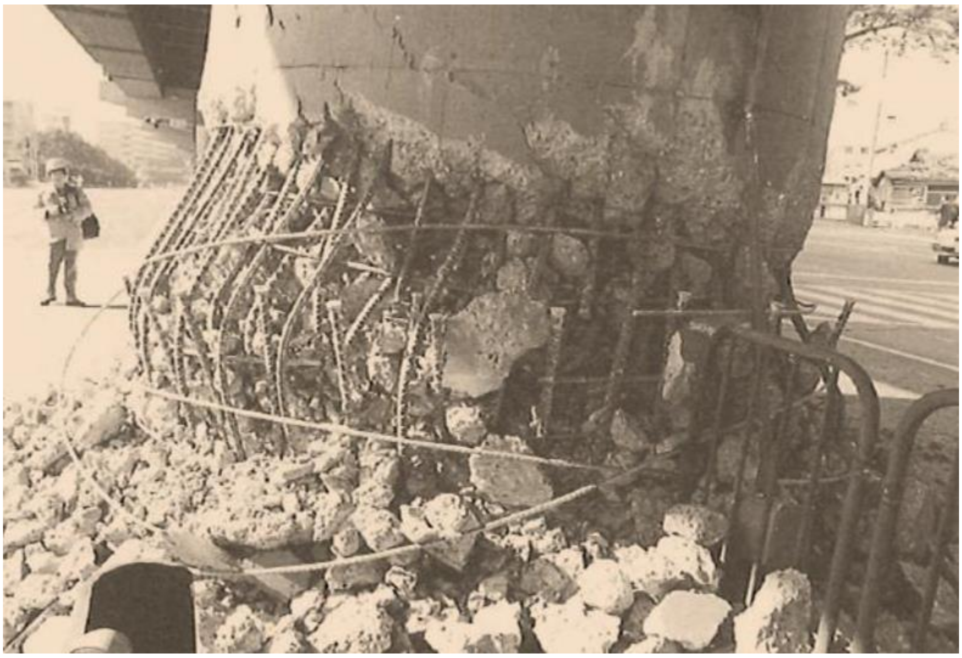

Figure 2.4: Failure at the base of a column after Loma Prieta earthquake, 1989 [3].

Northridge earthquake occurred in 1994 in California [2], near the city of Los Angeles, with a magnitude of 6.7 and a duration of the main shock of about 45 seconds. This earthquake caused the death of 72 people, affecting more than 2000 bridges, 6 of them collapsed and 4 were strongly damaged. The damages caused by this earthquake costed 20 billion dollars (40 times more than the cost due to the damages of 1971 earthquake). The main reason for the failures was the low percentage of transverse reinforcement that caused the excessive damage of the plastic hinges. In figures 5 and 6 it is possible to observe one example of buckling of RC columns and the collapse of a span due to the failure of a column.

Figure 2.5: RC columns under the Valley Freeway in 1994 [2].

Figure 2.6: Span collapsed at the Golden State- Antelope Valley interchange collectors, due to the collapse of a column [3, 4].

A 6.8 magnitude earthquake devastated the area of Kobe and Osaka (Japan) on 17 January 1995 [2]. This earthquake caused the death of 55.000 people and several important highways were damaged or collapsed entirely. Most of the damage occurred at the bottom of the column (in the plastic hinge region), due to the lack of sufficient transversal reinforcement. In figures 2.7 and 2.8 it is possible to observe one example of a bridge collapsed with its columns damaged after the Kobe earthquake.

Figure 2.7: Hanshin Expressway [3].

Figure 2.8: Flexural failure due to lack of confinement at the bottom of RC piers in Kobe earthquake, 1995 [3].

On 23 October 2004 Niigata-Ken Chuetsu earthquake hit with a 6.9 magnitude the lands of Japan [2], several highways, buildings and houses, which were destroyed or damaged, in many cases due to the lack of flexural ductility of RC columns. In figure 2. 9 is possible to observe one example of a damaged column.

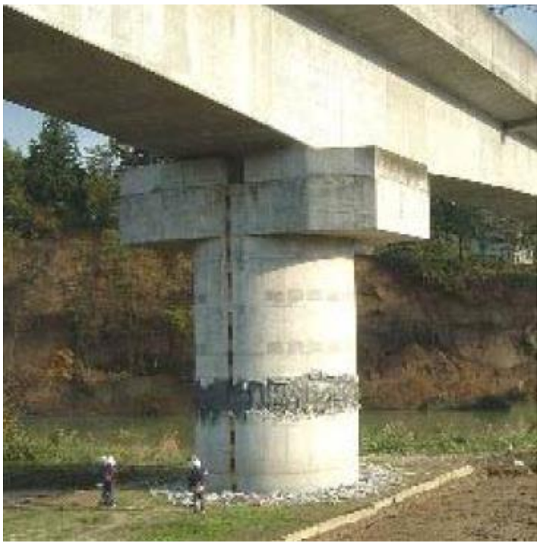

Figure 2.9: Damaged RC column of Unogawa Bullet Train Bridge [2].

Wenchuan earthquake hit China on 12 May 2008 [4], with a magnitude of 8.0 causing 69.146 death and 374.072 injuries. It was the most catastrophic event since 1976. The government spent 146.5 billion dollars during the following three years to rebuild the areas ravaged by the earthquake. In figure 2.10 it is possible to observe the damage on the plastic hinges of the columns and the relative displacement of the deck after this earthquake.

Figure 2.10: Damaged columns and relative displacements of joints on a bridge during Wenchuan earthquake [4].

On 27 February 2010 one of the 10 largest earthquakes in history occurred in the *Biobo* region of *Chile,* with a 8.8 magnitude [2]. The after-shock magnitude was greater than 5.0 and 521 people died. One example of a damaged bridge during this earthquake is the Juan Pablo II bridge showed in figure 2.11, exhibiting *shear failure of the columns* due to insufficient transverse reinforcement.

Figure 2.11: Juan Pablo II Bridge, shear failure of the columns [2].

2.2 Retrofit Approaches

When a bridge is seismically deficient, the optimal retrofit strategy should be found. A retrofit strategy consists of a plan for the seismic retrofit of a bridge and can include several approaches and measures. The retrofit *measures* consist on the physical modifications of a component of a bridge that have the objective of increasing the performance of the bridge when it becomes subjected to another future earthquake.

To select the best retrofit strategy it is necessary to confront the different strategies including not only the structural benefits, but also the costs, the aesthetics, the political and the environmental constrains. This complicated process includes:

- Detailed as-built evaluation. The goal of this step is to better understand the response of the bridge under a design seismic action, identifying the structural weak elements that could be object of retrofitting.
- Find alternative retrofit strategies. Normally it is possible to improve the seismic response of a the bridge in several ways. Therefore it is necessary to identify, in a preliminary stage, as many option as possible. Solutions that include high costs or other construction problems should be eliminated.
- Detailed evaluation of each viable retrofit strategy. This step includes preliminary design and preliminary costs estimation.
- Choose the best strategy by combining the contributions of the structural and the geotechnical engineering specialists, environmental and citizens groups, bridge owner, utility companies, state and government agencies. The retrofit decision should be documented in a report that should include all the as-built and preliminary calculations, costs estimation, conclusions and recommendations.

All the available retrofit approaches can be used alone or combined to develop a retrofit strategy. The common *approaches* used to develop a seismic retrofit operation are listed below:

- Strengthening
- Improvement of displacement capacity
- Force limitation by response modification
- Partial replacement

Strengthening is typically adopted to increase the moment capacity of the deficient structural elements. This approach has some consequences: it leads to the increase of the structural element stiffness and decrease the ductility demand on the retrofit component, increasing the force in the adjacent components.
The improvement of the *displacement capacity* can normally achieved in different ways: increase of the ductility capacity of columns, increasing of the ability to undergo large displacement without collapse or fracture; extending the length of the bearing seats to allow greater relative displacement at the bearing location without loss of support.
Is possible to obtain *force limitation* using sacrificial elements designed to yield during the seismic event. These elements are able to “protect” other elements reducing the applied force. One method consists on using isolation bearings, that can used as a “fuse” to limit the amount of shear force transmitted to the column.
The *modification of the dynamic response* consist in an increase of the fundamental period of the structure, that reduces the forces applied to the structure. This is possible by using isolators strategically positioned in the critical sections of the structure. However, the displacement demand may be very large. Energy dissipators and dampers could also be used to modify the dynamic response, improving the displacement capacity and reducing the strengthening necessity [5].

2.2.1 Strengthening and Improvement of Displacement Capacity

One of the most common strategies to increase the flexural strength of a column involves applying a *concrete layer* with additional reinforcing steel bars at the faces of the existing. An adequate number of dowels must also be provided in order to transfer the shear stresses between the existing column and the added concrete layer [5].

An alternative retrofit technique used to strengthened bridge piers consists on the use of *steel jacketing* to confine the existing reinforced concrete. The compressive stress-strain diagram for un-confined and confined concretes are presented in figure 2.12. This strategy contributes to increase the ultimate strength of the existing concrete and to increase the stiffness of the column in the strengthened region between 20% and 40%. The jacketing contributes to improve the ductility capacity of the column by eliminating the brittle shear mode of failure [4,5].

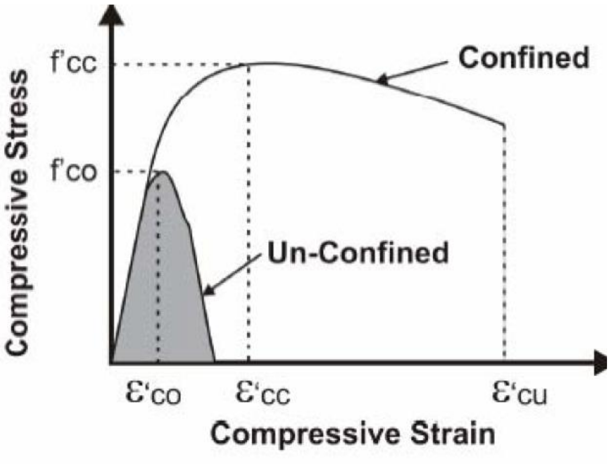

Figure 2.12: Stress-Strain diagram of confined and un-confined concrete.

An example of steel jacketing is presented in figure 2.13. In figure 2.14 it is also possible to observe the force-displacement diagram which is typically obtained RC columns with and without steel jacketing. The retrofitted column shows an increase of the resistance of low-confined or deteriorated pier through the confinement of the damaged concrete, reprising the original resistance or increasing the mechanical properties of the section; increasing the ductility and the dissipative capacity.

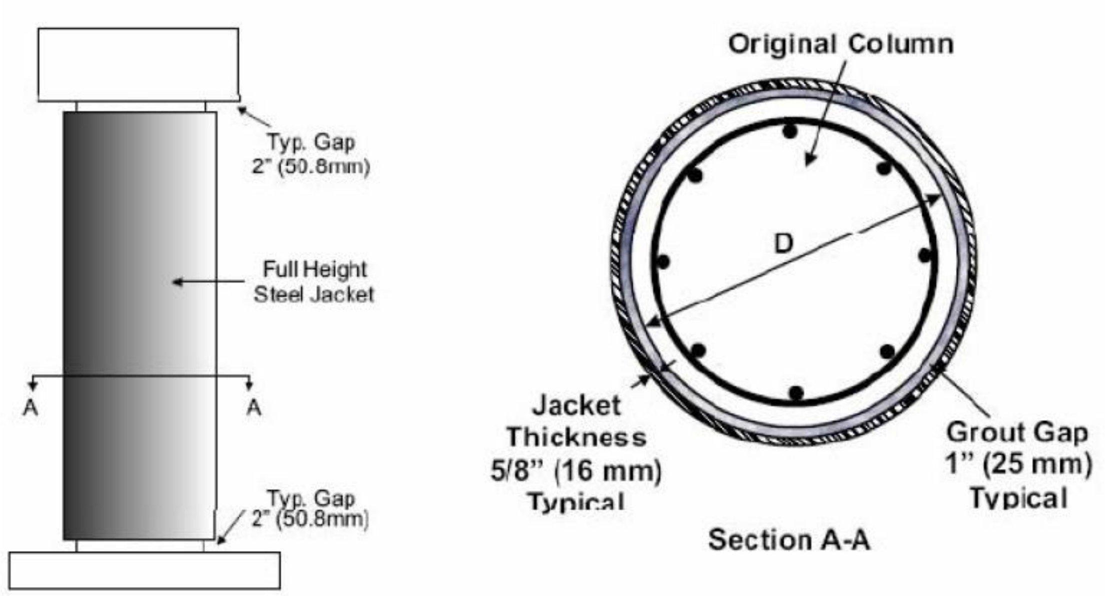

Figure 2.13: Example of steel jacketing [4].

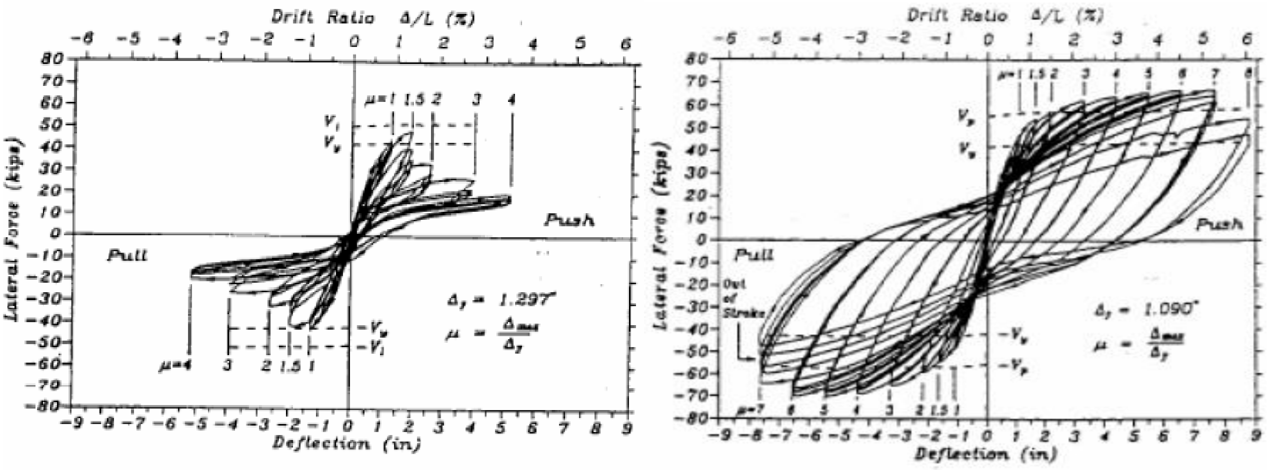

Figure 2.14: Load Force, Deflection Drift Ratio diagrams of a RC column, before and after steel jacket retrofit [4].

The retrofit techniques adopted in reinforced concrete piers include also the use of *Fibre-Reinforced Polymers (FRP) Jacketing*. Different types of materials with different mechanical properties can be used as jacketing, as is possible to observe in table 2.1. The advantages of this method include also the low costs of manpower and material lightness. In figures 2.15 and 2.16 some examples of retrofitted piers using fibre composites are shown.

Type of Fiber	Ultimate Strength, MPa (ksi)	Ultimate Strain	Modulus of Elasticity, GPa (ksi)
E-Glass	2410 (350)	0.020	41 (6,000)
S-Glass	3450 (500)	0.030	41 (6,000)
CF-Pan	4140 (600)	0.020	228 – 345 (33,000 – 50,000)
C-Pitch-GP	1380 (200)	0.003	41 (6,000)
Pitch UHM	2760 (400)	0.005	483 – 827 (70,000 – 120,000)
Aramid	3450 (500)	0.020	69 – 138 (10,000 – 20,000)
Ceramic	690 (100)	0.020	69 – 276 (10,000 – 40,000)
Nylon	345 (50)	0.050 – 0.500	3.5 (500)

Table 2.1: Mechanical properties of fibres used in modern fibre-reinforced plastic composites.[5].

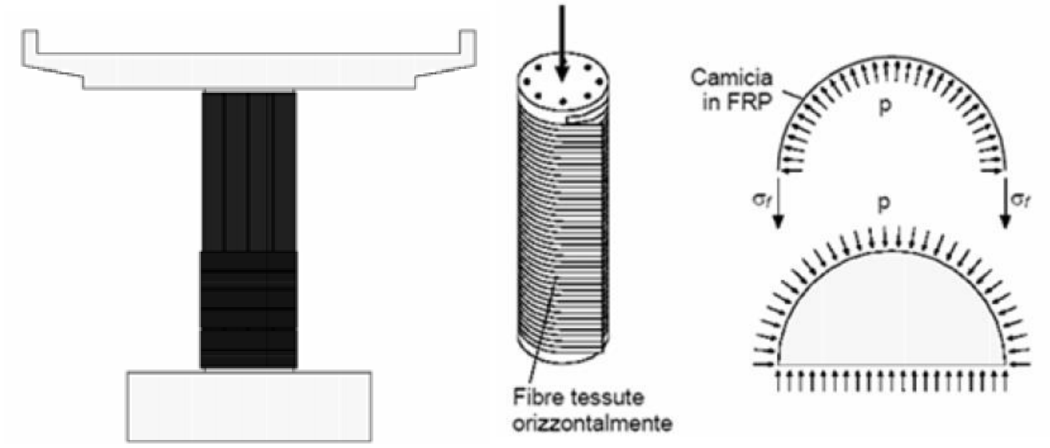

Figure 2.15: FRP retrofit technique [4]

Figure 2.16: Application of FRP [4].

Other methods to increase the strength and/or the ductility of existing piers include the use of:

- Pre-stressed high resistance steel wires wrapped around the column. These increase the lateral confinement and ductility with active pressure, as shown in figure 2.17.
- Supplemental shear walls casted in place between the columns. these increase the transversal capacity and prevent the formation of plastic hinges [4,5], as shown in figure 2.17.

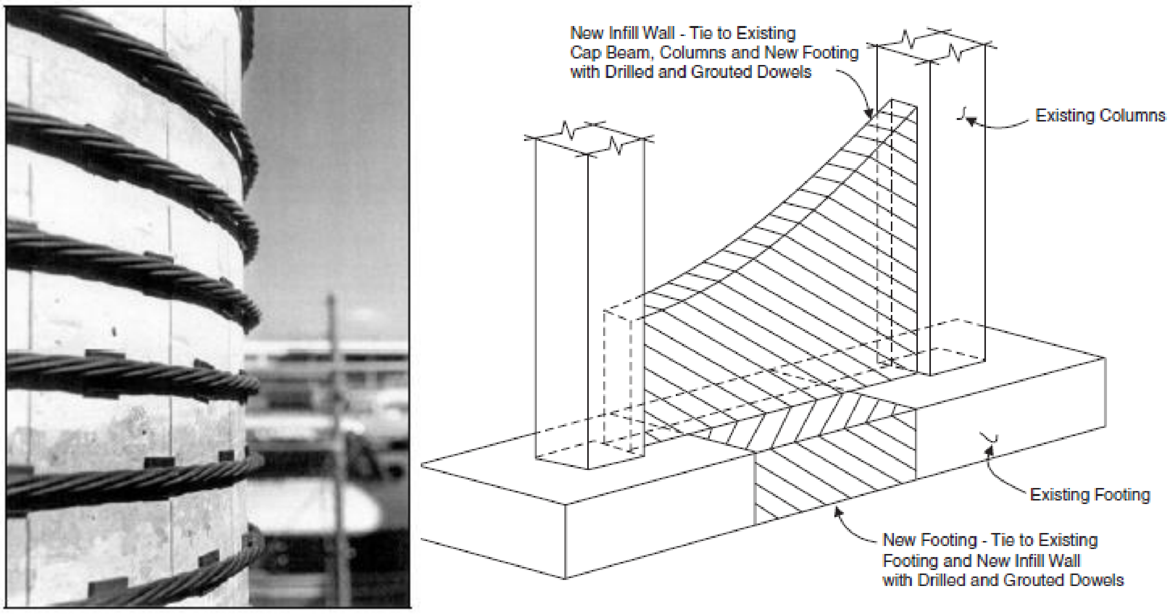

Figure 2.17: Retrofit methods based on pre-stressed steel wires and supplemental shear walls [5].

2.2.2 Force Limitation by Response Modification

The isolation of the column from the superstructure with *isolation bearing* has the dual benefit of replacing the vulnerable bearing and protecting the structural element from failure. By increasing the fundamental period of the structure it is possible to reduce the accelerations in the superstructure and the inertial forces transmitted to the substructures. These bearing should be stiff under service loads with a minimum amount of displacement, for example under wind loads, and flexible under seismic loads. This means that the force-displacement behaviour of these isolators must be non-linear. Currently, the most common isolator types are:

- Elastomeric: with or without lead core, with a non-linear or linear constitutive law.

- Sliders: characterized by high damping capacity and bi-linear behaviour.
- Viscous dampers: where the constitutive law depends on the velocity.
- Displacement dependent devices: linear or non-linear displacement dependent, normally used as bracings in the structures [5,6].

In figures 2.18 and 2.19 some examples of isolators and dissipators are shown.

Figure 2.18: Elastomeric isolation bearing and slider isolating bearing [6].

Figure 2.19: Viscous damper [6].

2.3 Conclusions

In the previous pages, a few of the most common approaches for seismic retrofitting of old or damaged buildings and bridges have been briefly discussed. As shown, all these techniques have in common the main objective of increasing the deformability of the structural elements, or to increase their tolerance to damage. The aim of the two subsequent chapters is to study alternative strategies that can lead to the increase of the efficiency of these approaches, by studying innovative retrofit methods based on two innovative materials: Engineered Cementitious Composites (ECC) and Shape Memory Alloys (SMA). ECCs consist of a family of cementitious composites that can undergo large deformations under tensile loads due to the formation of micro-cracks. The features of these innovative material are: ductility under tensile deformations, high durability and high tolerance to damage. SMAs are mostly special alloys that at low temperatures show shape memory effect, and at higher temperatures show super-elastic behaviour. In particular, the application of these materials in the regions where programmed plastic hinges will develop seems interesting, mostly in elements that need to undergo cycles of loading and unloading without excessive damage. The SMA features can help with the recovery of the initial position of elements subjected to large deformation. In the subsequent chapters these materials will be presented, with emphasis on the main properties and application already studied in the last decades.

Bibliography

[1] Ceb-Fip (2007); Seismic bridge design and retrofit – structural solutions, bulletin 39, ISSN 1562-3610.

[2] Moochul Shin (2012); Seismic retrofit and repair of reinforced concrete columns using shape memory alloy spirals, Ph.D Thesis, University of Illinois, pages 6-32.

[3] Maria Brando (2011); Seismic performance of bridges during Canterbury earthquakes, Politecnico di Milano, pages 17-30.

[4] Bruno Briseghella, Enzo Siviero (2009); Problematiche di adeguamento sismico nei ponti e nei viadotti, Slide from "Riabilitazione del costruito e adeguamento sismico" course, pages 1-43.

[5] Ian Buckle et al. (2006), Seismic Retrofitting Manual for Highway Structures: Part 1 – Bridges, PUBLICATION NO. FHWA-HRT-06 032, chapter 9: pages 337-397.

[6] A. Dusi, Base Isolation Devices and Systems (2012); Slide from "Aseismic design of building structures" course, dusi@dic.unipd.it, pages 1-15.

3. Innovative Seismic Strengthening Approaches using Cementitious Composites

3.1 Historical Development

The development of cementitious composite that can undergo tensile stresses has probably started in the 60's, with the work of Romauldi. He demonstrated the effectiveness of a cement composite that contained short steel fibres which reduced the brittleness of the concrete [1]. In the following years, different researches developed different composites that contained a large variety of different *fibre* types, such as glass, carbon, natural fibers and hybrids that combine either different fibre types or fibres with different lengths. The aim was to develop a material that could undergo high tensile stresses and/or high tensile strains. In the beginning of 80's *FRC* materials were developed. These materials exhibited a tension-softening quasi-brittle response, together with the increase of the toughness.

Aveston in 1971 [1], and later Krenchel and Stang in 1989 [1], demonstrated that the ductility behaviour of concrete could be increased by hundreds of times with the presence of continuous aligned fibres in the cement matrix. These materials didn't contain coarse aggregates and therefore were classified as fiber reinforced cement pastes or mortars, showing strain hardening response under tensile loads.

In the literature it is possible to find the different types of composites developed in the last three decades, which present different features in terms of tensile and flexural mechanical properties. Is possible to classify these material in the subsequent three categories:

- Composites that show strain-hardening behaviour in tension, called High Performance Fibre Reinforced Cementitious Composites (HPFRCC);
- Composites that shows deflection-hardening behaviour, called Deflection Hardening Fibre Reinforced Cement Composites;
- Composites that show only deflection-softening response, but with increased toughness.

Examples of HPFRCC include Ductal ® [1], CERACEM, CARDIFRC ®, High Performance Multimodal Fiber Reinforced Cement Composites (HPMFRCC) [8], Ultra High Performance Fiber Reinforced Concrete (UHP-FRC) [8] and ECC [1]. All these materials present different properties such as high tensile strength or high ultimate tensile strain. Normally, composites that include high tensile strength (from 10 MPa to 35 MPa) can't reach high tensile strain. This research will focus on this second type of composites that include ECC (Engineered Cementitious Composite).

ECC has a high ductility, reaching tensile strains of about 3-5% at moderate tensile stresses of 4-6 MPa. ECC was originally developed at the University of Michigan by Prof. Li and his co-workers in 1993 [1], and the approach consisted mostly on creating a synergistic interaction between fibres, matrix and the interface. The tensile ductility could be increased by the development of closely spaced multiple micro-cracks, although the fiber content is minimal (generally more or less 2% by volume). ECC is generally used in both elastic and inelastic stages, so the fibre action becomes effective under both normal and ultimate service loads. In any case, the development of this material is still evolving. A number of structural application have already appeared in Japan, Europe and US [1]. The typical tensile behaviour of ECC is shown in figure 3.1, where it is also possible to distinguish the tensile behaviour of ECC, conventional FRC and the unreinforced cementitious matrix. The tensile behaviour of ECC will be detailed in the next sections.

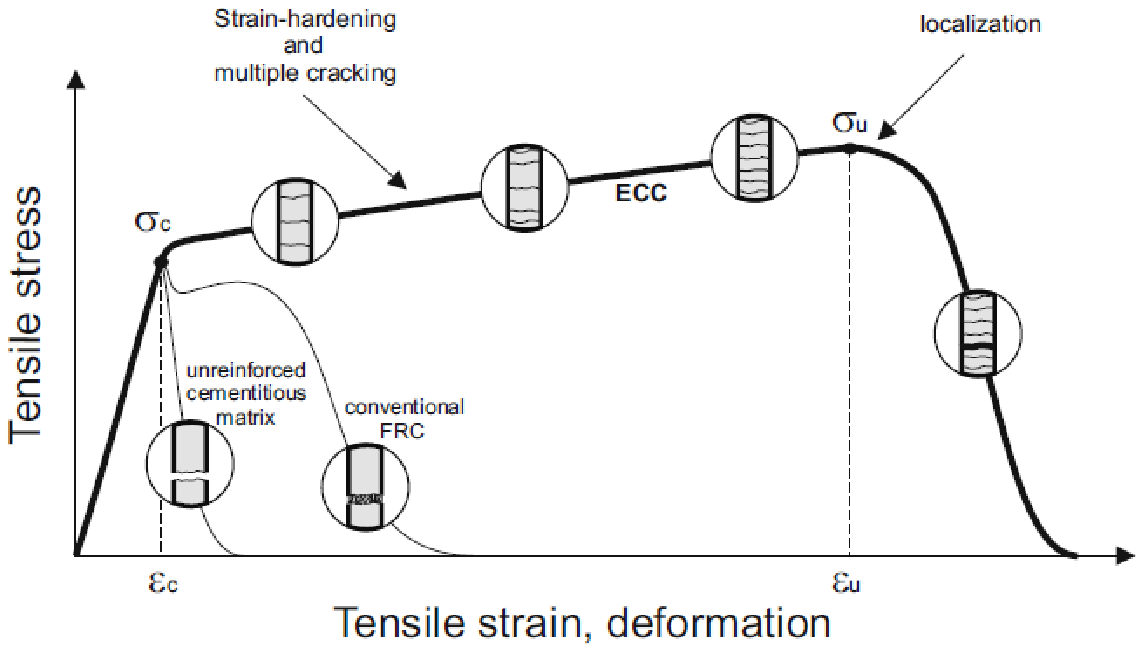

Figure 3.1: Typical tensile stress-strain diagram of ECC, FRC and unreinforced cementitious matrix [8].

3.2 Mechanical Properties

ECC materials are a class of ultra-ductile fibre reinforced cementitious composites which have a range of tensile strength, ductility and multi-cracking properties that can be adjusted depending on the demands of a particular structure. This family of materials can be design to include certain characteristics such as: self-consolidation property (ECC M45) for large-scale on-site construction developed by Kong in 2003, Lepech and Li in 2007 [1], high early strength (HES-ECC) for applications that require rapid strength gain designed by Wang and Li in 2003 [1], light weight (LW-ECC) for applications that must minimize the dead load of structural members developed by Wang and Li in 2003 [1]. Other types ECC materials have been develop by Li in 2004 and Lepech in 2007 [1] to maximize material greenness and infrastructure sustainability (Green ECC). Yang in 2005 and Li in 2007 [1] were also developing Self-Healing ECC that has the functionality of recovering the original transport and mechanical properties after experiencing damage. A summary of the major physical and mechanical properties of ECC are given in table 3.1.

Compressive Strength (MPa)	**First Crack Strength (MPa)**	**Ultimate Tensile Strength (MPa)**	**Ultimate Tensile Strain (%)**	**Young's Modulus (GPa)**	**Flexural Strength (MPa)**	**Density (g/cc)**
20 – 95	3 – 7	4 – 12	1 – 8	18 – 34	10 – 30	0.95 – 2.3

Table 3.1: Physical and mechanic range properties for ECC [1].

3.2.1 Tensile Behaviour

As reported previously, the most important characteristic of the ECC materials is the tensile behaviour, revealed by the uniaxial tensile stress-strain response. These materials can reach very high strains in tension up to 5% or more). The formation of many closely spaced micro-cracks follows the reaching of ultimate strains exceeding 300 times the one found in normal concrete. This ductile behaviour can be compared to the metal behaviour, in fact ECC materials show an elastic stage before a characteristic Yield Point, when the first micro-crack appears on the specimen. After this point, the material shows a strain-hardening response due to the formation of multiple micro-cracks which follow a volumetric straining and the increase of the load. The final failure occurs when one of the multiple cracks localizes and forms a fracture plane, as shown in figure 3.2. It is also possible to visualize the evolution of the width of the cracks during a tensile test [1; 3].

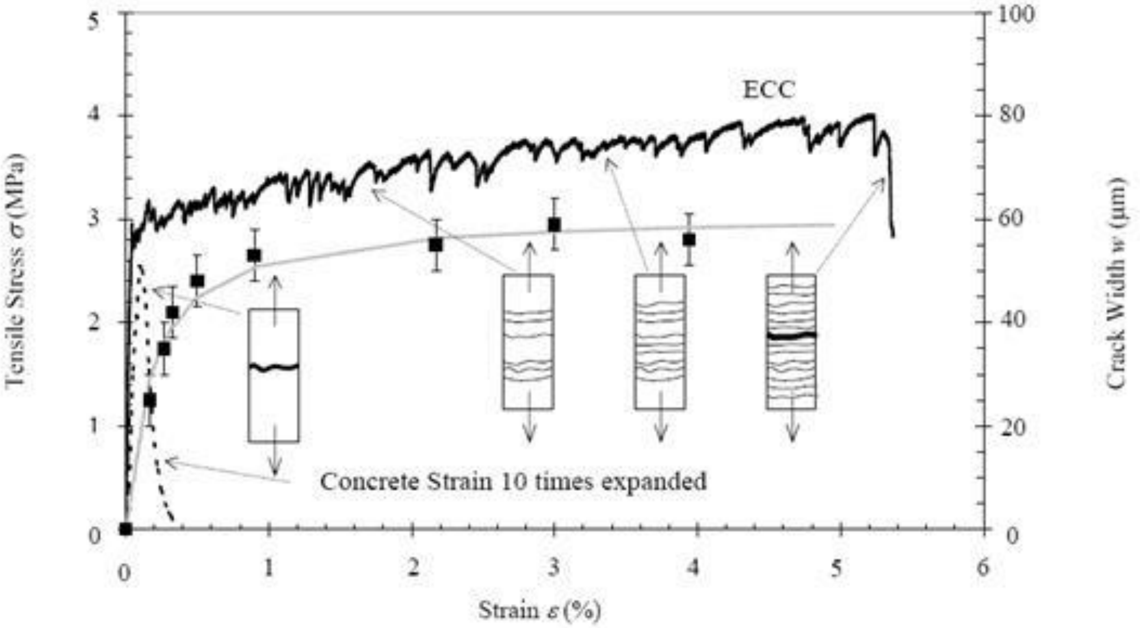

Figure 3.2: Typical ensile behaviour of ECC and concrete [1].

Before the Yield Point is reached, the ECC behaviour is not different from a normal FRC. But after this point FRC doesn't show a ductile response because of the localized crack opening. After the first cracking strain (0,01%), the micro-cracks have an opening increase from 0 to 60 µm until 1% strain. Further loading beyond this point causes the formation of other multiple cracks, with a width always roughly around 60 µm. The crack width in ECC is therefore less dependent on loading, structure size, geometry, steel reinforcement type and amount that FRC and common concrete. This unique characteristic is also important for the durability of the material and the structure [1].

3.2.2 Compressive Behaviour

ECC materials have a compressive behaviour similar to the normal and high strength concrete with a typical compressive strength ranging from 30 to 90 MPa and an elastic modulus around 20-25 GPa, typically lower than concrete due to the absence of coarse aggregates. The ultimate strain in compression can reach around 0,45-0,65%, which is higher than that of normal concrete. After the peak stress is reached, the ECC strength tends to decrease more gently than in the case of high strength concrete, and the specimen has a gradual bulging. In contrast, the conventional concrete exhibits an explosive crushing failure [1].

3.2.3 Flexural Behaviour

Due to ECC tensile hardening and multiple-cracking behaviour under imposed tensile deformations, an ECC beam, when subjected to bending, typically reaches high curvatures. During the bending test, the micro-cracks form at the lower face of the beam (figure 3.3) while large deflections are reached at increasing load (figure 3.4)[1]. In figure 3.5 the typical responses of an ECC beam tested in bending after 24 hours and 90 days are shown.

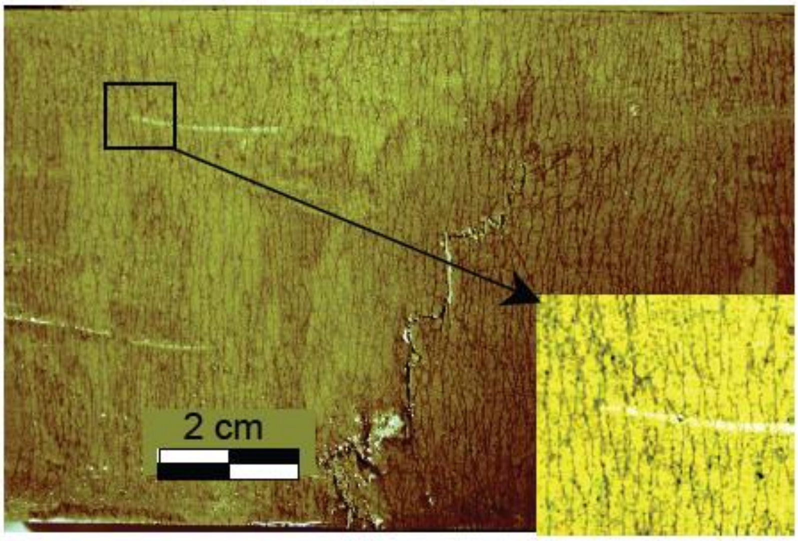

Figure 3.3: Formation of multiple-cracks in the tensile side of a beam [1].

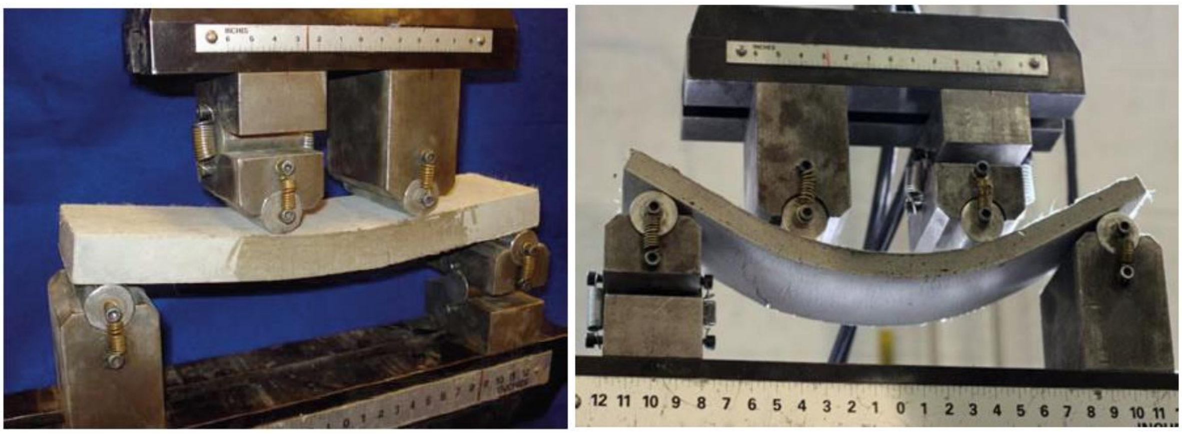

Figure 3.4: Bending test on an ECC beam [1].

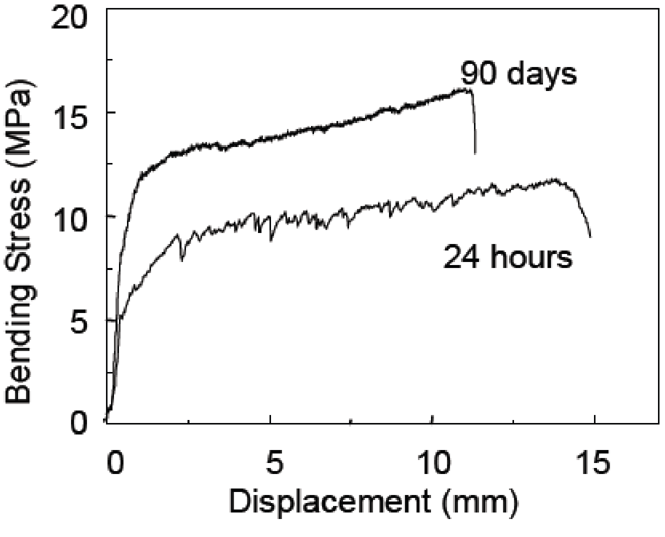

Figure 3.5: Flexural test on ECC beams after 24 and 90 days, a strength of 10-15 MPa (Modulus of Rupture) is easily attainable by this material [1].

3.3 Composition

In the past years ECC has been optimized by micromechanical design, which is a branch of mechanics applied at the material constituents scale level, and captures the mechanical interactions between fibres, mortar matrix and fibre/matrix interface.

Most of the HPFRCC require high fibre volumes to achieve high performances. However ECC uses a relatively low amount of fibres. Typically it contains fibers up to 2% of the volume, which is greater than the calculated critical fibre content needed to obtain the strain-hardening response in ECC. The matrix contains sand particles, cement grains and mineral additions that have size ranges from nano-scale to mm-scale [1; 3].

A typical mix proportion for ECC that use polyvinyl-alcohol (PVA) fiber is (weight proportion):

- Cement: 1,00
- Water: 0,58
- Sand: 0,80
- Fly ash: 1,20
- HRWR (high range water reducer): 0,013
- Fiber: 2%

Normally *Ordinary Portland Cement* is used (OPC), but blast-furnace slag may also be used with some cements that are called Portland slag cements (PSC).

The fine *silica sand* has a sand to binder ratio (S/B) of 0,36 which is used for maintaining the adequate stiffness and volume stability. Furthermore, the silica sand has a maximum grain size of 250 µm and a mean size of 110 µm.

Fly ash is used with the purpose of reducing heat generation without losing strength, as well as to increase the strength beyond 180 days, and to provide additional fines.

Super-plasticizer is used to control rheological properties of fresh concrete, to help in the dispersion of the ingredients uniformly in the mix and to increase the workability. Normally the super-plasticizer increases the slump from 5 cm to 18-20 cm without additional water, and can reduce the water content up to 15-20%, increasing the density and the strength of the concrete. Super-plasticizers are also used to reduce the porosity of the concrete. As a consequence the permeability coefficient of the cement reduces considerably and this also has an effect in increasing the durability of the material.

ECC M45, which is the ECC material that has the largest experimental dataset, has a water to binder ratio (W/B) of 0,26 to attain good balance of fresh and hardened properties. It also uses PVA fibres with 12 mm length and 39 µm diameter. The fibres have a nominal tensile strength between 880 and 1600 MPa, an elasticity modulus between 25 and 40 GPa, and a density of approximately 1300 Kg/m^3. Fibres elongation at failure is about 6-10%. The PVA fibers have one remarkable characteristic that is the strong bonding with the cement matrix [1; 4].

3.4 Micromechanics

The fundamental mechanism that governs the strain-hardening behaviour of ECC derives from the load bearing and energy absorption roles of the fibre “bridging” mechanism. Figure 3.6 shows the σ-δ curve, which can be thought of as a non-linear spring. The constitutive law of these springs can describe the connection between the opposite faces of the cracks and the average forces that the fibres can undergo wile restraining the opening of the crack when the material is under tensile loading.

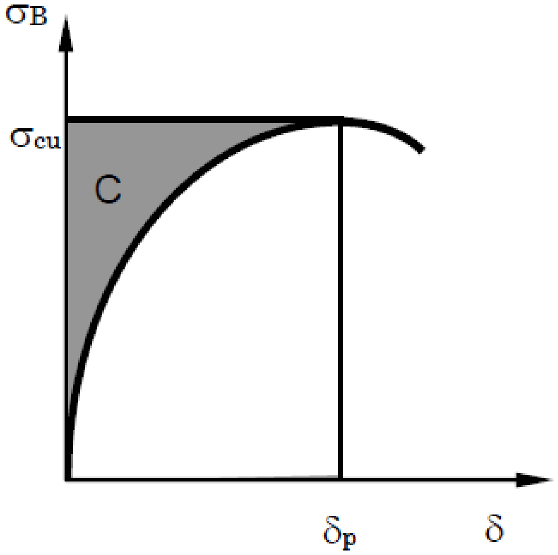

Figure 3.6: σ-δ curve [2].

There are two criteria for multiple-cracking to be attained: the strength-criterion and the energy-criterion. The first states that the matrix cracking strength must not exceed the maximum bridging stress σ_{cu}. The cracking strength is dominated by the matrix flaw size. The violation of this criterion means the formation of a crack at a load level that the fibers cannot support. The second criterion is associated with the mode of crack propagation, which is governed by the energetics of crack extension. When the fibre/matrix interface is too weak, the fibres pull-out from it and the σ-δ curve shows a low peak strength, σ_{cu}. When the interface is too strong, the springs cannot stretch and the rupture occur with a small value of critical opening displacement (δ_p). In both cases the complementary energy will be small (grey area) and a typical *Griffith crack* occurs, as shown in figure 3.7. As the crack propagates, the unloading of the springs will initiate at the middle of the crack (where the opening is maximum) and an expanding tension-softening region will follow the crack tip as the cracks continues to propagate. This implies a tension-softening failure of the composite similar to the one exhibited by conventional FRC. In contrast, a large complementary energy means that a crack remains flat so that the *steady crack* opening (figure 3.7) remains below the critical opening, resulting that the load can be transferred from the crack to the cement matrix and other cracks will be formed while the material maintains its tensile loading capacity. The behaviour of the material can be designed by controlling the σ-δ curve shape that is governed by the fibre volume fraction, length, diameter, strength and elasticity modulus, in addition to the fibre/matrix interaction parameters [2].

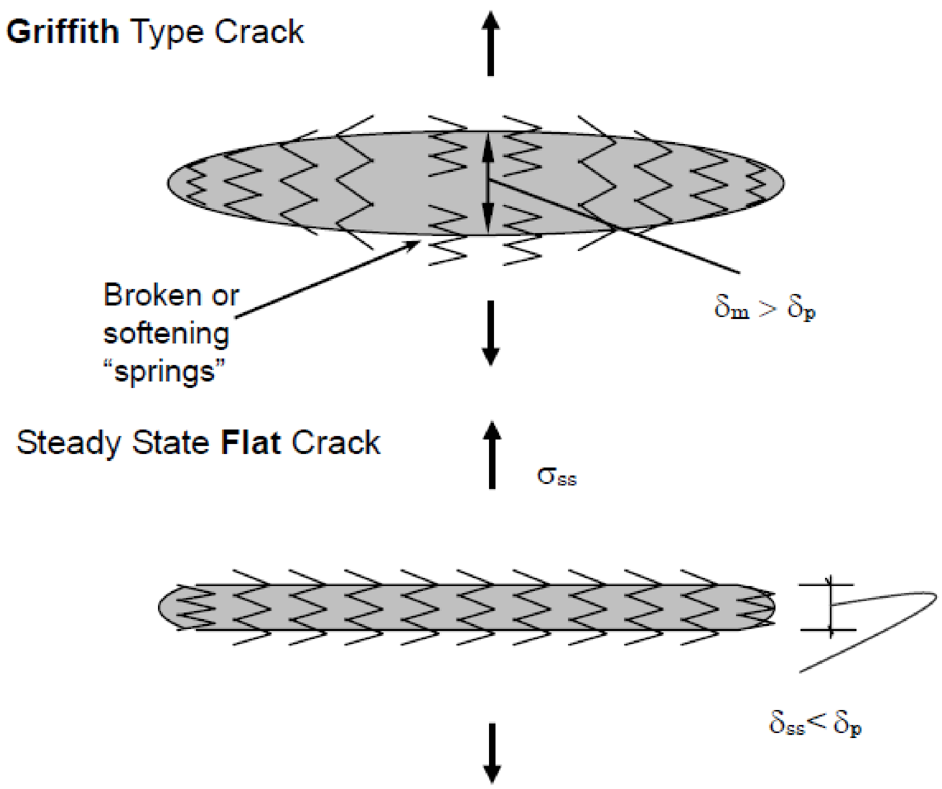

Figure 3.7: Griffith and steady state flat crack. Low complementary energy implies the first type of crack opening mode, high complementary energy implies the second type of crack opening mode [2].

3.5 Behaviour of ECC Structural Elements

Experiments have been conducted in the recent years to characterise the seismic and non-seismic behaviours of the ECC structural elements, such as flexural and shear elements, beam-column connection, walls and frames.

In 2002 Fisher and Li [1] tested R/ECC *flexural elements* under cyclic loading. The behaviour of a R/ECC column was compared to the behaviour of a regular R/C column. The details of the specimen are shown in figure 3.8. The R/ECC column showed a full hysteretic loop with larger energy dissipation and a significant damage tolerance under severe loading, as shown in figures 3.9 and 3.10. No shear stirrups were used at the base of the R/ECC flexural elements.

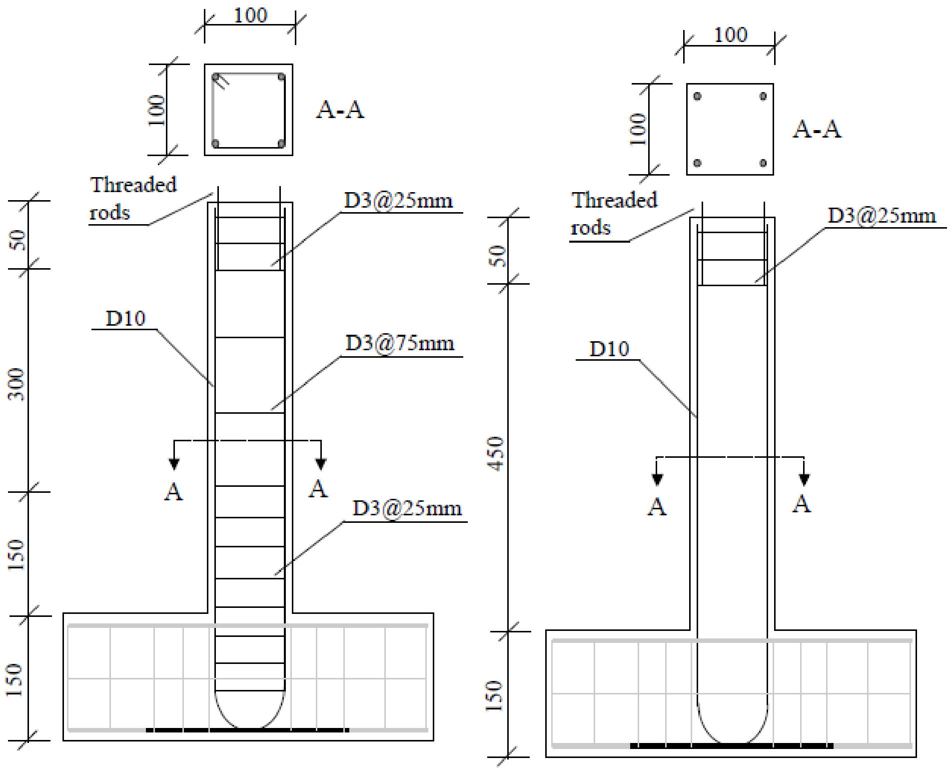

Figure 3.8: R/C and R/ECC columns [1].

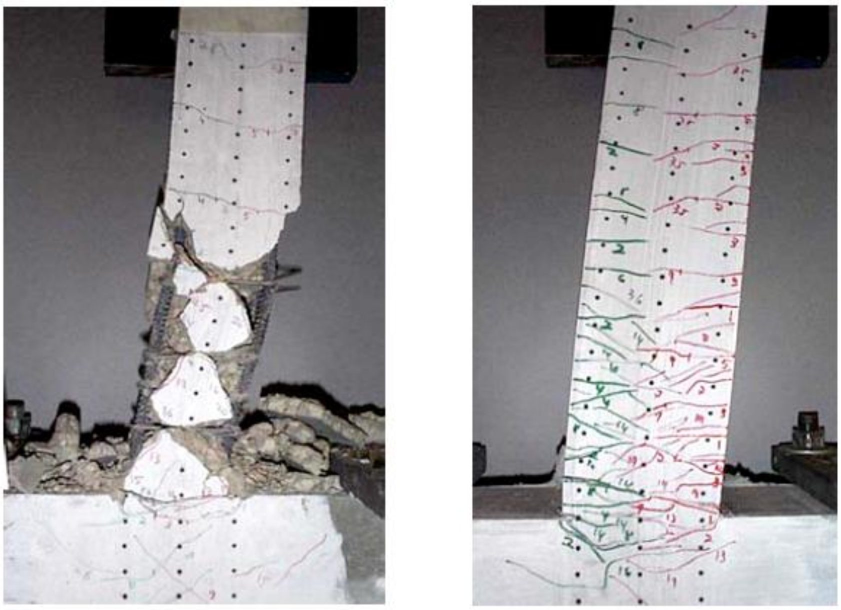

Figure 3.9: R/C and R/ECC columns after cyclic loading [1].

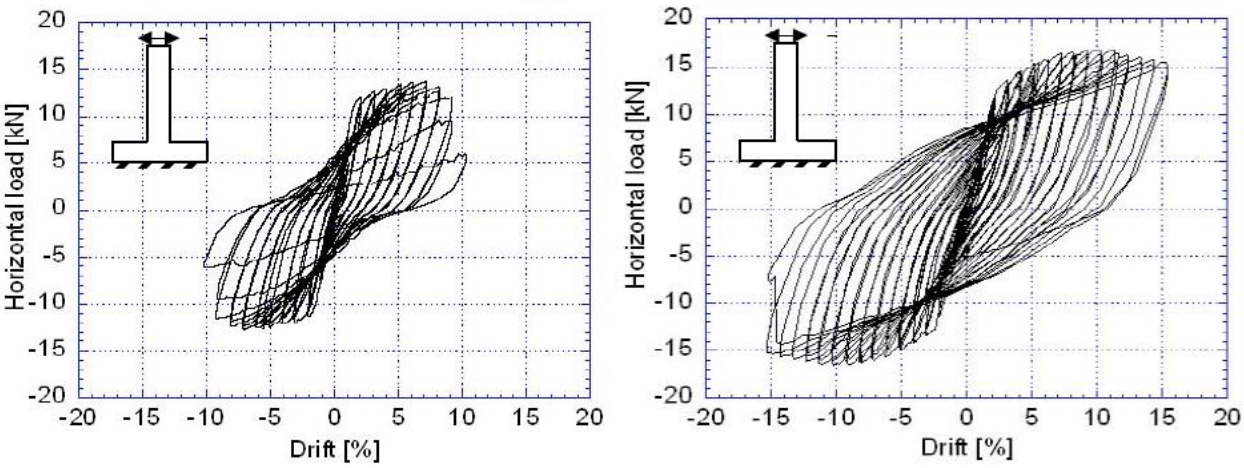

Figure 3.10: Horizontal Load-Drift diagrams of R/C and R/ECC specimen [1].

In 2004 [1] Kim studied the fatigue response of R/ECC *beams*: after over 100.000 cycles the R/ECC and also the R/C beams did not present significant stiffness degradation, but the cracks in R/C beam grew continuously up to 0,6 mm (at the end of the test), while the micro-cracks in the R/ECC beam remained approximately stationary at a crack opening of about 50 µm. Figure 3.11 shows the fatigue response of R/ECC (LS-2 and LS-3) and on R/C (LS-1) beams. The evolution of both stiffness and crack width are presented.

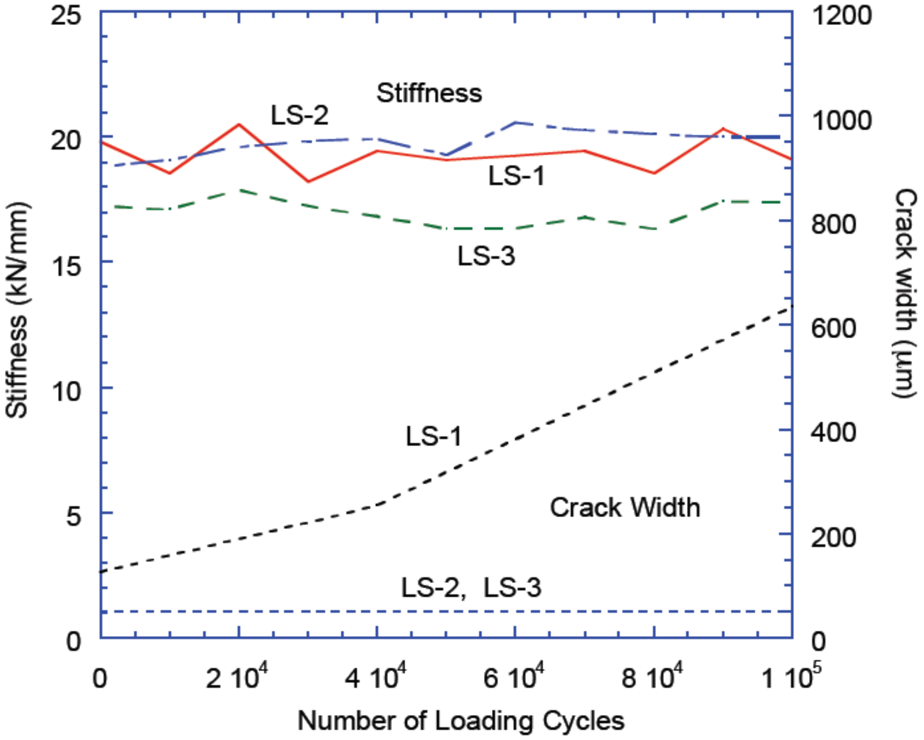

Figure 3.11: Flexural fatigue response of R/C (LS-1) and R/ECC (LS-2 and LS-3) specimens [1].

The behaviour of R/ECC *shear elements* was studied by Fukuyama in 2000 [1]. R/C and R/ECC specimens were tested under cyclic loading and the details and dimensions of the specimens are shown in figure 3.12. As shown in figure 3.13, the R/ECC element response revealed more stable hysteretic loops and greater energy dissipation. As shown in figures 3.14 and 3.15, the damage on R/ECC elements was less evident than in normal R/C with no visible bond splitting, cover loss or the formation of diagonal macro-cracks.

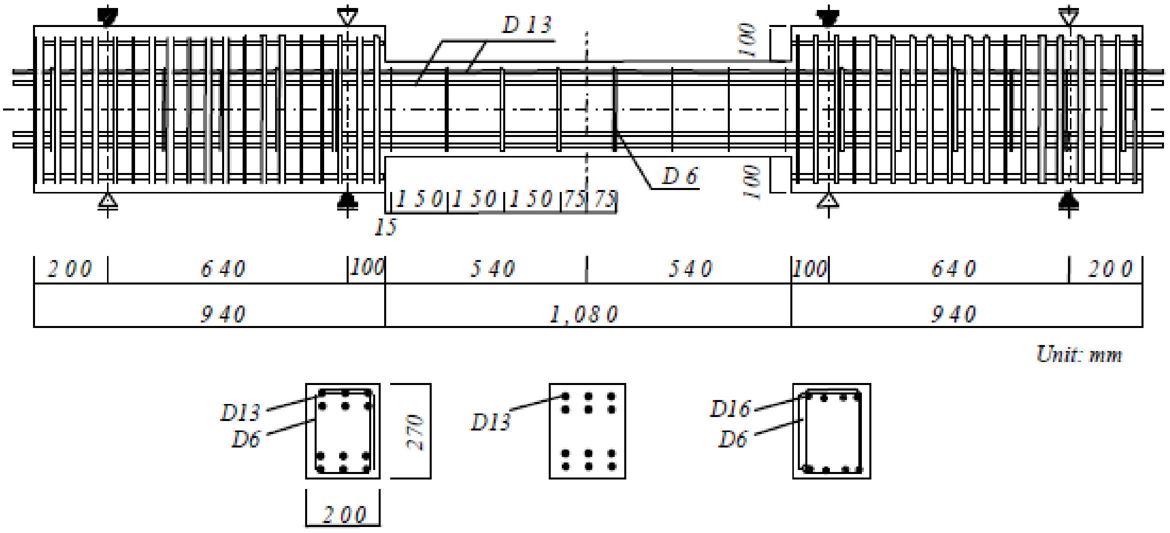

Figure 3.12: Shear element specimen [1].

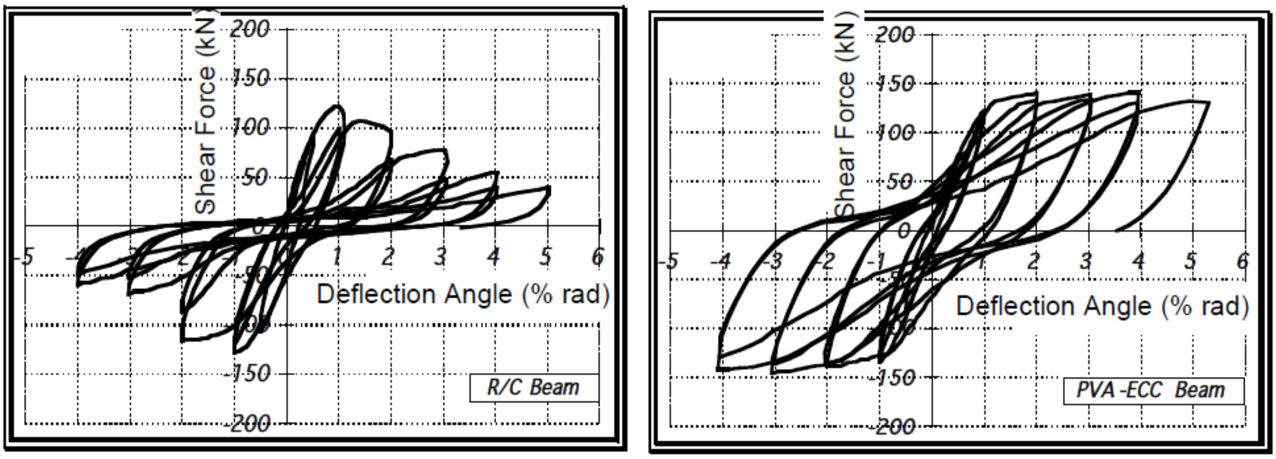

Figure 3.13: Shear Force-Deflection Angle diagrams in R/C and R/ECC specimen [1].

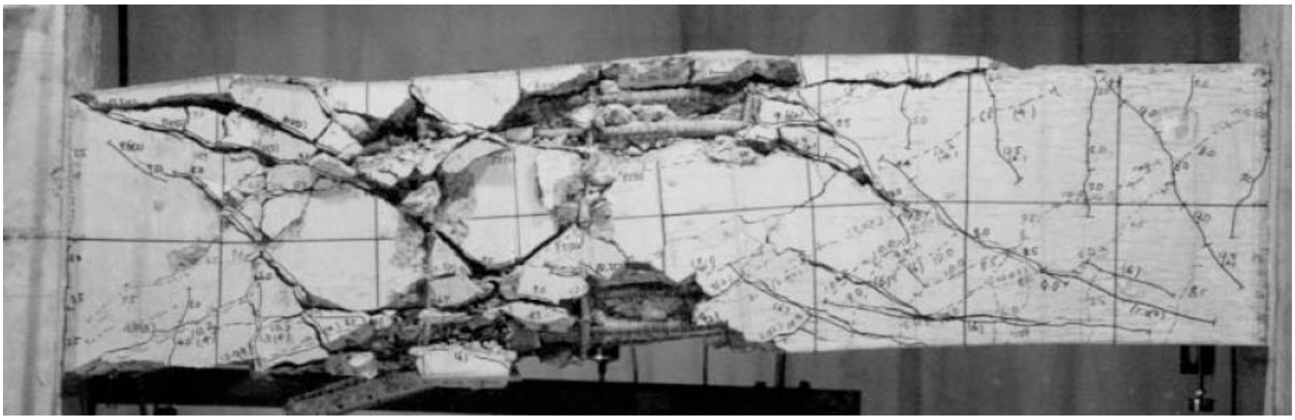

Figure 3.14: R/C shear element after cycle loading [1].

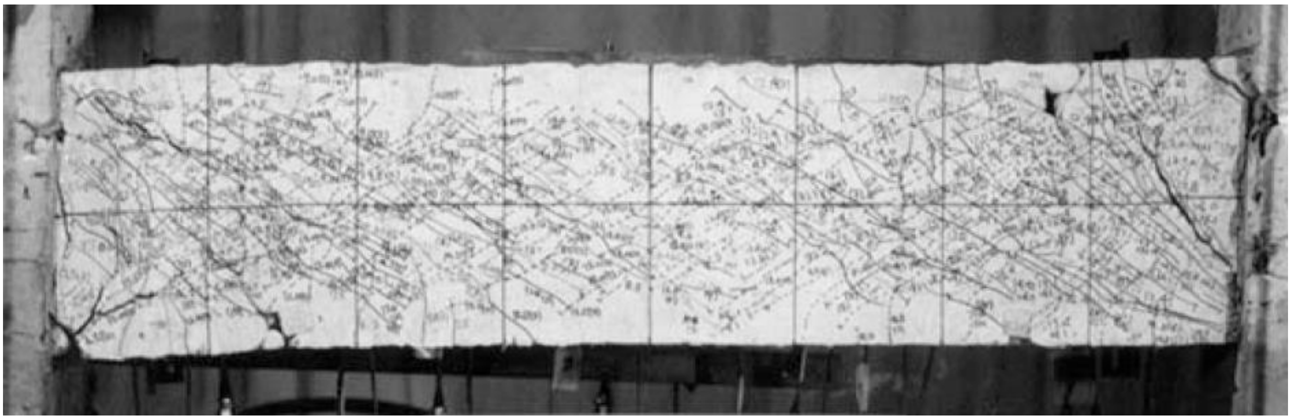

Figure 3.15: R/ECC shear element after cycle loading [1].

Fukuyama tested also R/ECC *column elements* under anti-symmetrical moment condition with an axial compressive load corresponding to 20% of the strength of the cement section of the column. Fukuyama observed that the hysteretic behaviour in terms of stability and energy dissipation in R/ECC columns was similar to the one observed in flexural and shear elements, as shown in figure 3.16. Furthermore, the R/ECC columns did not fail by shear or bond splitting [1].

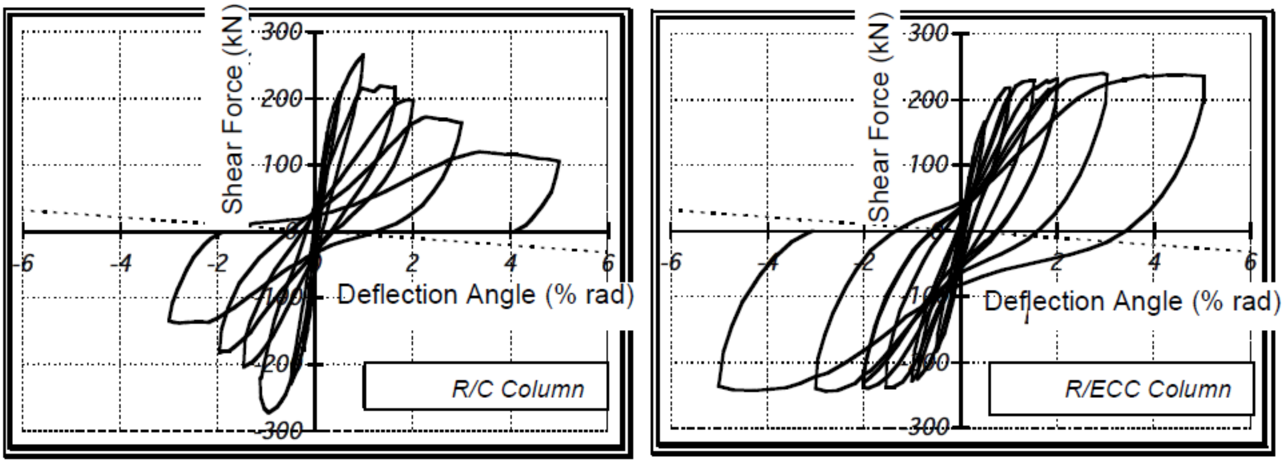

Figure 3.16: Shear Force-Deflection Angle diagrams of R/C and R/ECC columns [1].

3.6 Durability of ECC

ECC materials can be used in structures that need to undergo large deformations and must remain in service under extraordinary load events. Therefore, in addition to its superior tensile strength and ductility, ECC must show high durability under extreme environment conditions, such as long term tensile loading, freezing and thawing cycles, exposition to chloride and to alkali-silicate reactions.

The most important mechanical characteristic of the ECC is its tensile ductility. In 2004 Li an Lepech [1] investigated the *long-term tensile capacity* of ECC. Due to the continuous hydration of the cementitious materials and the delicate balance between cement matrix, fibre and cement/fibre interfaces, the strain capacity evolves with the maturing time. In figure 3.17 the strain capacity versus the age diagram is plotted. As shown, under tensile loads ECC has a long-term behaviour analogous to the compressive strength development curve in normal concrete: 10 days after casting ECC shows the peak strain capacity (5%). As hydration continues the matrix toughness increases, resulting in a lower ductility of the material. After 180 days the long-term capacity is expected to remain constant, at approximately 3% of ultimate tensile strain.

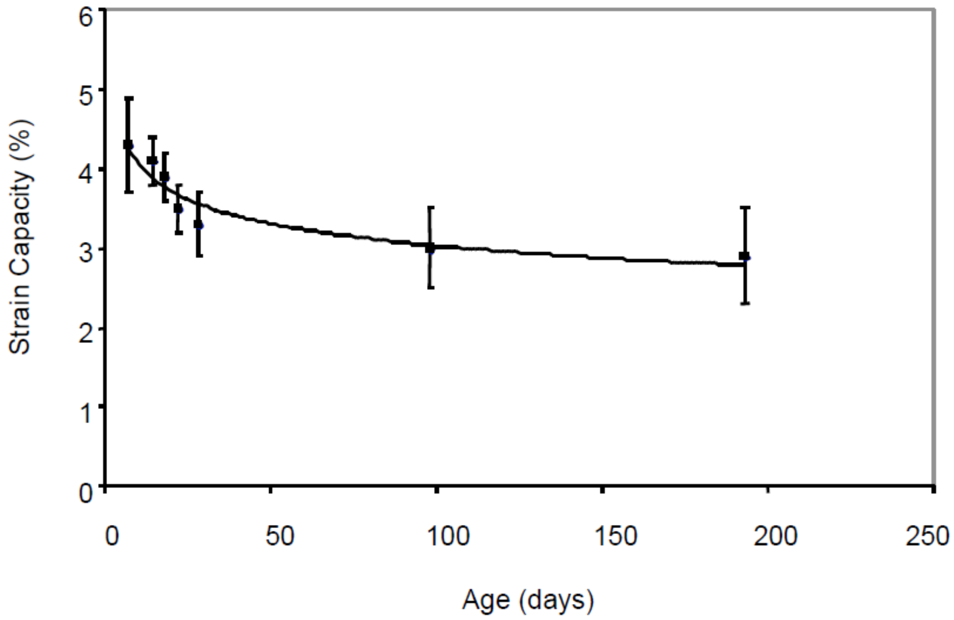

Figure 3.17: ECC tensile strain capacity as a function of the age after casting [1].

The durability under *cycles of freezing and thawing* of non-air-entrained ECC specimens was also tested by Li in 2003 [1]. As shown in figure 3.18, the concrete specimens exhibited high deterioration after 110 cycles (5 weeks) while ECC specimens underwent the test duration of 300 cycles with no degradation of the dynamic modulus on uniaxial tensile tests. Uniaxial tension tests were also performed on ECC specimens after wet curing and freeze thawing exposition, and the specimens exhibited a tensile strain capacity of approximately 3%.

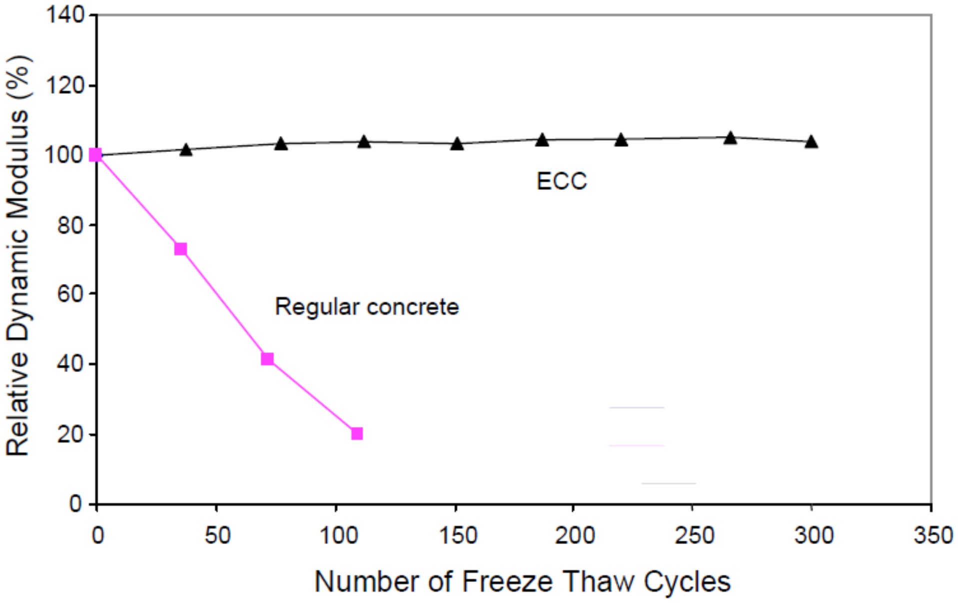

Figure 3.18: Relative dynamic modulus versus number of freeze thaw cycles of normal concrete and ECC [1]

To investigate the ECC's resistance to alkali-silicate reaction, Sharaman and Li in 2007 [1] tested ECC bar specimens immersed in alkali solution at 80°C. The specimens contained Class F and C fly ashes, high volumes of fly ash and fine silica sand. At the end of a 30 days period the specimens did not show any significant expansion. The PVA microfibers tend to restrain the expansion. The presence of high volumes of fly ash also decreases the pH value of the material, making alkali silicate reactions even less likely. The crystal nature of this particular sand also contributed to suppress the reactivity in an alkaline environment, showing that this material is not significantly vulnerable to degradation due to alkali silicate reaction.

ECC coupon specimens were tested in 2007 by Li [1] to analyse the material behaviour when exposed to environments with high *chloride concentrations*, such as marine structures or bridge decks subjected to de-icing salt applications. These specimens were preloaded at different uniaxial tension levels and exposed to a 3% NaCl solution at room temperature for 1,2 and 3 months, and subsequently reloaded up to failure. In all cases the reloaded specimens preserved the multiple crack-behaviour and tensile strain capacity of more than 3%, but the average crack width increased from 40 µm to 100 µm and the tensile strength reduced by about 10%. In figures 3.19, 3.20 and 3.21 the stress-strain diagrams obtained are shown.

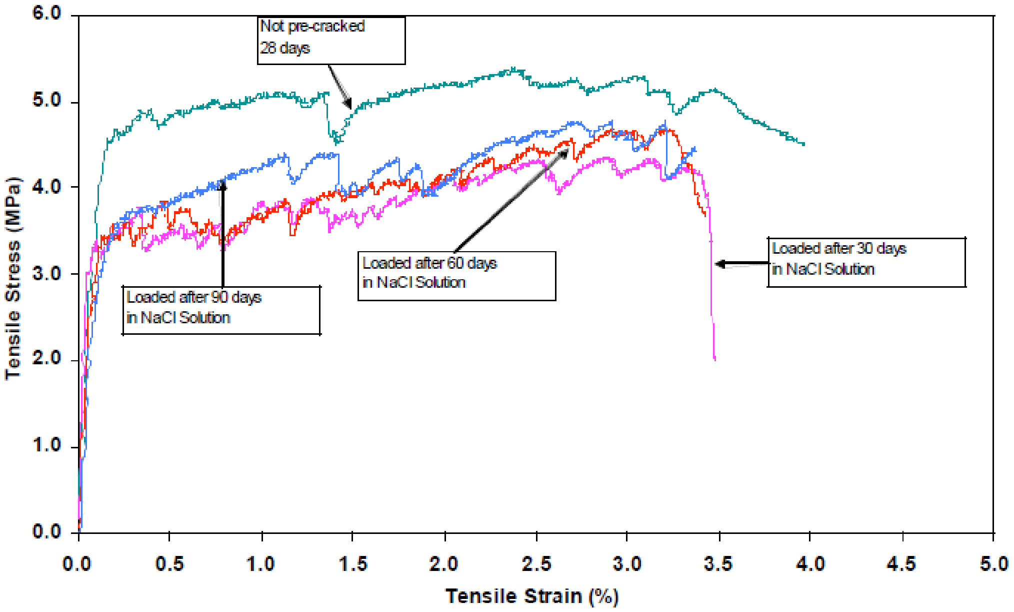

Figure 3.19: Tensile stress-strain curves of ECC: intact coupon specimens before and after subjected to 3% Na-Cl solution exposure [1].

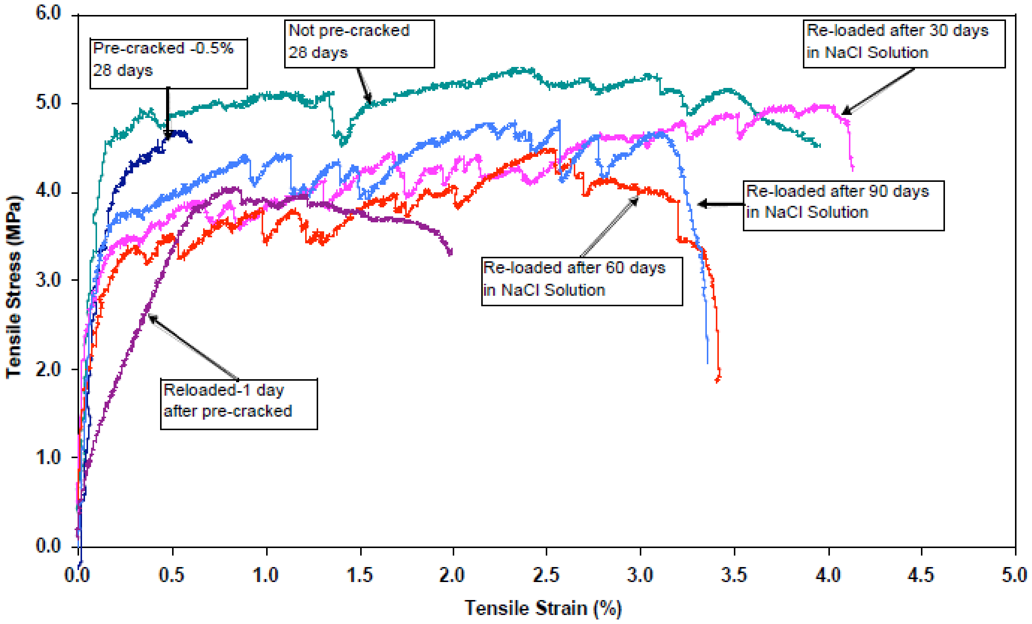

Figure 3.20: Tensile stress-strain curves of ECC pre-cracked specimens (0,5% strain) before and after subjected to 3% Na-Cl solution exposure [1].

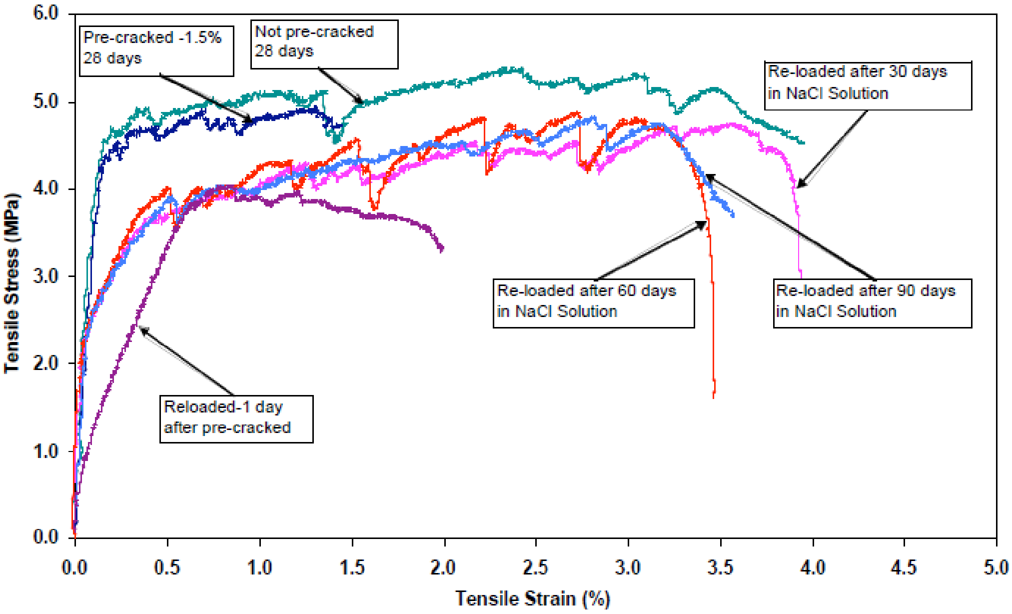

Figure 3.21: Tensile stress-strain curves of ECC pre-cracked specimen (1,5% strain) before and after subjected to 3% Na-Cl solution exposure [1].

The behaviour of non-air-entrained ECC subjected to mechanical loading and freezing and thawing cycles in the presence of de-icing salt was studied by Sahmaran and Li in 2007 [1]. After the exposure to 50 cycles, pre-loaded and intact specimens showed acceptable limits of both the surface condition by visual rating and the total mass of the scaling residue. To determine their residual tensile behaviour the specimens were reloaded for 25 and 50 cycles of freeze and thawing in the presence of de-icing salt: the specimens showed a loss of ductility but still exhibited multiple micro-cracking behaviour and 3% tensile strain capacity. These tests confirm that the ECC remains durable despite exposure to freezing and thawing cycles in the presence of de-icing salts.

Durability of R/ECC structural elements:

In normal reinforced concrete it is possible to increase the durability by means of a well-graded particle size distribution, by increasing fly ash and silica fume contents, or by reducing the water/cement ratio; all these solutions allow the formation of a dense concrete matrix that, with a more compact microstructure, exhibits lower permeability and reduced transport of corrosive elements. Obviously the increase of the durability is possible if the structure remains un-cracked during its service life, in order to restrain the transport of water, chloride ions and oxygen, which accelerate the deterioration process. The use of ECC to replace the normal concrete in steel reinforced concrete may present the following advantages:

- Alteration of the transport properties which are typical of conventional concrete: the micro-cracking behaviour of ECC delays the reaching of the aggressive agents to steel reinforcement. The transport properties of ECC include: a water permeability of about 5 x 10^{-11} m/s when permeation under hydraulic gradient is considered and the material is cracked in tension, chloride diffusion coefficient of 6,75 x 10^{-12} m^2/s which compares with the normal concrete chloride diffusion coefficient of about 10,58 x 10^{-12} m^2/s), and a sorptivity index value that is not particularly high if compared with normal concrete.
- Alteration of the nature of steel corrosion: the dispersed micro-cracks in a large region of the steel, instead of a concentrated crack, leads to a slower rate of corrosion and avoids spalling.

An experimental investigation carried out by Sahmaran in 2006 [1] showed that after 50 and 150 hours of accelerated corrosion exposure, the flexural strength of ECC specimens retained almost 100% of the original flexural capacity, and after 300 hours retained over 45% (figure 3.22). It also showed that after 25, 50 and 75 hours, steel reinforced bars in mortar specimens lost 2.5%, 5.3% and 11.7% percentage of mass, while steel reinforced bars in ECC specimens did not lose any appreciable mass before 50 hours, although loosing 17.5% percentage of mass after 300 hours of accelerated corrosion testing (figure 3.23 and 3.24).

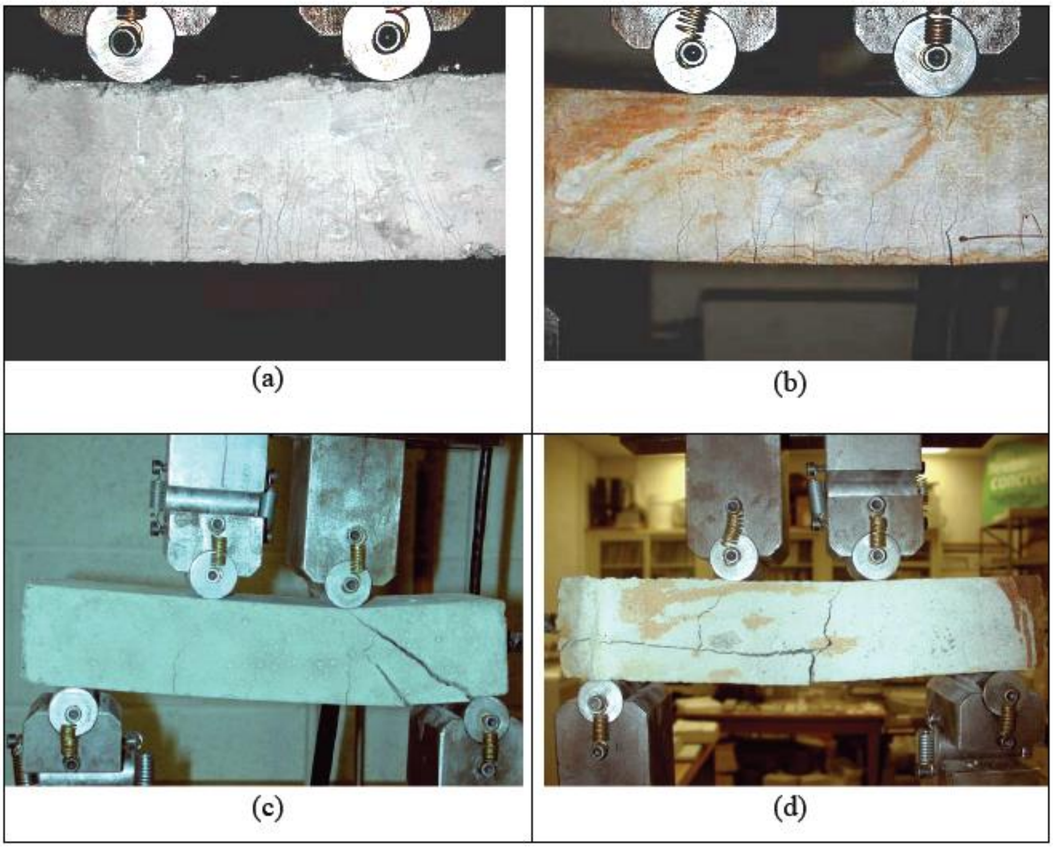

Figure 3.22: Reinforced mortar and ECC beam specimens under four point bending tests: ECC beams before (a) and after (b) 150 hours accelerated corrosion; reinforced mortar before (c) and after (d) 50 hours accelerated corrosion [1].

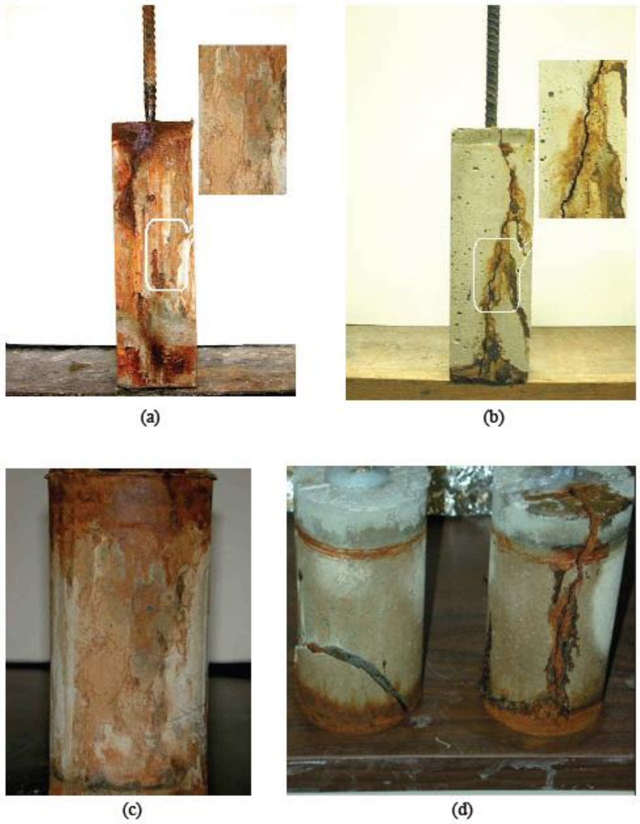

Figure 3.23: prismatic ECC specimen after 300 hours of accelerated corrosion test (a), prismatic mortar specimen after 75 hours of accelerated corrosion test (b), cylindrical ECC specimen after 350 hours of accelerated corrosion test (c) and cylindrical mortar specimen after 95 hours of accelerated corrosion test [1].

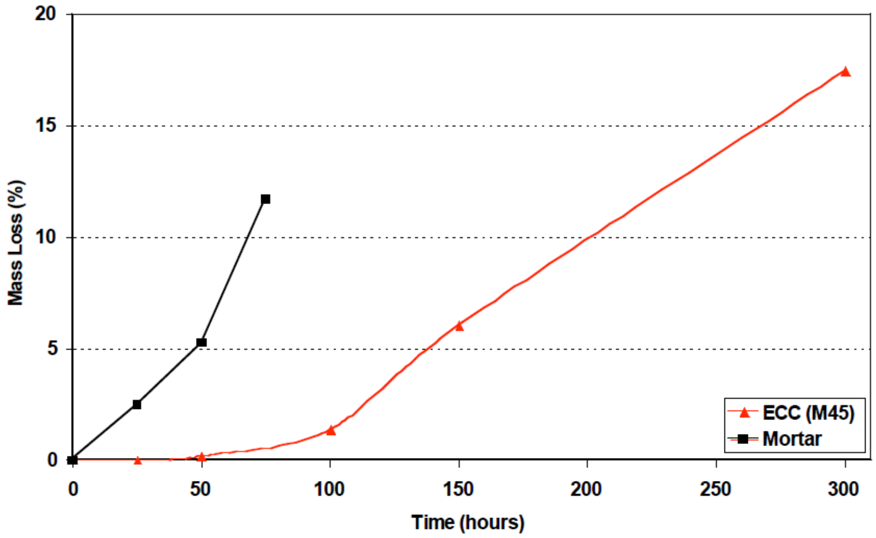

Figure 3.24: Percentage of reinforced steel mass loss after accelerated corrosion tests in ECC and mortar specimens [1].

3.7 Self-healing

The formation of cracks in concrete elements reduce the durability and the lifetime of a structure, exposing it to the environmental attack by aggressive agents. This causes a loss in stiffness and durability of the structure, increasing the cost of maintenance. Recent studies [5] showed that cracked cements have the ability to heal themselves over time if exposed to water. This extraordinary property cannot be exploited in normal reinforced concrete elements because of the large crack width, but may be very important in ECC structural elements. In fact this self-healing behaviour depends mostly on the crack width, and smaller cracks heal faster and more efficiently than large cracks. These studies proved that sometimes small cracks can heal completely, increasing mechanical properties and durability of the material. In addition, a gradual reduction in permeability occurs due to the diminishing of the crack width, as healing occurs.

Healing is a complex process that involves chemical and physical mechanism such as:

- Reaction of un-hydrated cement.
- Swelling of C–S–H.
- Precipitation of calcium carbonate crystals.
- Closing of cracks by impurities within the water.
- Closing of cracks by concrete particles from spalling on the crack faces.

Precipitation of calcium carbonate crystals is the main mechanism contributing to healing, but there are other mechanisms that increase the healing behaviour of the concrete such as chemical and bacterial encapsulation, or mineral admixtures and chemicals added in glass tubing.

The experimental studies by Herbert and Li showed that the self-healing of micro-cracks in ECC specimens can occur in natural environments with large variations of temperature even if the element has undergone tensile deformations from 0.5% to 1%. Furthermore, the level of stiffness and first crack strength could be completely recovered and often could exceed the initial value.

3.8 Applications and Costs

Engineered Cementitious Composites have been studied and tested in the past years showing positive properties that make it an important alternative for special engineering application. ECC materials have already been applied in real size structural applications, such as in a skyscraper in Japan or a mall in Canada and a bridge in Michigan [6]. In general these examples manifest less signs of damage than normal reinforced concrete structures. These constructions have in general a longer lifetime and are more sustainable due to a reduction of maintenance and repairing costs, a reduced environmental impact and an overall improvement of the safety of structures constructed with concrete. Unfortunately the price of ECC is still higher than normal concrete. The use of PVA fibre, even if in a small weight percentage, and the use of larger amounts of cement in the matrix increase the cost of these materials about three times relatively to normal concrete. However the initial investment can be easily recovered during the following years by the reduction of maintenance costs and the increasing of the service life of the structure [2, 6]. In the specific case of the bridge in Michigan, the ECC was used in a link slab to connect portions of the bridge deck, as shown in figure 3.25). Normally, separate portions of bridges are linked by mechanical expansion joints, which undergo stress, expansion and contraction deformations due to temperature gradient, vehicle loads and settlements, and can easily deteriorate. The use of the ECC link slab improved the behaviour of the bridge under thermal expansion and contraction. Furthermore, the self-healing behaviour of micro-cracks contributed to extend the proper functioning of the bridge.

Figure 3.25: ECC link slab in a bridge in Michigan [6].

3.9 Conclusions

In the previous pages, the most important features of Engineered Cementitious Composites have been discussed. Considering all the typical retrofit approaches and methods already explained in the previous chapter, it seems that these materials possess several characteristics that could contribute considerably to improve some of these retrofit approaches. One interesting idea is to use this materials as jacketing for damaged columns and piers. This method could be used not only to increase the strength of the element, but also to increase the displacement capacity and energy dissipation ability. One of the several features of this technique is the reduction of construction time and costs: in fact the composite is applied to the damaged part of the element with spraying technique and doesn’t need any additional reinforcement, increasing the ultimate load, the ductility of the recovered element and preventing the buckling of the longitudinal reinforcement (figure 3.26). M. Kunieda, et al. in 2012 [7] tested under cyclic loading two damaged R/C columns retrofitted with normal concrete and UHP-SHCC (Ultra-High Performance Strain Hardening Cementitious Composite) and obtained the results showed on figure 3.27. As shown, the second column, after retrofit, exhibited an increase of strength, an increase of displacement capacity and an increase of energy dissipation. On the contrary, the first column showed lower values of strength and displacement.

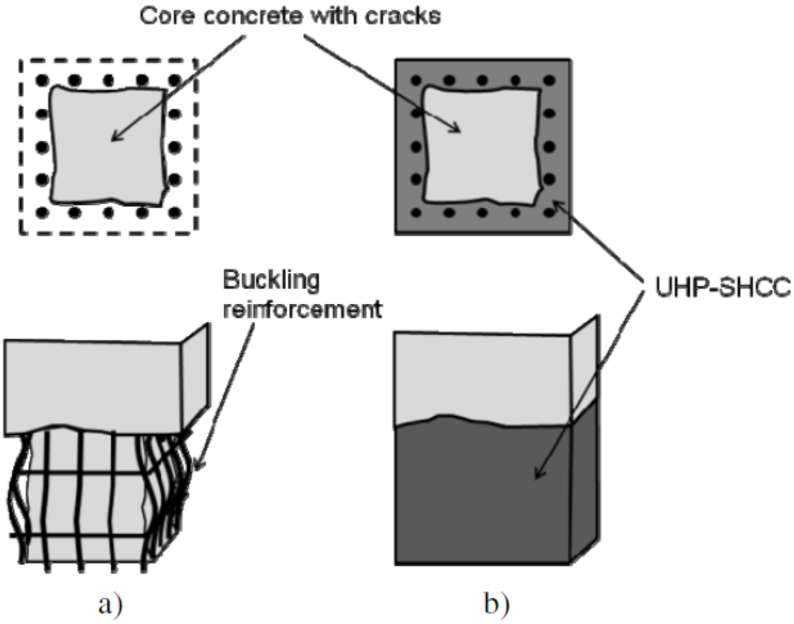

Figure 3.26: Construction procedure: a) damaged column, b) repaired column [7].

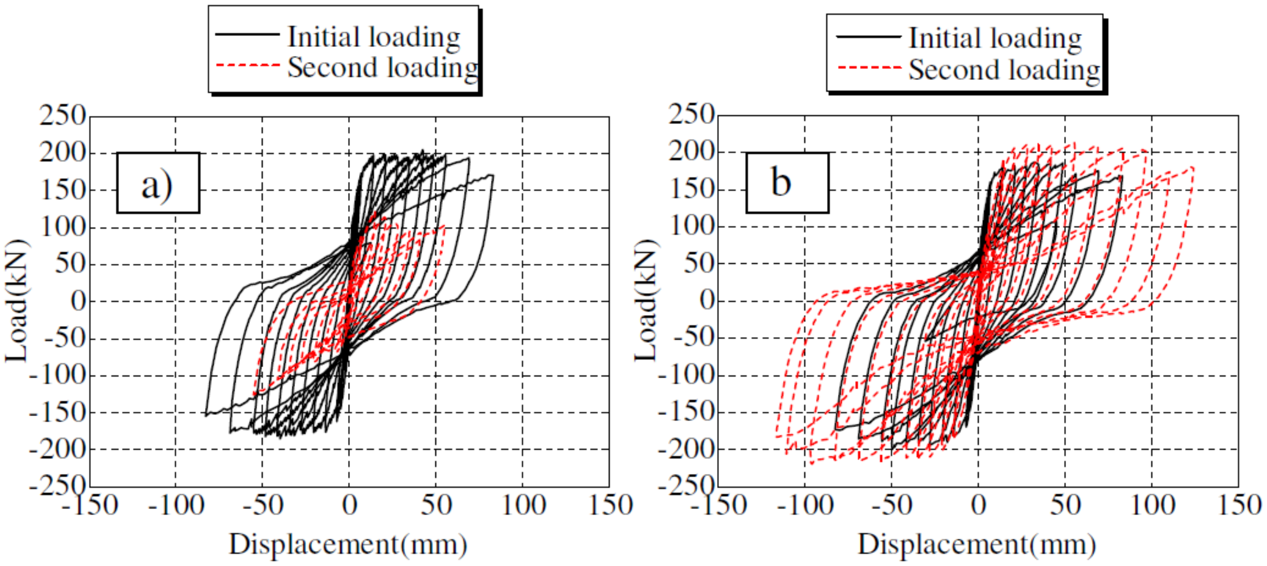

Figure 3.27: Load-Displacement diagrams of the two columns retrofitted with concrete (a) and UHP-SHCC (b) [7].

Bibliography

[1] Victor C. Li (2007); Engineered Cementitious Composites (ECC) – Material, Structural, and Durability Performance; University of Michigan, MI 48109, pages 1-78.

[2] Victor C. Li (2003); Invited Paper On Engineered Cementitious Composites (ECC), A Review of the Material and Its Applications; Journal of Advanced Concrete Technology Vol. 1, No. 3, 215-230, November 2003, pages 1-16.

[3] Mustafa Sahmaran and Victor C. Li (2003); Engineered Cementitious Composites. Can Composites Be Accepted as Crack-Free Concrete?; Journal of the Transportation Research Board, No. 2164, pages 1-8.

[4] A. W. Dhawale, V. P. Joshi (2013); Engineered Cementitious Composites for Structural Applications; International journal of Application or Innovation in Engineering of Management, ISSN 2319–4847, pages 1-8.

[5] Emily N. Herbert and Victor C. Li (2013); Self-Healing of Microcracks in Engineered Cementitious Composites (ECC) Under a Natural Environment; materials, ISSN 1996-1944, pages 1-11.

[6] J. Marks and J. Conklin (2013); Engineered Cementitious Composites: Applications and Impact of High Tensile, Self-Healing Concrete, University of Pittsburgh Swanson School of Engineering, Session A5, Paper #3204, pages 1-7.

[7] M. Kunieda, et al. (2012); Rapid Jacketing Technique by Using UHPSHCC for Damaged RC Column under Seismic Loading; Dept. of Civil Engineering, Nagoya University, Japan, pages 1-6.

[8] Eduardo Pereira (2012); Processes of Cracking in Strain Hardening Cementitious Composites, PhD thesis, University of Minho, pages 1-36.

4. Super-Elastic and Shape Memory Alloys on Seismic Retrofitting

4.1 General Overview

Shape memory alloy (SMA) are materials with extraordinary mechanical properties which are commonly used in biomedical, aerospace, automotive, robotic and telecommunication applications [4] (figure 4.1).

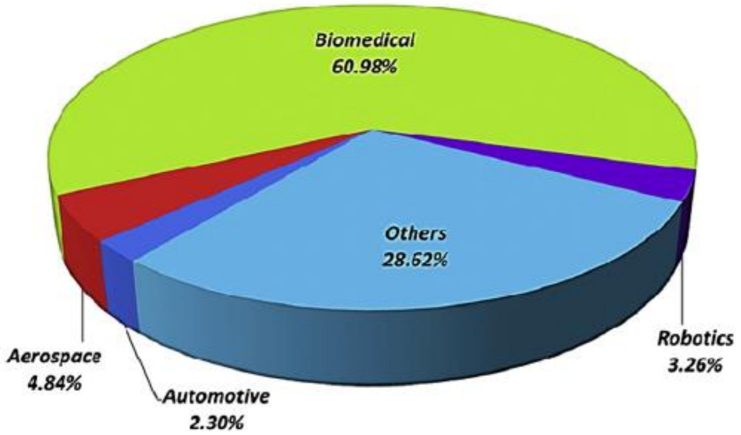

Figure 4.1: SMA US patents from January 1990 to September 2013 [4].

One of its properties was discovered for the first time in the 1930s, by Otsuka and Wayman [4]. They have observed the *pseudo-elastic behaviour* of an Au-Cd alloy in 1932. In the subsequent decades, other properties were discovered in similar materials. Greninger and Mooradian observed the formation of a *martensitic phase* with the change of the temperature in 1938. The *shape memory effect* governed by thermo-elastic behaviour was discovered by Kurdjumov and Khandros in 1949 [4], and reported by Chang and Read in 1951. In 1962 Buechler and co-researchers observed these previously mentioned properties in a Nickel-Titanium alloy at the Naval Ordinance Laboratory, and called this material NiTinol.

This material is one of the most used nowadays in engineering applications, due to its superior thermo-mechanical and thermo-elastic properties, its stability and practicability, that make it one of the most flexible and beneficial material for these applications [2].

The shape recovery behaviour of these alloys can be materialized in two different properties [9] (figure 4.2):

- Shape memory effect (SME): If the material undergoes a deformation at a low temperature, it can regain the original shape by just applying heat to the material.
- Super-Elasticity or Pseudo-Elasticity (SE): if the material is loaded at high temperature, the original shape can be recovered by just removing the applied load.

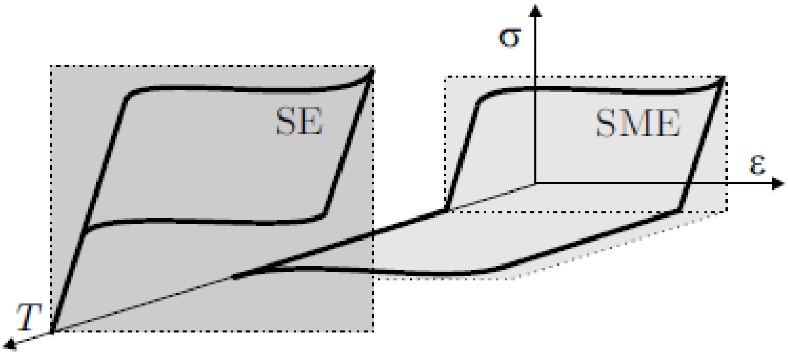

Figure 4.2: SMAs Super-Elastic and Shape Memory Effect with temperature change [9].

More than thirty different alloys have been discovered until today [3]. In tables 4.1 and 4.2, some of the alloys that exhibit shape memory effect, and their mechanical properties, are reported:

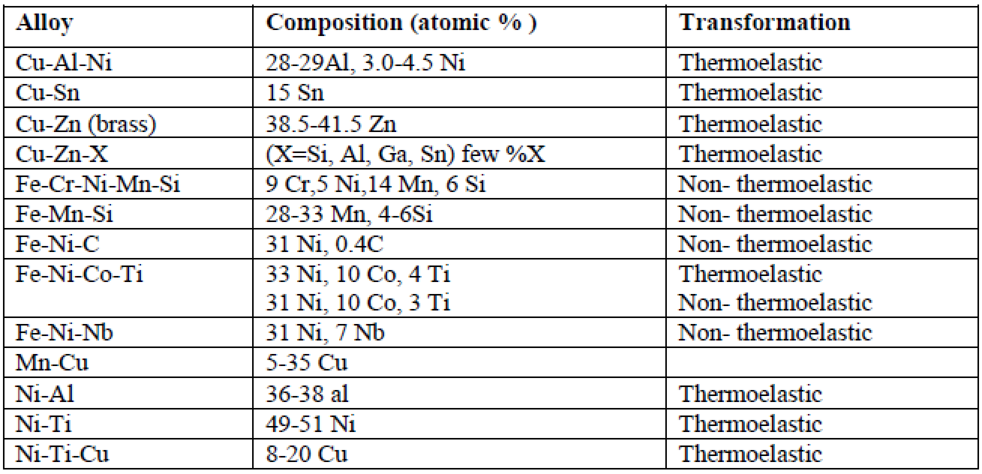

Alloy	**Composition (atomic %)**	**Transformation**
Cu-Al-Ni	28-29Al, 3.0-4.5 Ni	Thermoelastic
Cu-Sn	15 Sn	Thermoelastic
Cu-Zn (brass)	38.5-41.5 Zn	Thermoelastic
Cu-Zn-X	(X=Si, Al, Ga, Sn) few %X	Thermoelastic
Fe-Cr-Ni-Mn-Si	9 Cr,5 Ni,14 Mn, 6 Si	Non- thermoelastic
Fe-Mn-Si	28-33 Mn, 4-6Si	Non- thermoelastic
Fe-Ni-C	31 Ni, 0.4C	Non- thermoelastic
Fe-Ni-Co-Ti	33 Ni, 10 Co, 4 Ti 31 Ni, 10 Co, 3 Ti	Thermoelastic Non- thermoelastic
Fe-Ni-Nb	31 Ni, 7 Nb	Non- thermoelastic
Mn-Cu	5-35 Cu	
Ni-Al	36-38 al	Thermoelastic
Ni-Ti	49-51 Ni	Thermoelastic
Ni-Ti-Cu	8-20 Cu	Thermoelastic

Table 4.1: Different Shape Memory Alloys [3].

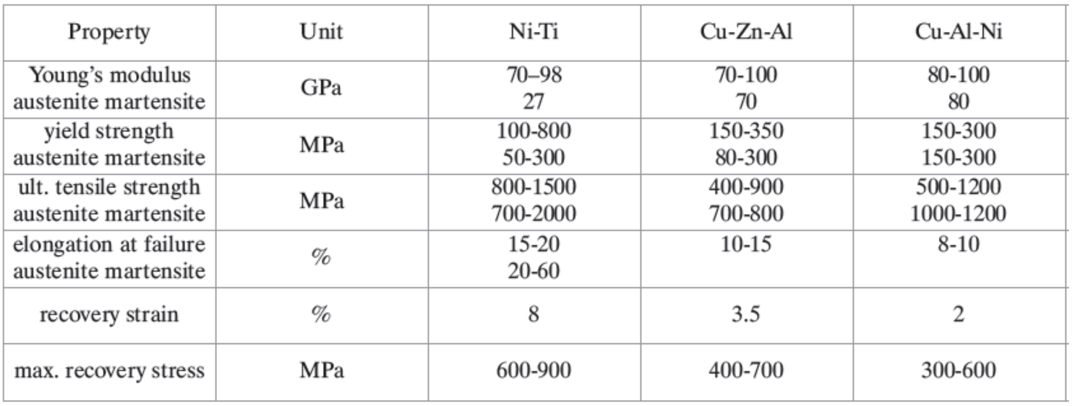

Property	Unit	Ni-Ti	Cu-Zn-Al	Cu-Al-Ni
Young's modulus austenite martensite	GPa	70–98 27	70-100 70	80-100 80
yield strength austenite martensite	MPa	100-800 50-300	150-350 80-300	150-300 150-300
ult. tensile strength austenite martensite	MPa	800-1500 700-2000	400-900 700-800	500-1200 1000-1200
elongation at failure austenite martensite	%	15-20 20-60	10-15	8-10
recovery strain	%	8	3.5	2
max. recovery stress	MPa	600-900	400-700	300-600

Table 4.2: Shape Memory Alloys Mechanical Properties [7].

The properties that make SMAs interesting for civil structures are [2;3]:

- The large force generated upon returning to its original shape.
- Repeated absorption of large amounts of strain energy under loading without permanent deformation.
- SMA has excellent damping characteristics at temperature below the transition temperature range.
- Excellent corrosion resistance (comparable to series 300 stainless steels) and nonmagnetic.
- SMA has low density and high fatigue resistance under large strain cycles.
- It has the ability to be heated electrically for the recovery of shape.

4.2 Crystal Structure

Shape Memory Alloys have two different phases, characterized by three different crystal structures, and six possible transformations [4]. Figure 4.3 describes the stress-strain-temperature diagram of a typical Shape Memory Alloy, including all the possible transformations and phases, which are explained subsequently.

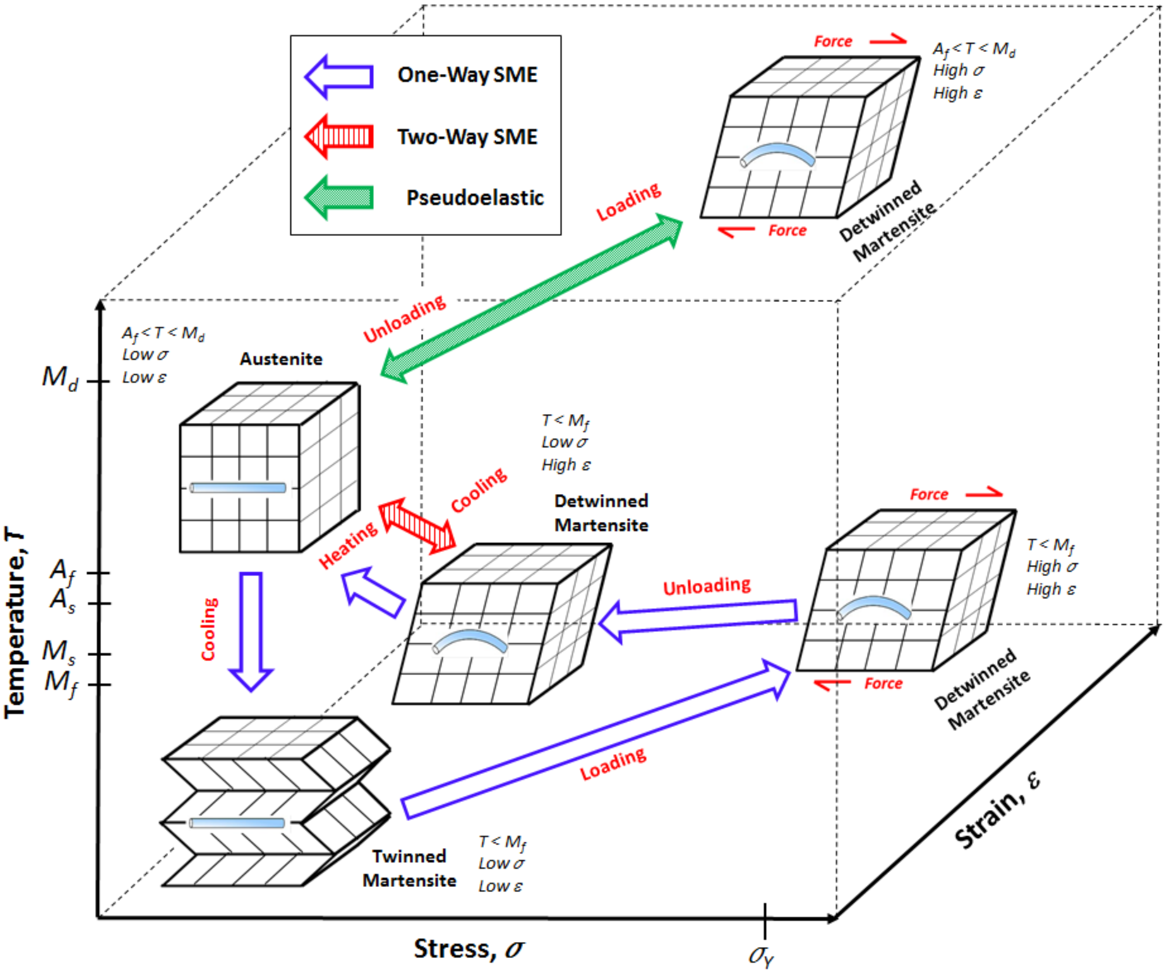

Figure 4.3: General SMA Martensite and Austenite phase transformation after stress and temperature variations [4].

One phase is called *Martensite* [2; 9], which is normally a less-ordered (parallelogram asymmetric) crystal structure and is stable at low temperatures and high stresses. The other phase is called *Austenite*, which has a body-centred cubic ordered structure and is stable at high temperatures and low stresses. The Martensitic phase can exist in two different crystal structures: *Twinned* (or self-accommodated) and *Detwinned* Martensite. Normally Martensitic phase is weaker than Austenitic phase and can be easily deformed, because in Austenitic phase the high temperature causes the atoms to arrange themselves into the most compact possible pattern, resulting in a rigid cube arrangement that has higher resistance to external stresses. SMA crystal structures are shown in figure 4.4.

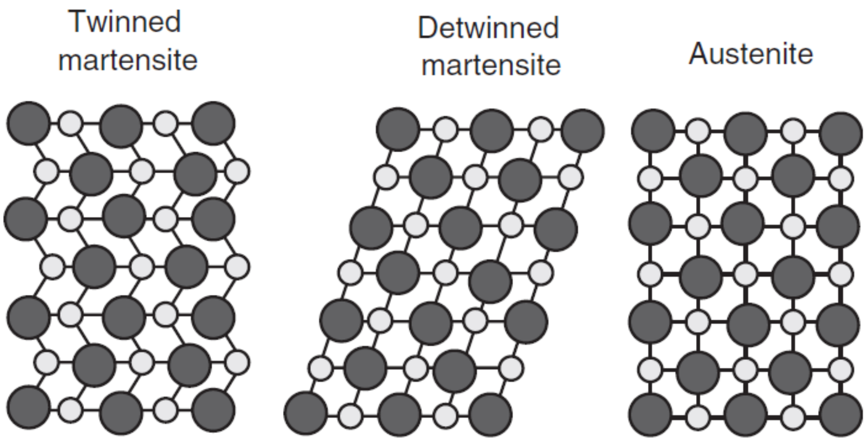

Figure 4.4: Shape Memory Alloys phases and crystal structures [2].

The martensitic transformation, that is a shear lattice distortion with no diffusive process involved [2, 9], can be temperature induced (Shape Memory Effect) or stress induced (Super-Elasticity).
Figure 4.5 shows the Martensitic and Austenitic fraction as a function of temperature, without any applied load.

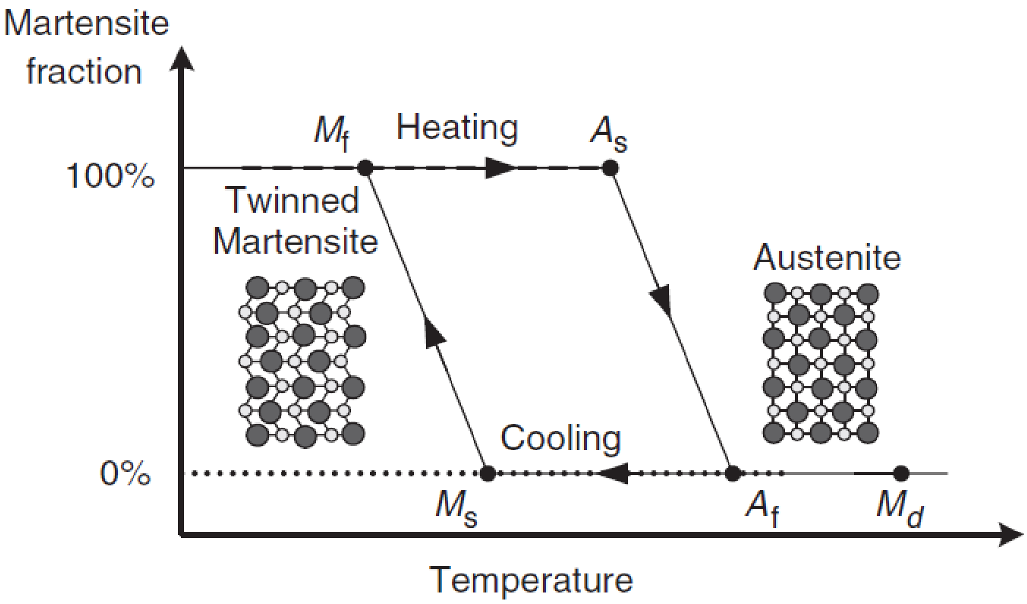

Figure 4.5: Martensite and Austenite temperature fraction [2].

There are four characteristic temperatures at which phase transformations occur [2; 4]:

- As (Austenite start temperature): where the material starts to transform from twinned Martensite to Austenite.
- Af (Austenite finish temperature): where the material is completely transformed into Austenite.
- Ms (Martensite start temperature): where the material starts to transform from Austenite to twinned Martensite.
- Mf (Martensite finish temperature): where the Martensite transformation is completed.
- Md (Martensite desist): the maximum temperature at which SMAs phase transformation can no longer be stress induced, after this temperature the material will be permanently deformed.

Table 4.3 shows a typical range of Nitinol characteristic temperatures.

M_f °C	M_s °C	A_s °C	A_f °C
-10	17	30	45

Table 4.3: Nitinol’s typical characteristic temperatures [9].

4.3 Shape Memory Effect

The SMAs have different shape-memory effects, the most common effects are called One-Way and Two-Way Shape Memory (figure n. 4.6).

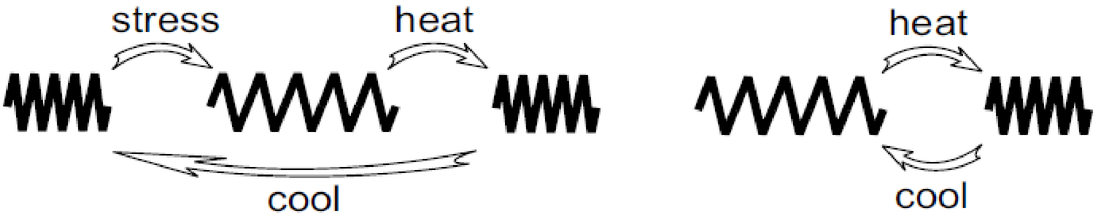

(a) One-way shape memory effect (b) Two-way shape memory effect

Figure 4.6: Different Shape Memory Effect [9].

- The One-Way Shape Memory (a): if the alloy is at a temperature lower than the As point and Twinned Martensite phase is present, the metal can be stretched or bended by applying a load and change to Detwinned Martensite phase. After removing the load the metal can return to the original shape just by applying heat, which is responsible for bringing the alloy to a temperature higher than Af (Austenite phase). When the material cools down and returns to a temperature lower than Ms, it adopts the Twinned Martensite phase and returns to its original shape. Figures 4.7 and 4.8 show the relations between stress, strain, temperature and load in One Way Shape Memory effect [4, 6, 9].

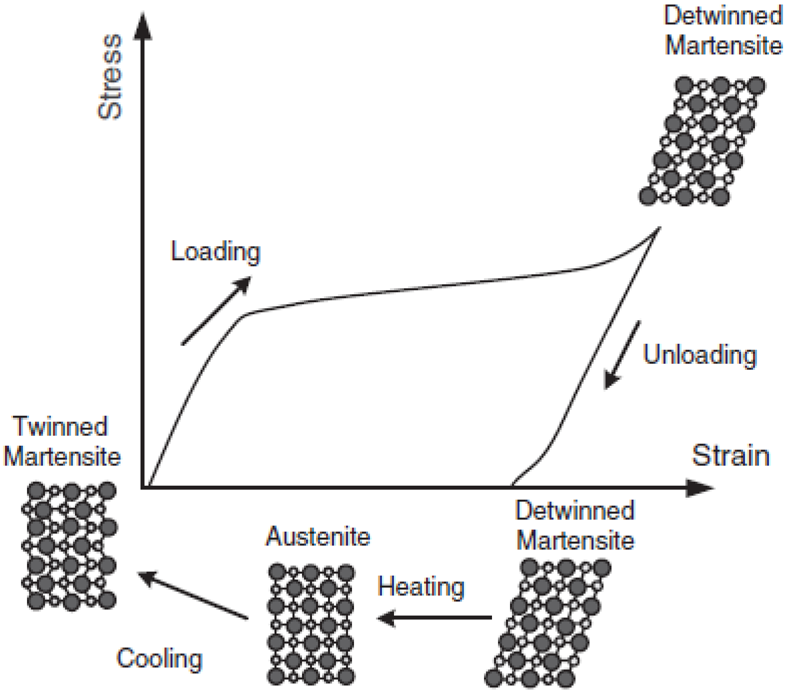

Figure 4.7: Stress-Strain diagram in One-Way Shape Memory Effect transformation and different SMA crystal structures [2].

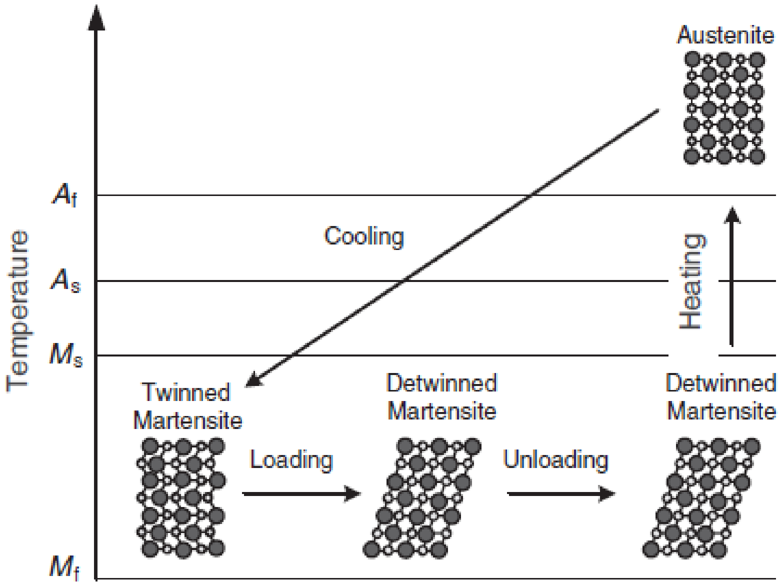

Figure 4.8: One-Way Shape Memory Effect crystal structure transformation, with changing of temperature [2].

- The Two-Way Shape Memory (b): the alloys in this case can memorize two different shapes, each of those characterized by a different crystal phase. To obtain this effect, the alloys must be treated by forcing them with a cyclic load, in the Martensite phase, to assume a certain shape. The material can change its shape just by experiencing temperature changes, as shown in figure 4.9 [4, 5, 9].

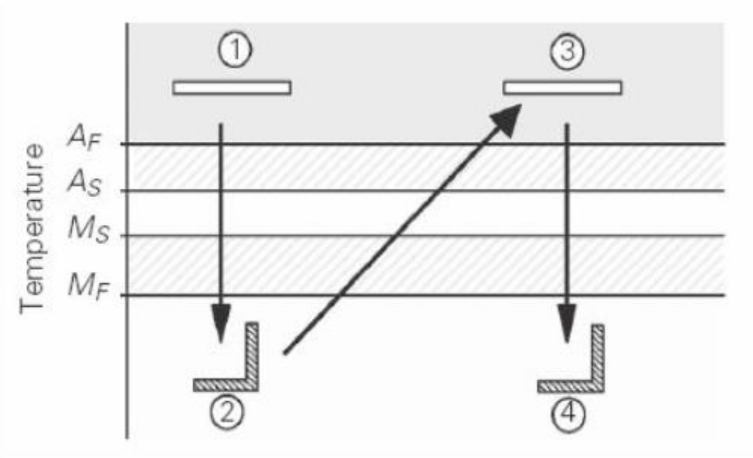

Figure 4.9: Two-Way Shape memory Effect temperature dependence [5].

4.4 Super-Elastic Effect

When the Shape Memory Alloy is exposed to a temperature above Af, it is in Austenite phase. When a sufficiently high stress is applied to the material (without changing the temperature), it transform into Detwinned Martensite. When the load is released the alloy returns to the Austenite phase, which results in the complete shape recovery and a substantial hysteretic loop. If the temperature is below Af but above As, there will be only partial recovery of the original shape. Also, if the temperature is above Md, the material is stabilized in the austenite phase and the martensitic transformations cannot be induced by an applied load [2, 9]. Figure 4.10 shows the typical stress-strain diagram when experiencing the Super-Elastic Effect.

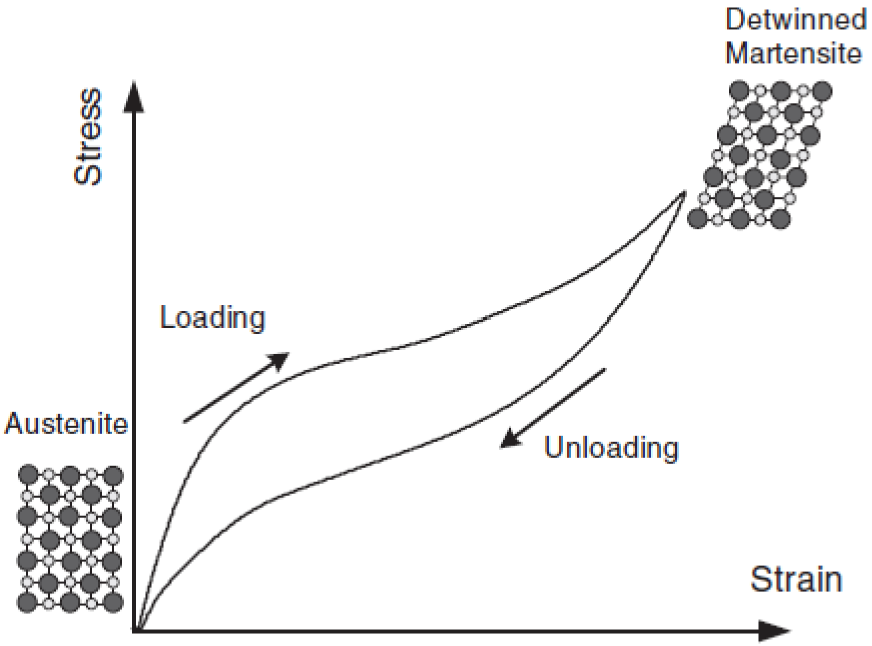

Figure 4.10: Stress-Strain diagram shows the Super-Elastic Effect [2].

4.5 Nitinol

Since the discovery of Nitinol, other alloys with the same properties were discovered. However, due to their exceptional properties, Nickel-Titanium (Ni-Ti) and Copper (Cu) based alloys are the ones most frequently used.

4.5.1 Composition

Nitinol is a binary system based on an almost equi-atomic compound of Nickel and Titanium, that shows shape memory effect when the percentage of Nickel is around 48-52%. Sometimes there could be intermetallic and solid intrusions, such as oxygen, nitrogen, hydrogen and carbon, which are responsible for several alterations of the physical and mechanical properties of the alloy. Besides the alteration of the state of purity of the alloy, these intrusions may alter the typical temperatures of phase transformation, the biocompatibility and the degradation of the mechanical properties of the alloy. Oxygen and nitrogen have damaging effects on the ductility of the material, hydrogen causes variations in the temperature of phase transformation, and reduces the ductility of the alloy. Moreover, if chromium, manganese, iron, vanadium, niobium or cobalt are present in the Nitinol alloy, they may cause a decrease in the value of Ms temperature. In contrast, if copper, platinum, palladium, hafnium or zirconium are present in the Nitinol alloy, they may cause an increase of Ms temperature [2, 3].

4.5.2 Mechanical Properties

Nitinol is the most studied alloy in the past years, and in general it shows better characteristics than the other shape memory alloys. These characteristics include:

- Hysteretic damping.
- High strength.
- High reliable energy dissipation (based on a solid phase transformation).
- Excellent fatigue properties (low-cycle and high-cycle).
- Excellent wear, abrasion and corrosion resistance.
- Excellent re-centering ability [2-4].

The Ni-Ti based alloys, compared with the other SMAs, show superior mechanical properties: the tensile strength exceeds 895 MPa, the elongation reaches 50 - 60% at failure and withstanding 8% strain in the martensitic form, which can be fully recovered by heating [7]. Table 4.4 shows the typical mechanical properties of Ni-Ti based alloys.

Young's Modulus	Austenitic	~ 83 GPa
	Martensitic	~ 28 - 41 GPa
Yield Strength	Austenitic	195 - 690 MPa
	Martensitic	70 - 140 MPa
Ultimate Tensile Strength	Fully Annealed	895 MPa
	Work Hardened	1900 MPa
Poisson's Ratio	0.33	

Table 4.4: Nitinol Mechanical Properties [2].

4.5.3 Physical Properties

The table 4.5 shows the physical properties of Nitinol, such as the melting point, density, thermal conductivity, coefficient of thermal expansion and specific heat.

Melting Point	1573K	
Density	6.45 g/cm^3	
Thermal Conductivity	Austenitic	0.18 W/cm-K
	Martensitic	0.086 W/cm-K
Coefficient of thermal expansion	Austenitic	11.0 x 10^{-6} / K
	Martensitic	7.0 x 10^{-6} / K
Specific Heat	0.20 cal/g-K	

Table 4.5: Nitinol Physical Properties [2].

4.5.4 Fatigue Behaviour

The shape memory alloys are frequently subjected to cyclic loading. In Civil Engineering applications, it could be due for example to the cyclic nature of the seismic load. As with other materials, also the mechanical properties of Nitinol exhibit degradation due to the formation and propagation of micro-cracks and faults after repeated use. The level of reversible deformation diminishes and the dimension of hysteresis loop that characterizes the super-elastic behaviour is reduced. The fatigue behaviour of these materials is very complex because of the non-linear stress-strain behaviour (Super-Elasticity), and the crystal structure dependence from the temperature [2].
There are two types of fatigue behaviour:

- With *Controlled Strain*: if the material is alternately deformed between two different macroscopic configurations. In this case a Nitinol bar can tolerate about 1000 cycles at 4% to 12% imposed strain and 10.000 cycles at 1% imposed strain, unlike other metallic bars that can tolerate 1000 cycles at 1% imposed strain before fracture.
- With *Controlled Tension*: if the material undergoes a controlled loading. In this case the degradation of the material properties occurs more quickly than in the precedent case [10].

The combined action of both behaviours is the most frequent, increasing even further the potential degradation of the material properties. Table 4.6 shows the maximum strain or stress cycles that Nitinol can undergo without experiencing significant reduction of the mechanical properties.

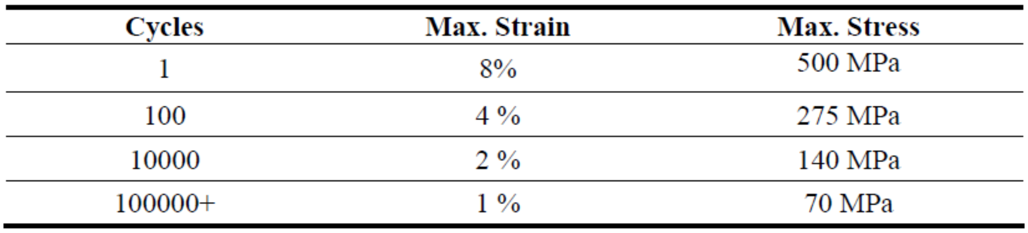

Cycles	Max. Strain	Max. Stress
1	8%	500 MPa
100	4 %	275 MPa
10000	2 %	140 MPa
100000+	1 %	70 MPa

Table 4.6: Nitinol Fatigue Stress-Strain Behaviour [2].

Other effects of the cyclic loading are the increase of residual deformation and the reduction of the dissipated energy, i.e. the hysteretic loop area. The figure 4.11 shows the stress-strain curve of a 2 mm diameter wire tested under cyclic tension [2].

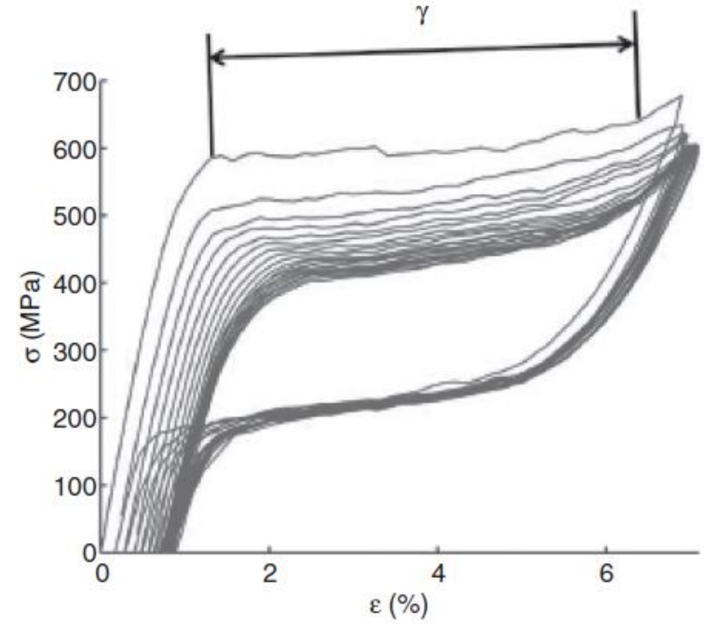

Figure 4.11: Nitinol Stress-Strain response during a tensile fatigue loading test [2].

4.5.5 Temperature Effect

Extensive experimental testing has been conducted in recent years regarding the characterization of the temperature effect on the mechanical behaviour of Nitinol wires [2]. The most interesting discovery was that the temperature influences the transformation phase's critical stress: in particular, as shown in figure 4.12, an increase in temperature corresponds to a linear increase of the transformation stress. Furthermore, it was observed that the initial stiffness does not change due to the temperature increase or decrease. The figure 4.12 shows the stress-strain diagram at various temperatures: it is possible to observe that in a -50° C to 0° C temperature range, the material shows Shape Memory Effect, and in a 0° C to +40° C temperature range it shows Pseudo-Elastic Behaviour. After exceeding the temperature of +40 C° the alloy manifests residual deformation because the Martensite transformation cannot be stress-induced after this temperature point.

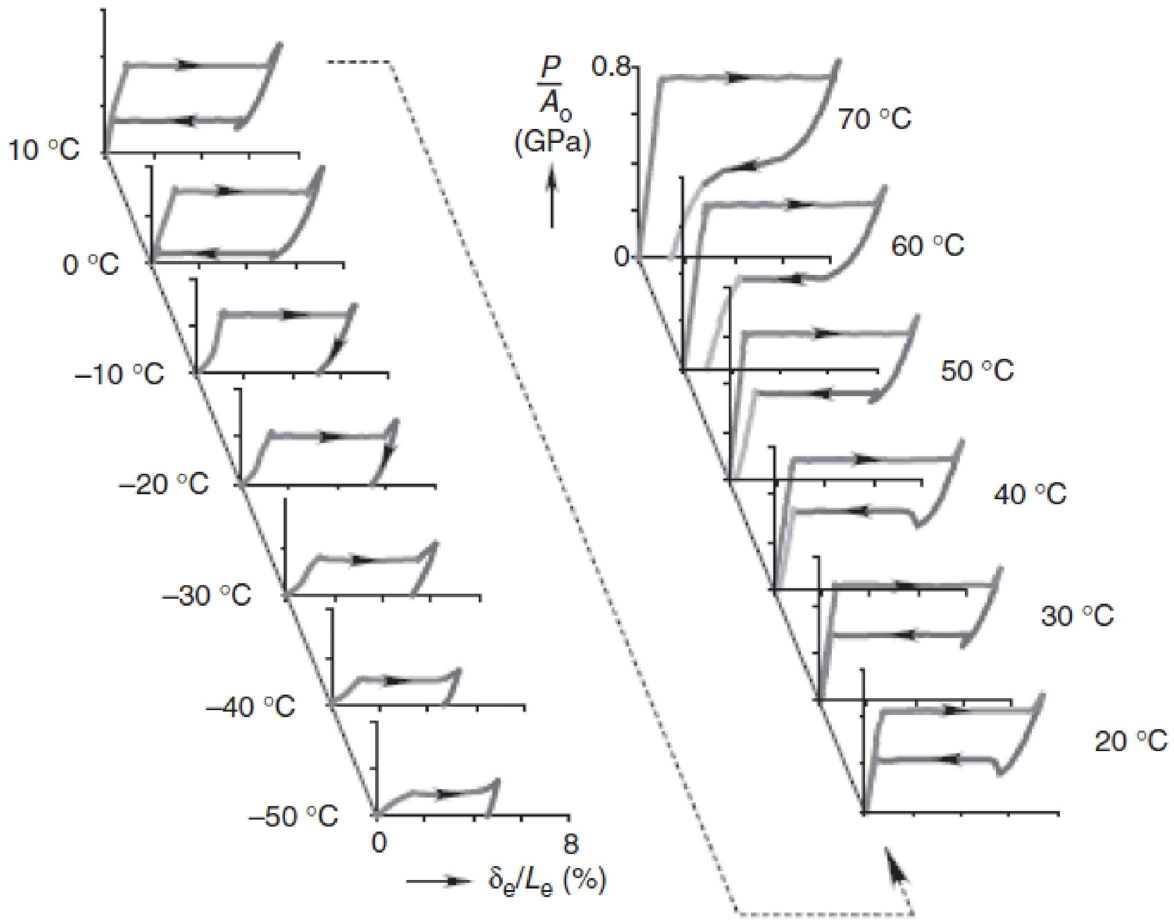

Figure 4.12: Nitinol Stress-Strain diagrams at various temperatures [2].

4.5.6 Corrosion and Aging

Ni-Ti alloys exhibit higher corrosion and aging resistance than steel and the other Shape Memory Alloys. They have a good corrosion resistance behaviour due to the presence of a passive film that has the effect of a protective layer [2].

4.6 Seismic Applications

Shape Memory alloys possess extraordinary properties as previously mentioned, which make them a smart material for civil engineering applications. Nevertheless, the number of field application in civil engineering are very limited due to the high cost and the small size of SMAs components [7; 9]. Some interesting uses of Nitinol alloys are in seismic applications, such as in the retrofitting of historical buildings damaged by earthquakes as well as new buildings or bridges after damaged. Considering the seismic retrofit approaches and methods previously studied, Shape Memory alloys can be used in many diverse applications, such as for the improvement of the behaviour of isolators and dissipators, exploiting the Martensitic Shape Memory Effect. As previously discussed, this phase has a large damping capacity but requires external heat to return to the original shape. Alternatively, Austenitic Super-Elastic Effect can be of interest, although it has smaller damping capacity but provides strong re-centring forces to restore the initial position of the structure. In this chapter some examples, already studied by other researchers, will be discussed [2, 7, 15].

4.6.1 SMA Base Isolator Devices

A SMA *Base Isolator Devices* represent interesting passive structural control mechanisms which allow to reduce the accelerations in structures due to different horizontal loads. These devices are installed between the ground and the super-structure, to assemble an uncouple system. The base isolator provides variable stiffness to the structure while it filters the seismic energy transferred from the ground to the super-structure, reducing displacements, forces and damage in the structure.

Base isolators include: SMA bars for highway bridges, SMA wire re-centring devices for civil buildings and SMA spring isolation systems (figure 4.13) [15].

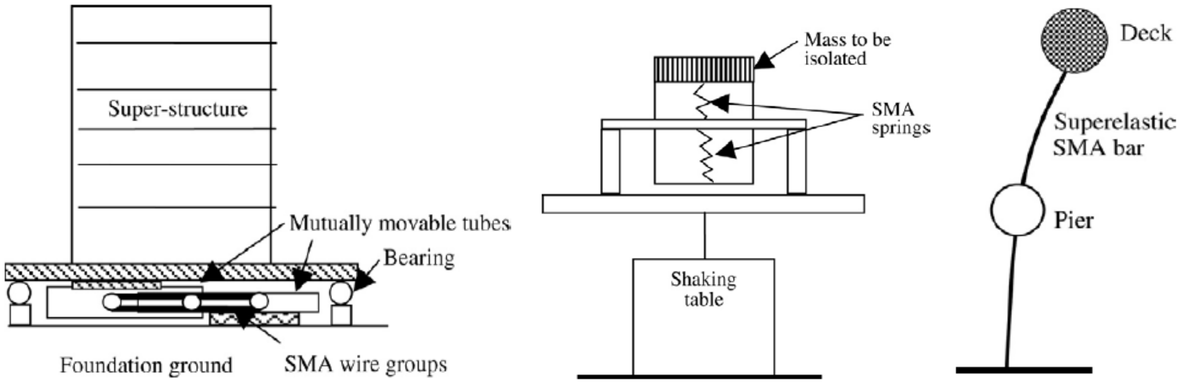

Figure 4.13: SMA base isolator devices [15].

Dolce [15] developed and tested a full-scale Nitinol *wire-based isolation system* to study the feasibility of Nitinol wires in seismic applications. The device, shown on figure 4.13 (in the middle), was composed by a super-elastic SMA wire wounded around some stubs. When there was a reciprocal movement between the super-structure and the foundation, the wire was elongated and the vibration magnitude was damped by the wire. The tests have shown that the isolation system was able to filter vibration energy from the ground to the super-structure, while showing variable stiffness with the load intensity.

Wilde [15] investigated a *SMA bars isolation system* for elevated highway bridges. For small excitation levels, the isolation system acts as a rigid and firm link between the deck and the pier. For a medium excitation level, the SMA bars undergo stress-induced Martensitic phase change, reducing its tensile stiffness and also the stiffness of the system, allowing greater displacement. After several loading cycles, the maximum displacement is a fifth comparable with the conventional isolation system. Bridges equipped with SMA isolation devices show, in general, lower damage levels than bridges with common isolation devices.

4.6.2 SMA Energy Dissipation Devices

SMA *Energy Dissipation Devices* are integrated in the structure and absorb vibration energy due to their stress-strain hysterical behaviour. Dissipation devices include: diagonal braces for frame structures, dampers for supported and cable-stayed bridges, restrainer bars, connection elements for columns and retrofitting devices for historical buildings (figure 4.14) [15].

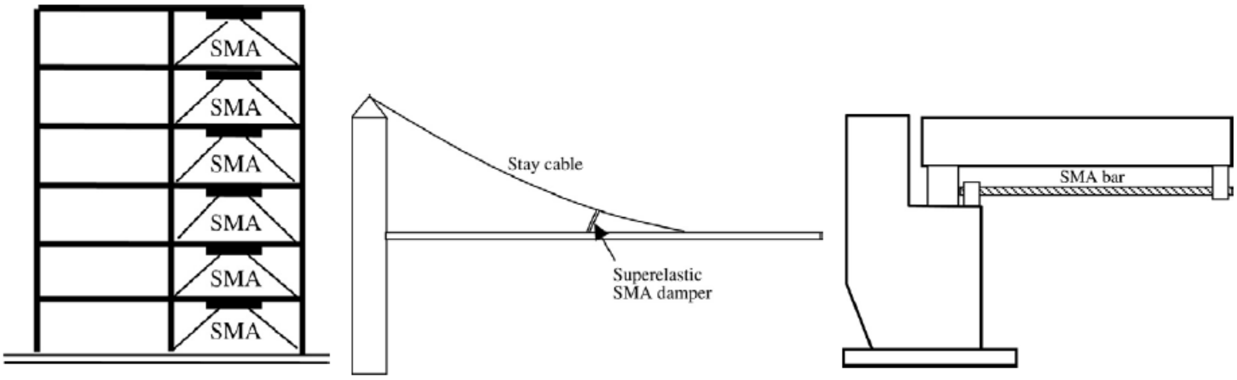

Figure 4.14: SMA energy dissipation devices [17].

To demonstrate the efficacy of SMAs as *diagonal braces* in frame structures, some studies have been conducted by various researchers [2]. Gilbert and Rasmussen in 2012 [12] tested Drive-In Steel Storage Racks subjected to horizontal loads (figure 4.15) with different spine and plan bracing configurations. The numerical studies demonstrated that the use of these materials can reduce the inter-story drift and can limit the residual drift in steel buildings.

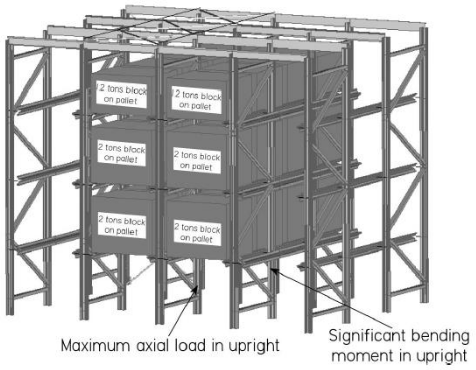

Figure 4.15: SMA diagonal braces in frame structure test [12].

SMA dampers can be used to mitigate the wind induced vibrations in cable-stayed bridges. Casciati in 2008 [2] studied the feasibility of an SMA wire-steel cable system that consists of a steel cable with SMA super-elastic wire wrapped several times around the cable. The tests have shown that this smart system increases the fundamental frequencies and the damping coefficient while decreasing the amplitude of the vibrations. Faravelli in 2010 [2] developed a hybrid control system that combined SMA wrapped wires and an open loop control strategy to further improve the behaviour of stay-cables when they are subjected to strongly non-linear vibrations.

To reduce the relative displacement in multi-span simply supported bridges, DeRoches and Delemont in 2002 [16], tested *SMA restrainer bars and cables* applied on hinges and abutments (figure 4.16). These devices can be designed to provide sufficient stiffness and damping to limit the relative displacement of the deck during seismic events. The use of SMA restrainers can contribute to a reduction of 42% of the maximum relative displacement, which is significantly higher than the contribution of steel restrainer cables that reach reductions of 24%. The elastic stress-strain behaviour of SMA restrainers allows them to undergo large deformations while remaining elastic. In addition the super-elastic properties SMA restrainers results in efficient energy dissipation at the hinges. The increased stiffness of the SMA restrainers at large strains provides additional restraint to limit the relative openings in a bridge under seismic events.

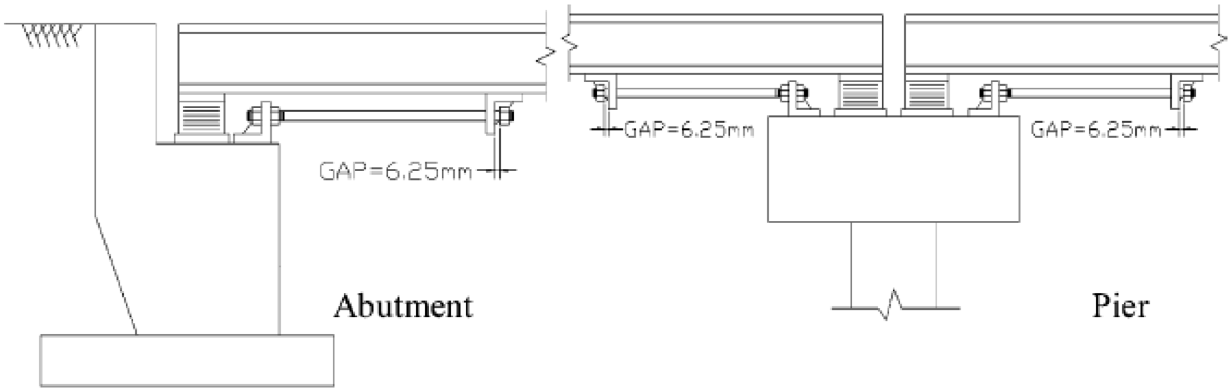

Figure 4.16: SMA restrainer bars in the abutment and column of a bridge [16].

4.6.3 Retrofitting of Historical Buildings

Another example of a structural application of SMA devices is the Basilica of San Francesco in Assisi [7]: this historical building underwent strong damage after the 1997 earthquake. The aim of the retrofitting was to limit the acceleration and the forces transmitted from the root of the main structure to the masonry gable, and to induce energy dissipation to the whole structure. To solve this problem, the gable was completely disconnected from the roof and was linked to the roof again by SMA devices (SMAD), as shown in figure 4.17.

Figure 4.17: Basilica of San Francesco in Assisi's SMA device [7].

These devices have been studied in the past years by a large number of researchers: Ma and Yam in 2011 [2], Suduo and Xiongyan in 2007 [2], Zuo in 2008 [2] and others. SMA-based devices have been developed with the purpose to isolate and control the vibration of the building.

The device employs pre-stressed super-elastic wires, which are strained only in tension for re-centring capability. Additional wires are used for an additional energy dissipation. The SMADs work for normal horizontal loads (wind and minor earthquakes) with the linear elastic behaviour and small displacement (Patch I), and in case of major earthquake the SMA critical stress will be exceed and the wires will lose their stiffness (Patch II). The device allows for higher displacements and permits to activate the damping of the connected masonry structure while acting as load limiter. Hysteresis is produced by cycle loading and unloading, and when the super-elastic plateau is exceed, the SMA increases its stiffness (Patch III), and prevents the gable from tearing of the main structure in case of an unexpected strong earthquake [7; 2]. The load-displacement diagram of these devices is shown in figure 4.18.

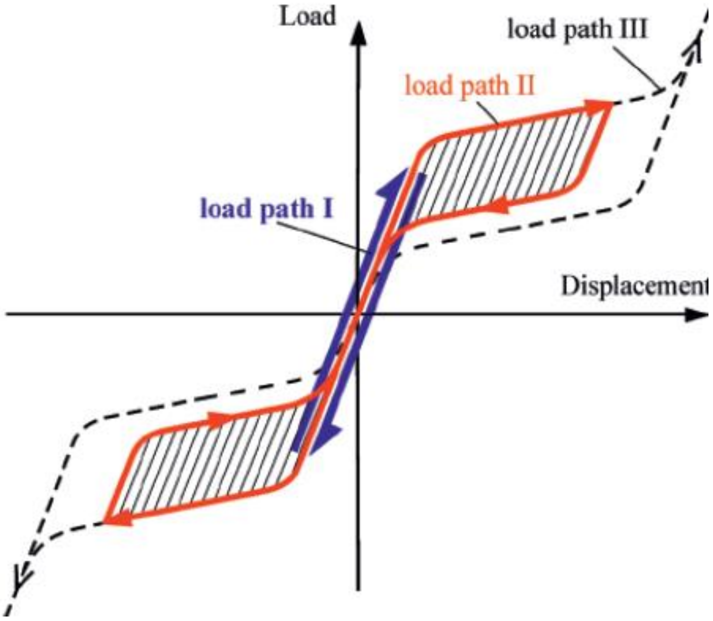

Figure 4.18: Load-Displacement response of the SMA devices in Basilica of San Francesco [7].

4.6.4 SMA as Reinforcement for Concrete Beams and Columns

Another SMAs application tested in 2013 by A. Abdulridha et al. [14] (details on figures 4.19 and 4.20) consists of using SMA bars or wires as concrete reinforcement. The purpose of this test was to exploit the re-centring characteristic of the Shape Memory Alloys, and to develop a ductile reinforced concrete beam that can have optimal strength and displacement recovery response if subjected to reverse cyclic loading. The results have shown that under reverse cycling loading, reaching a plastic displacement value 9.5 times higher than the elastic displacement value, the SMA reinforced beams recovered 85% of the mid-span displacement, while the conventional beam only recovered 26%. Under cyclic loading with a plastic displacement value 6.5 times higher than the elastic displacement value, the SMA and conventional reinforced concrete beams recovered respectively 80% and 17% [14].

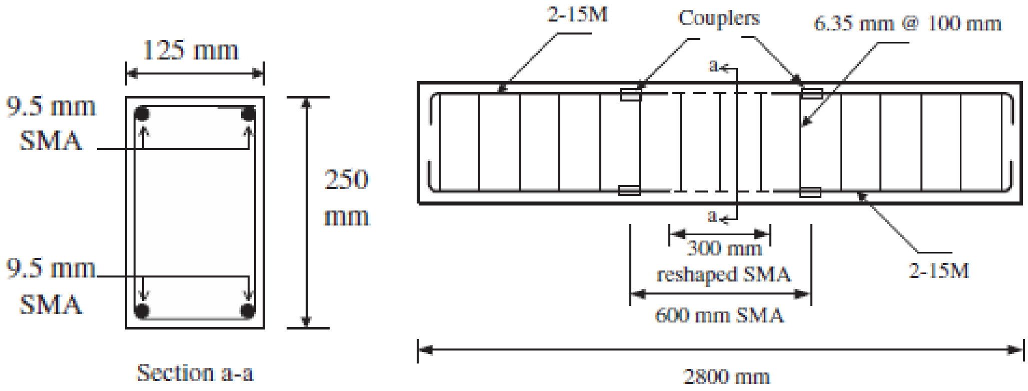

Figure 4.19: Details of the specimens (section and reinforcement arrangement) [14].

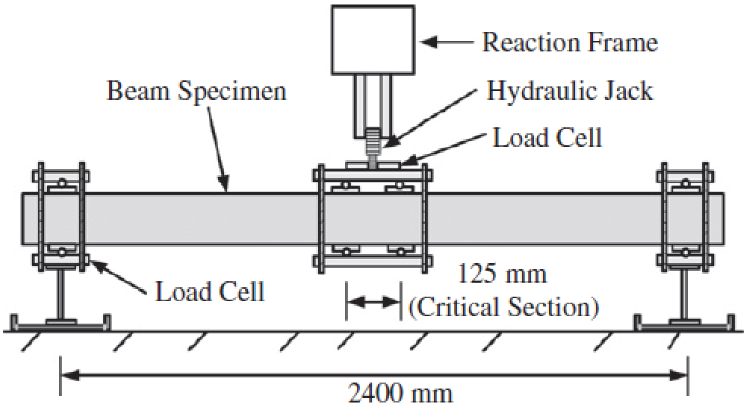

Figure 4.20: SMA reinforced concrete beam bending test [14].

In order to reduce the residual drift and to ensure the serviceability and safety in bridge columns after a strong earthquake, Mostafa Tazarv and M. Saiid Saiidi, in 2013 [13], developed an analytic modelling method to estimate residual displacement in SMAs reinforced concrete. A full scale model was tested on a shaking table at the University of California (San Diego) for the analytic model verification. The SMA bars were used only in the region of the plastic hinge of the column. Details of the specimen are shown in figure 4.21. As shown in figures 4.22 and 4.23, the results obtained have revealed that the SMA reinforced column exhibited a residual displacement 80% lower than the conventional column.

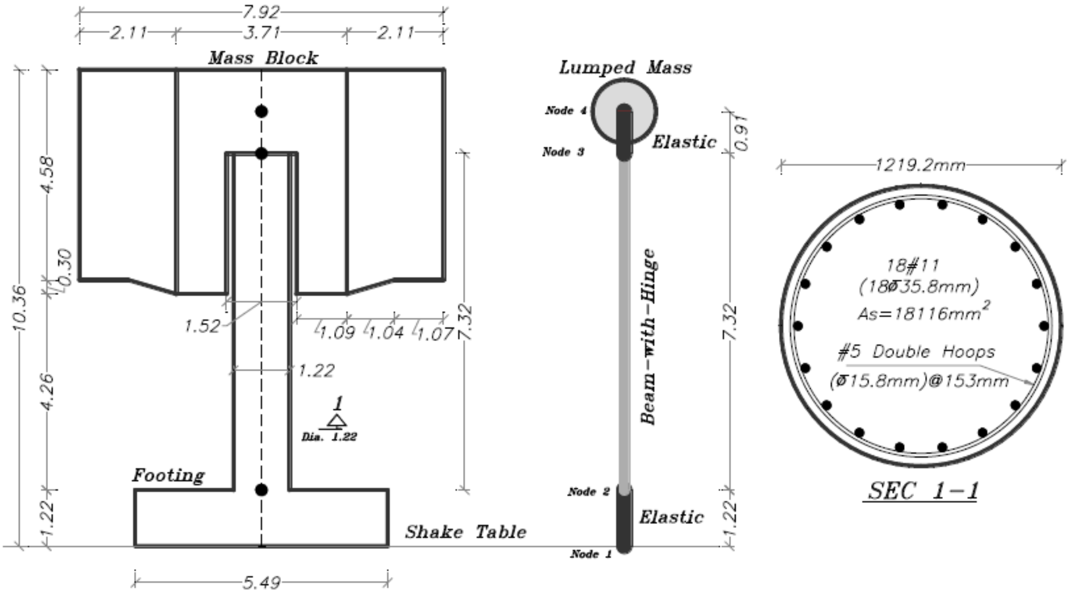

(a) (b) (c)

Figure 4.21: SMA reinforced concrete column test, (a) full-scale column model, (b) analytic model, (c) full-scale column section [13].

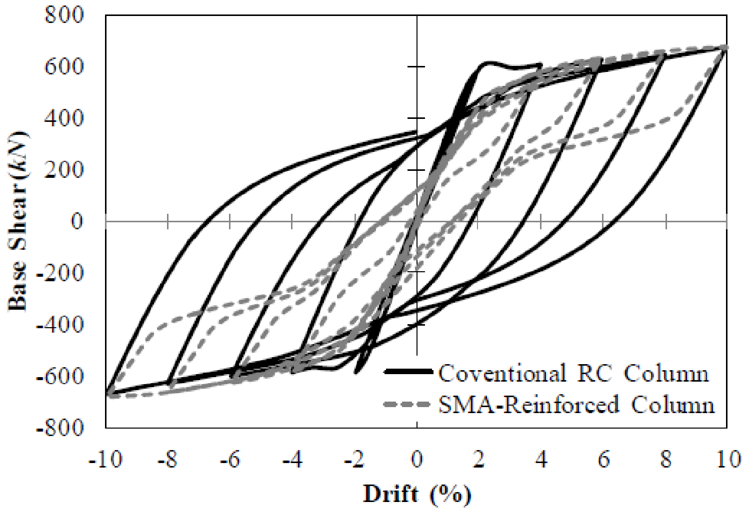

Figure 4.22: Load-Drift responses of conventional and SMA reinforced concrete columns [13].

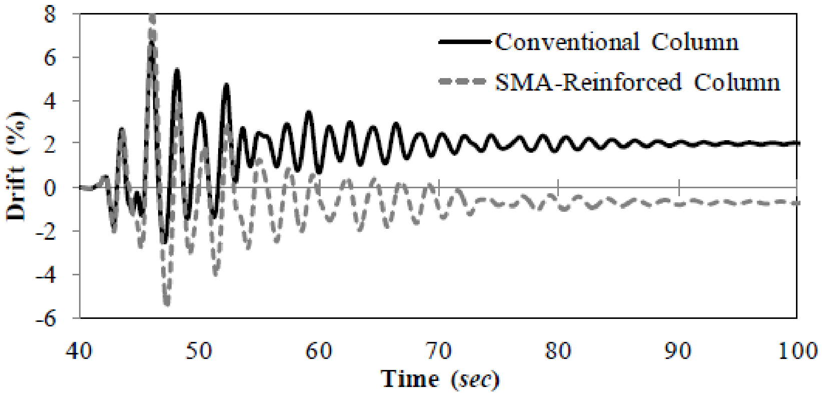

Figure 4.23: Drift-Time responses of conventional and SMA reinforced concrete columns [13].

4.7 Modelling of SMA

4.7.1 Nitinol Bars and Wire Modelling

The complex behaviour of Nitinol under cycling loading and temperature changes should be simplified in order to design and verify the contribution of the Nitinol component utilized in a structure. Tazarv & Saiidi [13] proposed a non-linear behaviour for Nitinol wires and bars, as shown in figure 4.24 and table n. 4.7.
The non-linear model consist of:

- A first linear branch, with a constant slope (k1) which represents the Nitinol behaviour in the Austenite phase. After one loading and unloading cycle, which subjects the material to a stress incrment lower than fy (yeld stress point), the material will return to the original configuration without any plastic deformation.
- After surpassing the yield stress point, the material will behave according to another linear branch with constant slope (k2) until a total strain of 6% is reached, and the material assumes the Detwinned Martensite phase. By releasing all the load the material will follow initially a linear unloading path with k1 slope (the amplitude of this branch is β fy), and then it will follow another linear path with k2 slope until it will reaches the yield stress point. Additional unloading will cause the return of the specimen to the original shape without any plastic deformation, following a linear stretch with k1 slope.
- At a load increase that results in an imposed strain higher than 6%, the material will follow a linear stretch with constant slope (k3) until an ultimate point is reached, set at 10% strain. Subsequent unloading of the specimen will result in plastic deformation.

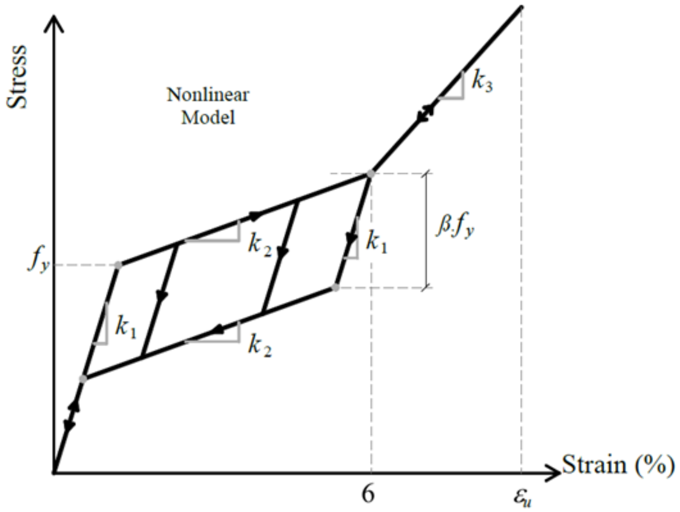

Figure 4.24: Stress-Strain non-linear model for Super-Elastic Ni-Ti Alloys [13].

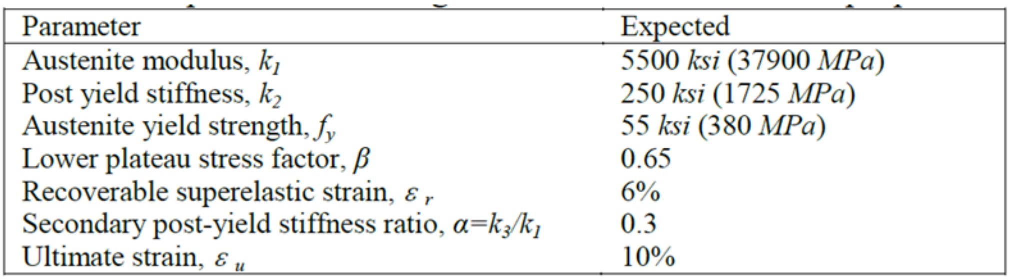

Parameter	Expected
Austenite modulus, k_1	5500 ksi (37900 MPa)
Post yield stiffness, k_2	250 ksi (1725 MPa)
Austenite yield strength, f_y	55 ksi (380 MPa)
Lower plateau stress factor, β	0.65
Recoverable superelastic strain, ε_r	6%
Secondary post-yield stiffness ratio, $\alpha=k_3/k_1$	0.3
Ultimate strain, ε_u	10%

Table 4.7: Proposed parameters for the non-linear model of Nitinol bars [13].

4.7.2 Modelling of SMA Reinforced Concrete

The use of SMA bars and wires as reinforcement in concrete beams and columns implies the formulation of a specific constitutive model for their design and verification. Elbahy et al [17] proposed a model for the calculation of the ultimate resistant moment and the moment-curvature relationship. The assumptions are: plane sections remain plane after deformation, ultimate (confined) concrete strain is 0.0035, compressed concrete follows the stress-block behaviour and concrete tensile resistance is ignored. These assumptions are summarized by the stress-strain diagrams for concrete, steel and SMA bars presented in figure 4.25, 4.26 and 4.27.

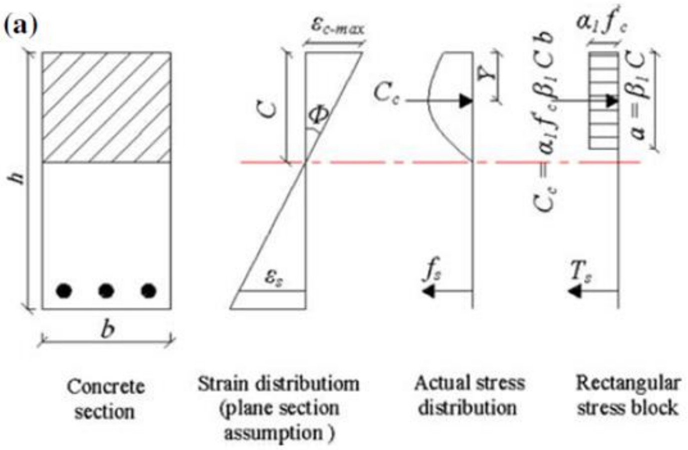

Figure 4.25: Assumptions of the model [17].

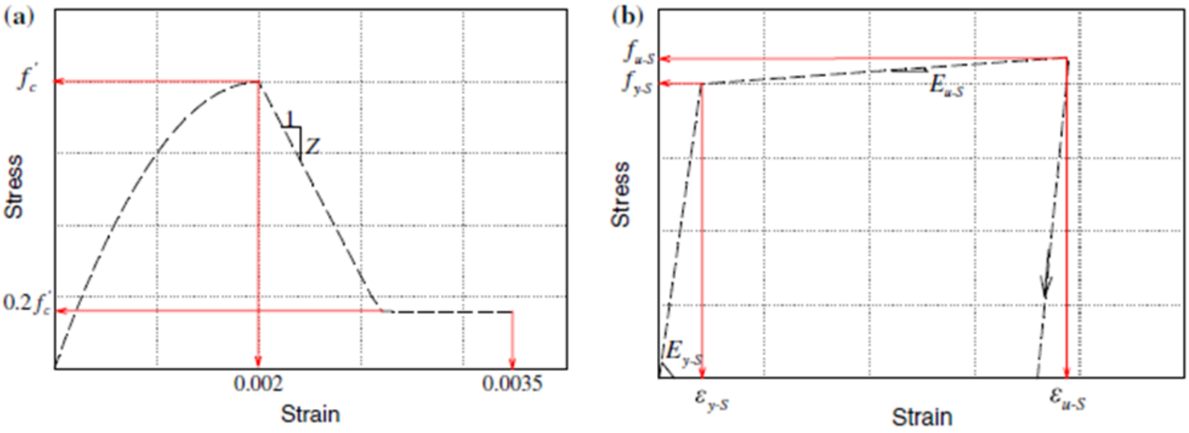

Figure 4.26: Stress-strain diagrams for concrete (a) and steel (b) [17].

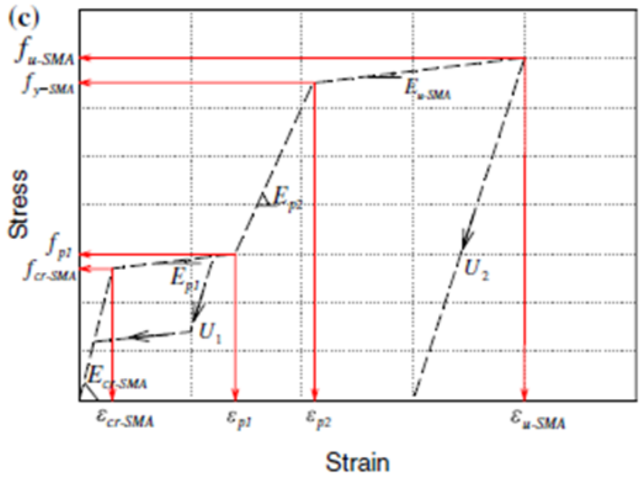

Figure 4.27: Stress-strain diagrams for SMA bars (c) [17].

It is possible to calculate the moment-curvature diagram for a section, considering for example a fibre model for composite sections (figure 4.28).

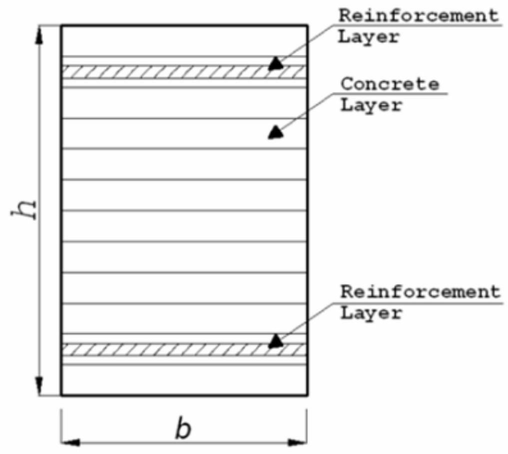

Figure 4.28: concrete section fibre model [17].

The same authors proposed the model shown in figure 4.29 for SMA bridge devices, which essentially considers the same assumption as the one previously referred [17].

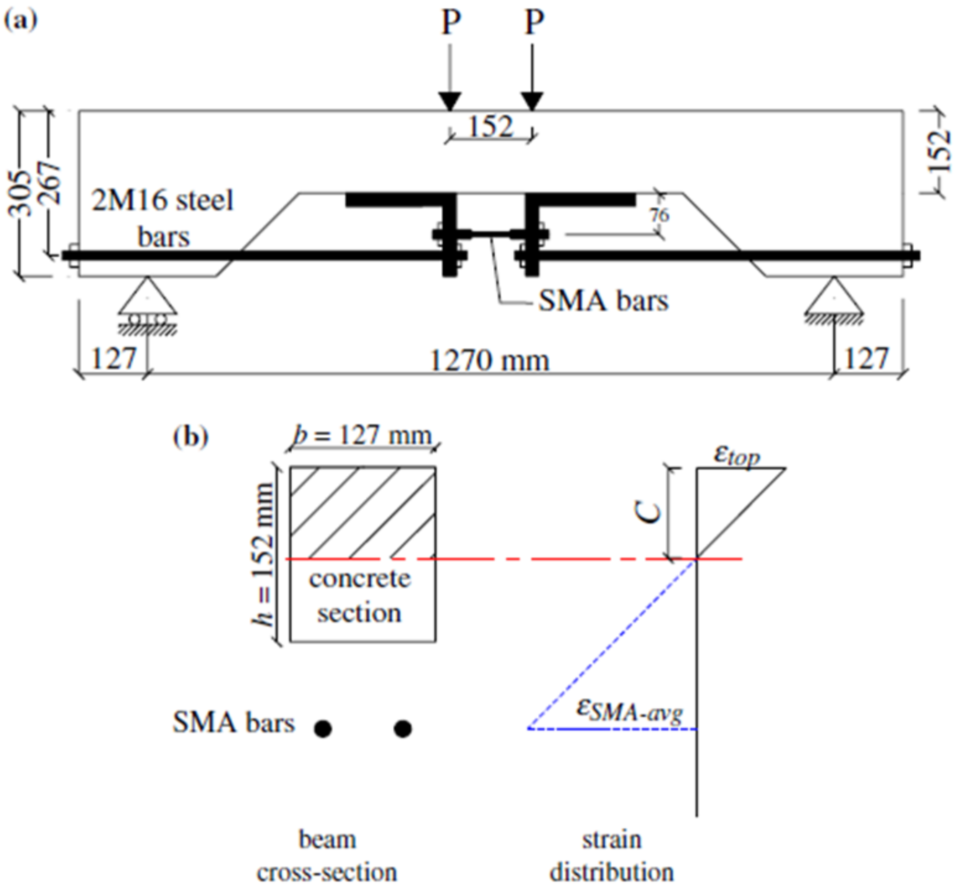

Figure 4.29: SMA devices (a) and their beam cross-section and strain distribution model (b) [17].

4.7.3 Modelling of SMA Devices

A constitutive model has been developed by Cardone et al. [18] to describe the SMA devices super-elastic behaviour during seismic events. The numerical model has been created by assembling a series of non-linear springs. Four springs have been used for represent the behaviour of these devices, as shown in figure 4.30. An elastic spring with an initial gap (GAP1) to allow the thermal movement of the bridge in standard working condition and in the absence of seismic loads is connected in series with three other springs. This device corresponds to a multi-linear spring (MLE) which is used to describe the non-linear elastic behaviour of the SMA device, connected to a spring with a non-linear cyclic behaviour (PW) which is used to account for the energy dissipation capacity of the SMA device, and to an elastic spring element with gap (GAP2) that is used to capture the increase of stiffness of the SMA device at the end of the phase transformation from Austenite to Detwinned Martensite.

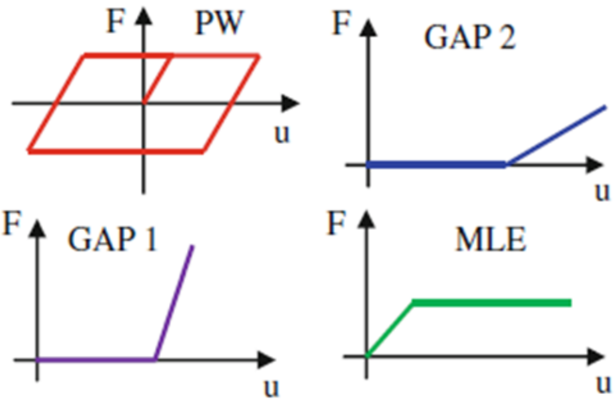

Figure 4.30: four different sprigs utilized in the model, and the force-displacement diagram of the SMA device [18].

4.8 Conclusion

In this chapter the main characteristics of Shape Memory Alloys, and in particular of Ni-Ti alloys, have been discussed. Super-Elastic and Shape Memory Effects are two interesting features that can be used in civil engineering applications, and in the literature it is already possible to find some interesting examples and applications such as seismic dissipators, restrainers and isolators. The complex non-linear temperature dependent stress-strain behaviour of these materials could represent an obstacle for the design, but it is also possible to simplify it, as discussed previously. The design of structural elements showing an increase of strength, ductility, dissipation of energy and the ability to recover the initial deformation is therefore not necessarily too complex.

In the following chapter, the tensile behaviour of two different types of Nitinol wires will be tested and the behaviour of a reinforced composite material that can be used in civil engineering applications will be investigated. Examples of possible application are in the design of critical structures or for seismic retrofit of old structures, exploiting the Shape Memory or the Super-Elastic Effects.

Bibliography

[1] Otsuka and Wayman (1999); Shape Memory Material; Cambridge University.

[2] O. E. Ozbulut, S. Hurlebaus and R. Desroches (2011) ; Seismic Response Control Using Shape Memory Alloys: A Review; Journal of Intelligent Material Systems and Structures.

[3] Debbarma. S.R, Saha.S (2012); Review of Shape Memory Alloys applications in civil structures, and analysis for its potential as reinforcement in concrete flexural members; INTERNATIONAL JOURNAL OF CIVIL AND STRUCTURAL ENGINEERING Volume 2, No 3.

[4] Jaronie Mohd Jani et al. (2013); Materials and Design, A review of shape memory alloy research, applications and opportunities.

[5] L.G. Machado, M. A. Savi (2003); Medical applications of shape memory alloys; Brazilian Journal of Medical and Biological Research.

[6] D. J. Hoh, et al. (2009); Shape memory alloys: metallurgy, biocompatibility, and biomechanics for neurosurgical application.

[7] M. Motavalli et al. (2009); Shape memory alloys for civil engineering structures – on the way from vision to reality; Architecture Civil Engineering Environment, The Silesian University of Technology No. 4.

[8] Reginald DesRoches (2002); Application of Shape Memory Alloys in Seismic Rehabilitation of Bridges, Final Report for Highway IDEA Project 65; Georgia Institute of Technology.

[9] Federica Daghia (2008); Active fibre-reinforced composites with embedded shape memory alloys; University of Bologna.

[10] P. Filip et al. (2001); Titanium-Nickel Shape Memory Alloys in Medical Applications; eds. Titanium in Medicine, ed. Springer.

[11] V.B. Krishnan (2004); Design, Fabrication and testing of a Shape Memory Alloy based Cryogenic Thermal Conduction Switch; University of Central Florida.

[12] Gilbert and Rasmussen (2012); Drive-In Steel Storage Racks: Stiffness Tests and 3D Load-Transfer Mechanisms; American Society of Civil Engineers.

[13] Mostafa Tazarv & M. Saiid Saiidi (2013); Analytical Studies of the Seismic Performance of a Full-Scale SMA-Reinforced Bridge Column; International Journal of Bridge Engineering (IJBE), Vol. 1, No. 1, pp. 37-50.

[14] Alaa Abdulridha et al. (2012); Behavior and modeling of superelastic shape memory alloy reinforced concrete beams; Engineering Structures, journal homepage: www.elsevier.com/locate/engstruct.

[15] G. Songa, N. Maa, H.-N. Lib (2006); Applications of shape memory alloys in civil structures; Engineering Structures 28.

[16] R. DesRoches, M. Delemont (2002); Seismic retrofit of simply supported bridges using shape memory alloys; Engineering Structures 24.

[17] Y. I. Elbahy, M. A. Youssef, M. Nehdi (2009); Stress block parameters for concrete flexural members reinforced with superelastic shape memory alloys; Materials and Structures.

[18] Donatello Cardone et al. (2001); Numerical Studies on the Seismic Retrofit of Bridges Using Shape Memory Alloys; ASM International.

5. Experimental Research on ECC and NiTinol

5.1 Experimental Tests on ECC Mixtures

5.1.1 Mixture Design

Having in mind the applications described in the previous chapters, with the purpose to select the best composites for subsequent experiments, ten different mixtures of ECC have been developed. Two different types of cements have been used: Portland 32.5N and 42.5R were used to obtain 5 different composites by varying the fraction of Cement, Fly Ash, Water, Viscosity Modified Agent (VMA), while keeping constant the fraction of Sand, Limestone Filler and Super Plasticizer (SP), and the amount in terms of percentage by volume of the PVA fibers. The main characteristics of the mixtures are detailed subsequently.

5.1.2 Mixing Procedure

In order to obtain consistent experimental results, the mixing procedure was kept similar for all mixtures. All the materials were keep away from water or weathering, which can alter their performance (especially PVA fibres and Cement). The procedure included the following sequence of steps:

- Firstly all the materials were collected and measured; the quantities are registered in tables 5.1 and 5.2; all the solid materials were then put in a bowl (cement, fly ash, sand, filler and VMA).
- The solid materials were then mixed in a mortar automatic mixer (see figure 5.1). After one minute, water and super plasticizer were added to the bowl while mixing, doing it quickly (from 5 to 10 seconds). This makes the kneading easier and avoids that part of the composite gets attached on the sides of the bowl.
- After about two minutes the mixing was stopped in order to test the fresh properties of the composite.
- The mixer was restarted and all the fibres were added; after 2 minutes of mixing, the fresh properties and homogeneity of the composite was checked by hand, making sure that it did not contain little pieces of aggregated powder (that represent non-mixed material) or little blocks of non-dispersed fibres. Then the fresh properties were tested, before casting.
- The specimens were cast while the mould was vibrated in the shaking table, in order to reduce the air entrapped in the mixture, and then covered it with cling film. After one day the mould was moved into the climatic chamber.

Figure 5.1: Automatic mixer, spoon and bowl used to mix the materials.

	Mixtures with Cement type 42.5R				
	M1-4R	M2-4R	M3-4R	M4-4R	M5-4R
Material	Mass [g]	Mass [g]	Mass [g]	Mass [g]	Mass [g]
Cement 42.5R	856	876	876	971	1091
Fly Ash	1713	1753	1753	1458	1091
Sand	300	307	307	340	382
Limestone Filler	300	307	307	340	382
Water	610	580	580	643	722
SP Sika 2002HE	32	33	33	36,7	41,2
VMA	1	1	2	2.1	2.4
Fiber PVA	52	52	52	52	52

Table 5.1: Mixtures with Cement type 42.5R.

	Mixtures with Cement type 32.5N				
	M1-3N	M2-3N	M3-3N	M4-3N	M5-3N
Material	Mass [g]	Mass [g]	Mass [g]	Mass [g]	Mass [g]
Cement 42.5R	856	876	876	971	1091
Fly Ash	1713	1753	1753	1458	1091
Sand	300	307	307	340	382
Limestone Filler	300	307	307	340	382
Water	610	580	580	643	722
SP Sika 2002HE	32	33	33	36.7	41.2
VMA	1	1	2	2.1	2.4
Fiber PVA	52	52	52	52	52

Table 5.2: Mixtures with Cement type 32.5N.

5.1.3 Fresh Behaviour

In order to evaluate the fresh properties of the mixtures, the mini-slump flow time and the mini-slump spread were measured. Both characteristics were evaluated using a mini-slump cone with the following dimensions: … the mixtures were spread on a damp Plexiglas plate. The following procedures were conducted:

- The mini-slump flow time (t20) was measured by registering the time taken by the mixture to reach a 20 cm diameter circumference drawn in the Plexiglas surface after lifting the flow cone.
- The mini-slump spread was measured by registering the dimensions of two perpendicular diameters (dxd) of the final spread mixture in the same Plexiglas surface.

These two measurements have been conducted before and after adding the PVA fibres to the mixtures. The obtained results are shown in tables 5.3 and 5.4.

	Mixtures with Cement type 42.5R				
	M1-4R	M2-4R	M3-4R	M4-4R	M5-4R
t20 (s)	no data	n.d.	n.d.	1.17	0.95
dxd (cm)	n.d.	n.d.	n.d.	35x36	33.5x33.5
t20 (s) (w/fiber)	n.d.	n.d.	n.d.	1.72	1.71
dxd (cm) (w/fiber)	21x21	22x22	n.d.	22.5x25.5	20.5x25

Table 5.3: Fluid properties of Cement 42.5R mixtures.

	Mixtures with Cement type 32.5N				
	M1-3N	M2-3N	M3-3N	M4-3N	M5-3N
t20 (s)	2	2,31	4	2,37	0,97
dxd (cm)	35x33	32.5x32	26.5x27.5	28.5x30	32.5x34
t20 (s) (w/fiber)	2.46	1.66	4.1	1.96	1.31
dxd (cm) (w/fiber)	23x27.5	21.5x25.5	21,5x26	25.5x25	30x30

Table 5.4: Fluid properties of Cement 32.5N mixtures.

The different properties in the fresh state in the hardened state are very sensitive to the amounts of each ingredient adopted in each mixture. The purpose of this experimental research was to better understand the effect of the quantity of water and viscosity modifying agent on the fresh properties of these composites. As shown in previous tables, the fresh behaviour of the composites is clearly more fluid when while the fibres are absent. In fact, after removing the cone the mixtures spread on the Plexiglas surface quickly, assuming a circular shape. After adding the fibres, the mixtures exhibit viscous behaviour, and more time is required for the mixtures to spread on the Plexiglas surface. The difference between the fresh behaviours before and after adding the fibres is shown in figure 5.2.

Mixture M3-3N	
Without fibers	With fibers
	
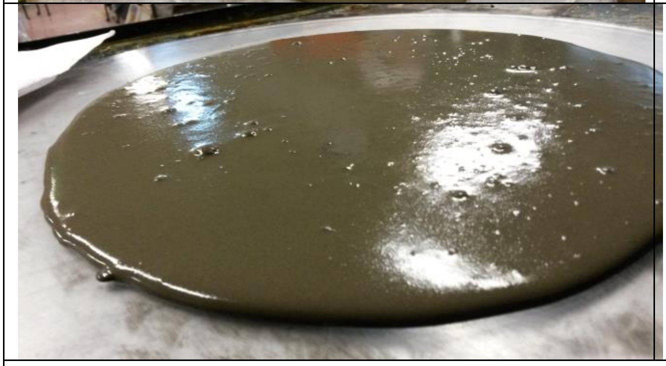	
Mixture M3-4R	
Without fibers	With fibers
	
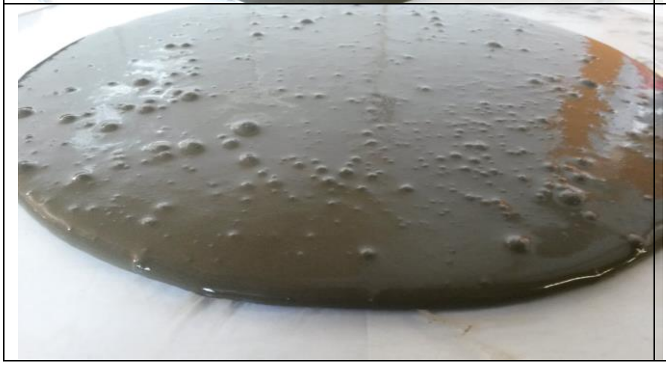	

Figure 5.2: M3-3N, and M3-4R mixtures before and after adding the fibres.

5.1.4 Hardened Behaviour in Tension

With the purpose of evaluating the hardened properties of the ten different mixtures in tension, specimens for tension tests have been casted in an acrylic mould, as shown in figure 5.3. For each mixture one plate 15 mm thick, 600 mm long and 150 mm wide was obtained. All plates were kept for 28 days in a climatic chamber at approximately 20°C. Afterwards, from each plate 1 cm to 4 cm on each side was cut out, as shown in figure 5.4. The plates were then rectified and cut to obtain 6 specimens. Each specimen was 65 mm wide, 200 mm long and 15 mm thick.

Figure 5.3: Acrylic mould.

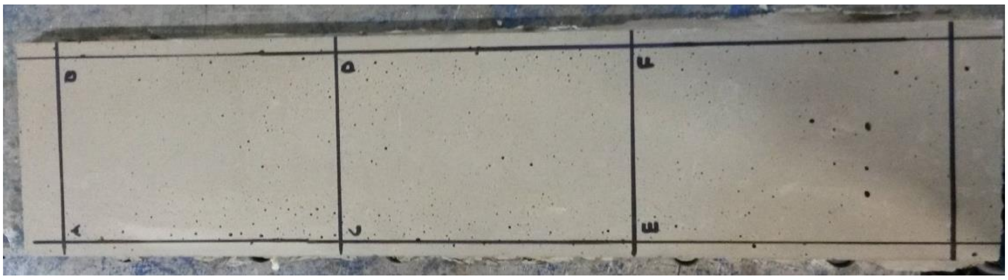

Figure 5.4: Position of the specimens in the plate before cutting.

The specimens have been tested in tension using two clamps: one clamp was connected to the actuator with a 200 KN load cell and the other fixed to the reaction frame, as shown in figure 5.5. The fixed part of the specimens on each edge was about 4 cm deep. During the tests the specimens were subjected to an imposed increasing tensile displacement at a constant rate of 0,010 mm/s. The axial force, the displacement between the two clamps and the displacement between two fixed points in the specimen at a distance of 10 cm, where measured. To measure the displacements three LVDT's sensors were used.


Figure 5.5: Actuator and load cell (a), clamping device (b) and clamped specimen during the test (c).

5.1.5 Results

In this section the tensile stress-strain responses obtained for all specimens are presented and discussed. In order to facilitate the comparison of the responses obtained for different mixtures, the tensile stresses were represented up to a value of 5 MPa and the tensile strains up to 5% to 7%.
The tensile stress and the tensile strain were calculated according to equations 1 and 2 respectively:

$$\sigma = \frac{F}{A} \text{ [1]}$$

$$\varepsilon = \frac{\delta}{l} \times 100 \text{ [2]}$$

Where: σ is the tensile stress, F is the applied force, A is the area of the cross-section of the specimen, ε is the tensile strain, δ is the displacement and l is the distance between the opposite clamped edges in the specimen.

Mixtures with Cement 42.5R:

In figure 5.6 the tensile responses obtained for the specimens of mixture M1-4R are shown. In general it is possible to distinguish the typical behaviour of strain-hardening or ECC materials: the first part of the response could be approximated to a straight line, with high stiffness and revealing elastic deformations. The formation of the first micro-crack is visible in the experimental responses for a tensile strain of approximately 0,20% and an applied tensile stress of 2,5 MPa. Afterwards, the specimens underwent large deformations due to the formation of several micro-cracks perpendicular to the longitudinal axis of the specimen. In this part of the response the material showed plastic hardening behaviour. These specimens reached a displacement between 2,5 mm and 7 mm (between 2,1% and 5,8% strain) before the localization of the macro-crack and the onset of the softening behaviour until failure. The peak stress observed was, in general, slightly higher than the tensile stress observed when the formation of the first micro-crack occurs, reaching 3,5 MPa. The failure is due to the localization of the deformations and the formation of a singular crack that leads to the rupture of the PVA fibres bridging that crack. This mixture showed a satisfactory behaviour, but the dispersion of results was excessive. Figure 5.7 shows the surface of one specimen after testing, where the presence of several micro-cracks perpendicular to the longitudinal axis of the specimen can be observed. After removing the applied load the specimen recovered partially its strain and some micro-cracks became invisible by naked eye.

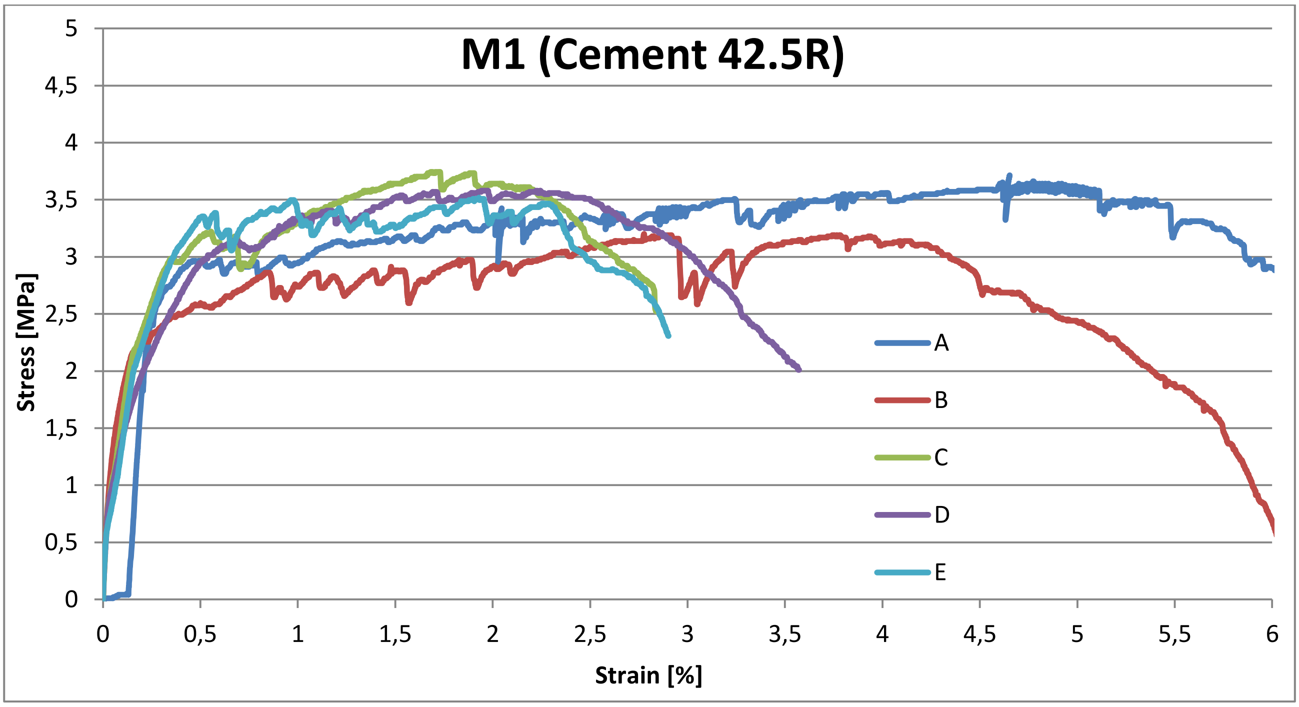

Figure 5.6: Tensile stress-strain responses obtained for mixture M1-4R.

Figure 5.7: M1A-4R specimen.

The “M2-4R” mixture showed also strain the typical hardening behaviour (figure 5.8), although the ultimate strains were in general significantly lower. In the initial stage of the test, the specimens A and C showed an apparently elastic behaviour up to a tensile strain of 0,20%. In the other specimens two segment were identifiable instead, characterized by two slightly different slopes, before the first micro-crack was observed. The behaviour after this point was characterized by the formation of micro-cracks and the slightly increase of the applied stress up to a tensile strain between 1,5% and 2,7%. In these specimens it was possible to observe a lower number of cracks, as shown in figure 5.9 were one of the tested specimens is presented.

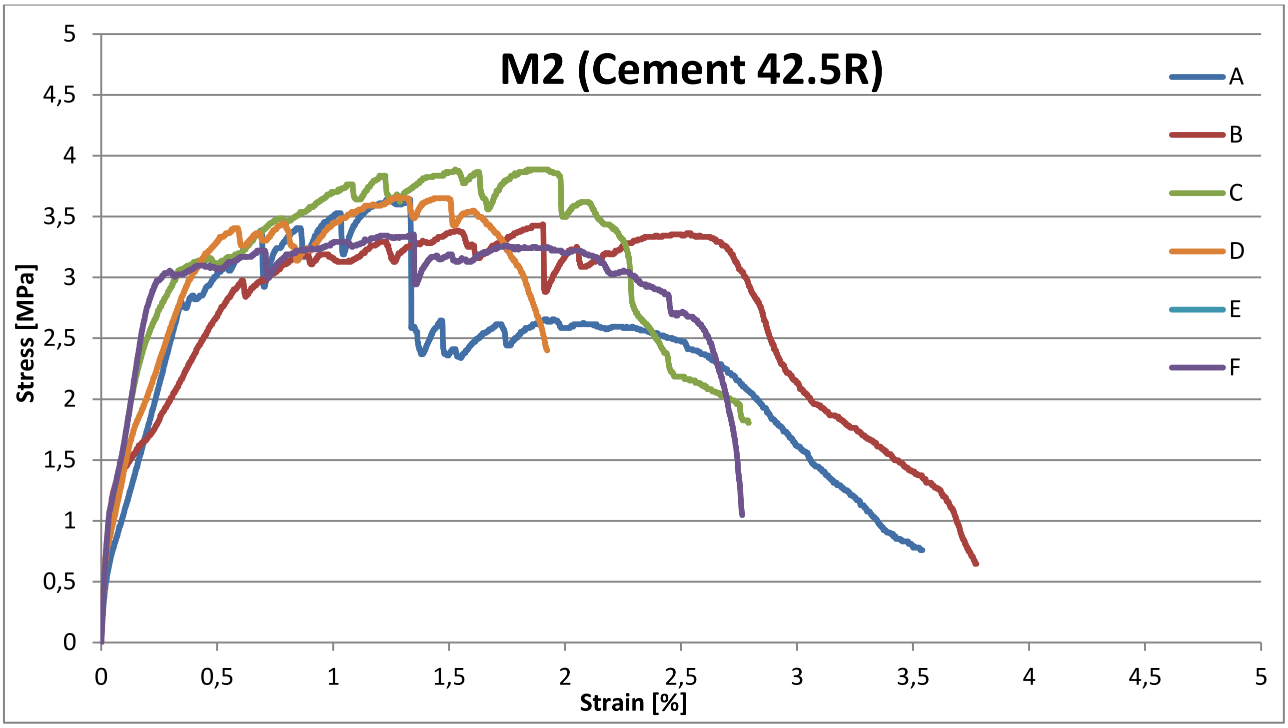

Figure 5.8: Tensile stress-strain responses obtained for mixture M2-4R.

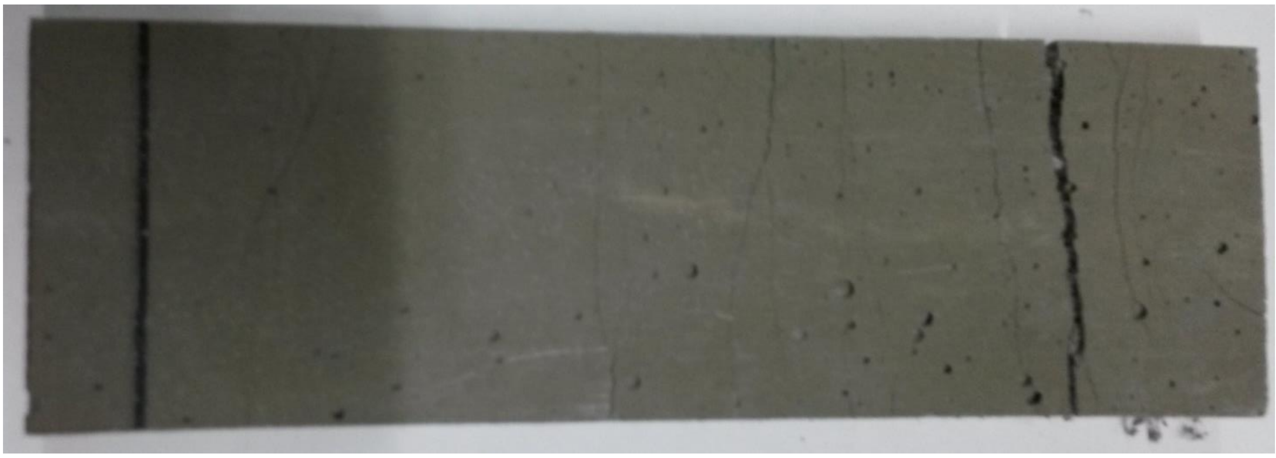

Figure 5.9: M2B-4R specimen.

The responses obtained with the third mixture are presented in figure 5.10. Apparently this mixture have resulted in the best tensile performances obtained among all tested. Before the appearance of the first micro-crack, apparently at 0,20% of tensile strain and applied stresses between 3,2 MPa and 3,8 MPa, the behaviour was approximately linear elastic with a slope of 16000 MPa. The plastic stage of the response was characterized by the formation of a large number of micro cracks, as shown in figure 5.11, where one of the tested specimens is presented. This large increment of the tensile strains occurred at a slow but constant increment of the tensile stress. The ultimate tensile stress reached values between 3,8 MPa and 4,9 MPa, at tensile strains between 2,9% to 4,3%. The range of tensile strains reached in the plastic stage of the tensile responses are 14.5 to 21.5 larger than the elastic stage, resulting in very high ductility indexes. The results obtained for this mixture are more uniform and present less scatter than the previous ones, and the main tensile characteristics such as the ultimate stress and strain are comparable or even exceed the ones found in the literature, as discussed in the previous chapters.

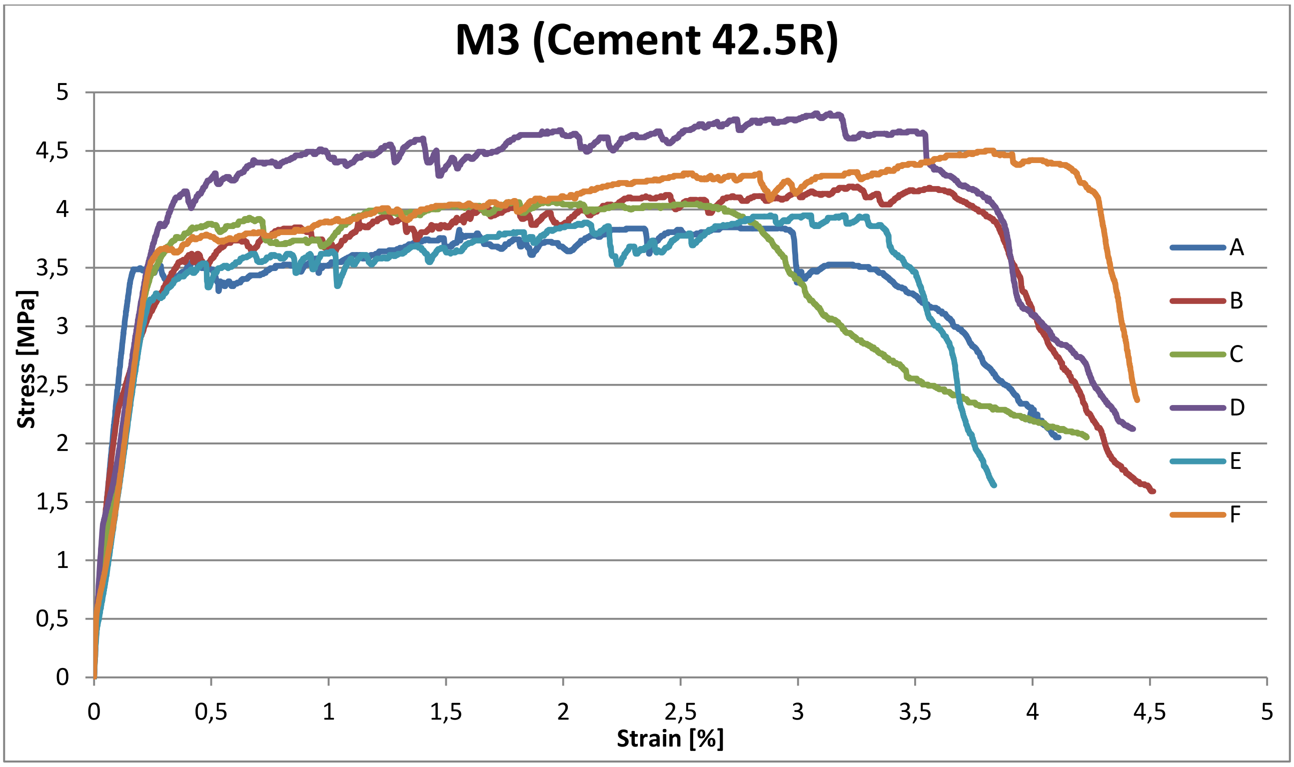

Figure 5.10: Tensile stress-strain responses obtained for mixture M3-4R.

Figure 5.11: M3A-4R specimen.

Regarding the “M4-4R” and “M5-4R” mixtures, which contained a higher ratio between cement and fly ash (1:2 for “M1-4R”, “M2-4R” and “M3-4R”, 1:1,5 for “M4-4R” and 1:1 for “M5-4R”), showed a less pronounced post cracking strain hardening behaviour. As shown in figures 5.12 and 5.13, in all specimens the first crack seems to be formed at the end of the apparently elastic stage at about 0,20% strain, however most of the specimens haven’t reached ultimate tensile strains as expressive as in the previous cases. In fact, the maximum tensile strain reached before starting the softening stage was about 1,66% strain. In figure 5.14 one of the “M4-4R” tested specimens is shown, where the number of micro-cracks that can be identified is smaller than in the previous cases.

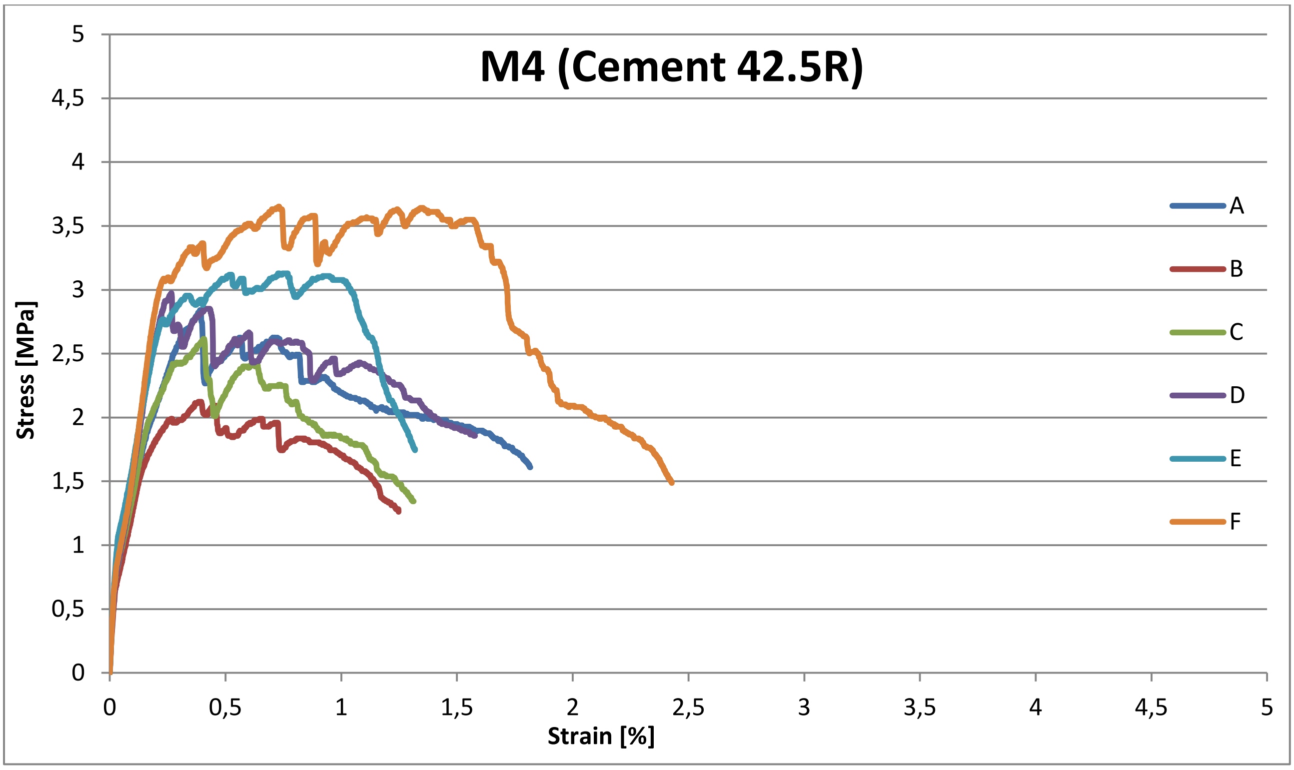

Figure 5.12: Tensile stress-strain responses obtained for mixture M4-4R.

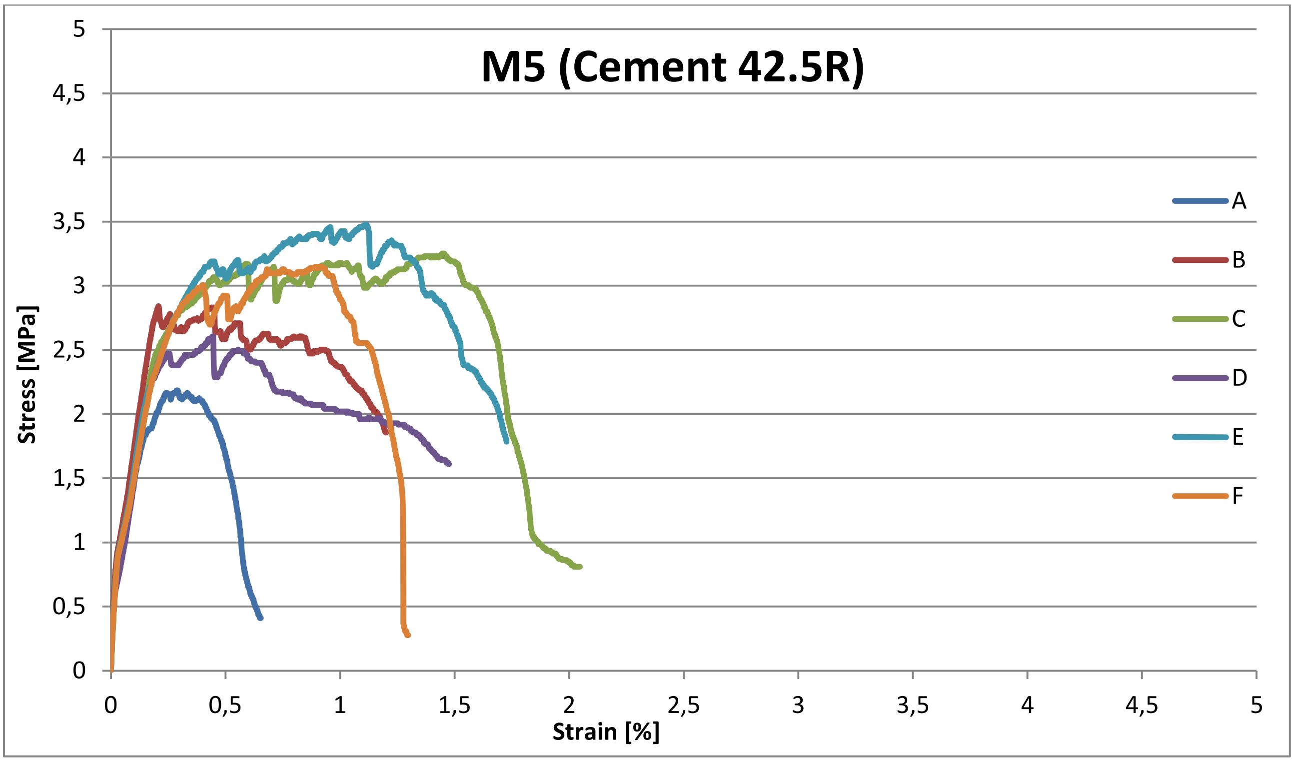

Figure 5.13: Tensile stress-strain responses obtained for mixture M5-4R.

Figure 5.14: M4F-4R specimen.

Mixtures with Cement 32.5N

In order to evaluate the influence of the type of cement used on the tensile performance of the developed composites, the mixtures previously tested were repeated by replacing the cement type 42.5R with the cement type 32.5N. In general, the results obtained were less expressive in terms of tensile performance than the ones presented previously.

As shown in figures 5.15 and 5.16, "M1-3N" and "M2-3N" mixtures showed tensile responses with less pronounced post-cracking stages if compared with the same mixtures made with cement 42.5. In particular the strain hardening behaviour was not as consistent as in the previous mixtures, and after the first micro-crack, that apparently forms at a tensile strain of 0,20%, the number of additional micro-cracks forming is less significant. Figure 5.17 shows one of the M2-3N specimens after testing, where the number of visible cracks is clearly inferior. It is possible to impute this behaviour to the wrong interaction between matrix and fibres, which can be associated both with the fresh and the hardened state of the composites.

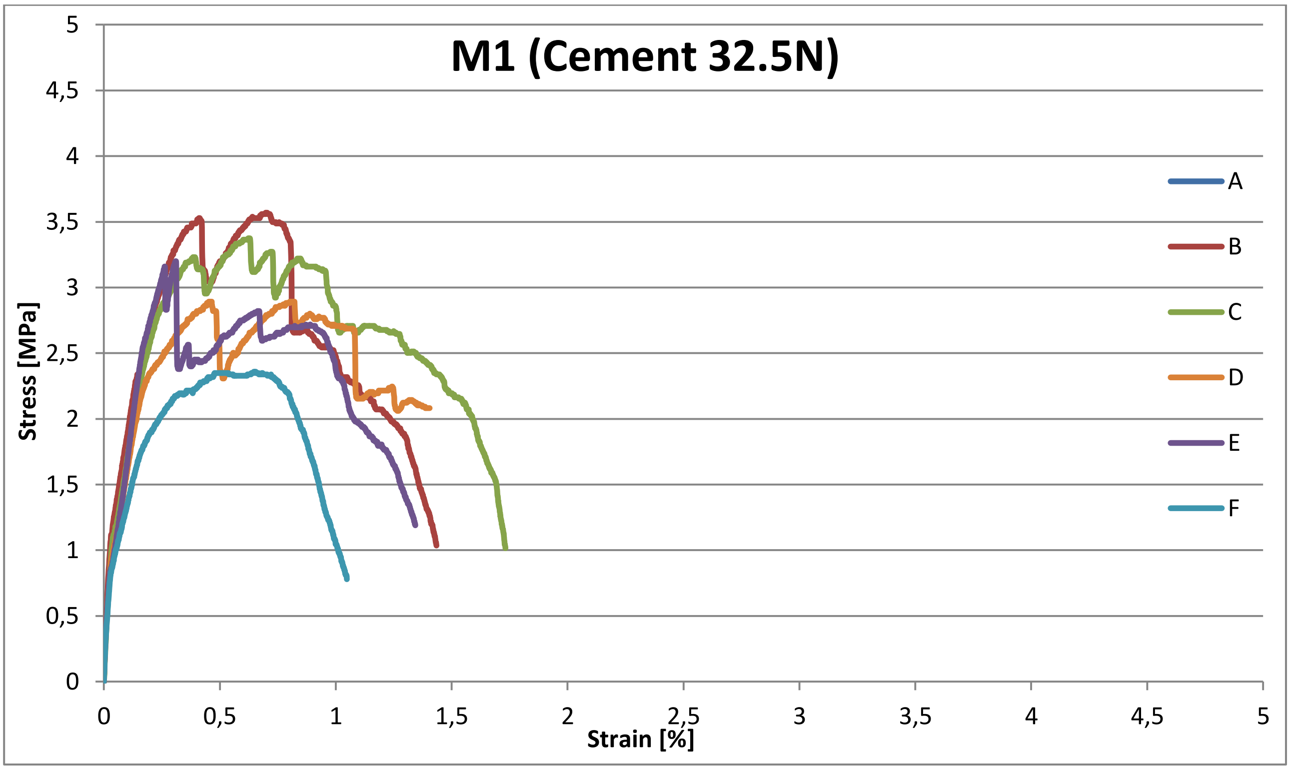

Figure 5.15: Tensile stress-strain responses obtained for mixture M1-3N.

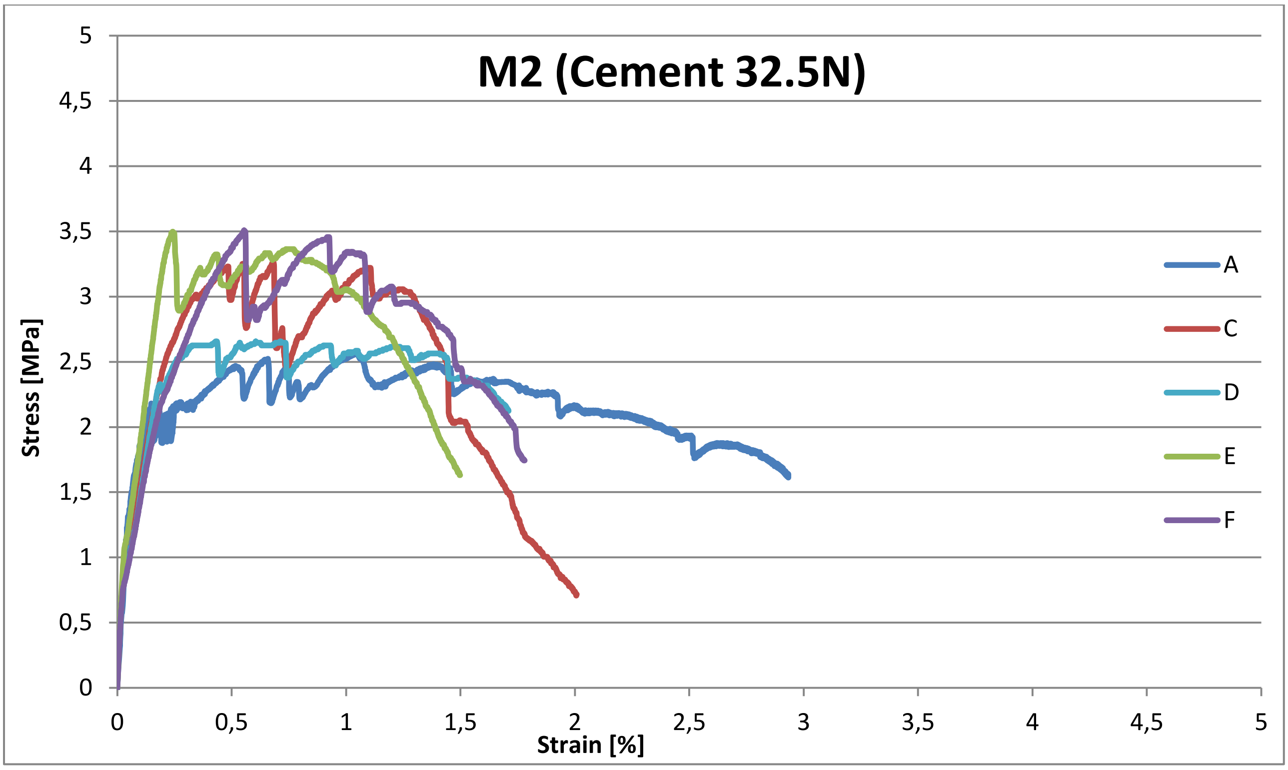

Figure 5.16: Tensile stress-strain responses obtained for mixture M2-3N.

Figure 5.17: M2A-3N specimen.

In the case of the “M3-3N” mixture the post cracking behaviour obtained was also satisfactory. In figure 5.18 it can be observed that most of the specimens reached a tensile strain of about 2,5% strain before softening, and a couple of specimens (A and B) reached an ultimate strain between 3,3% and 4,1%, with the formation of an higher number of cracks. Figure 5.19 shows one of the specimens after the testing. The first crack for all specimens seems to have occurred at a different value of the tensile stress, ranging from 1,5 MPa to 3,5 MPa. The variability of results in terms of the first cracking stress and ultimate strain and stress makes the “M3-3N” mixture less attractive than the “M3-4R” previously presented.

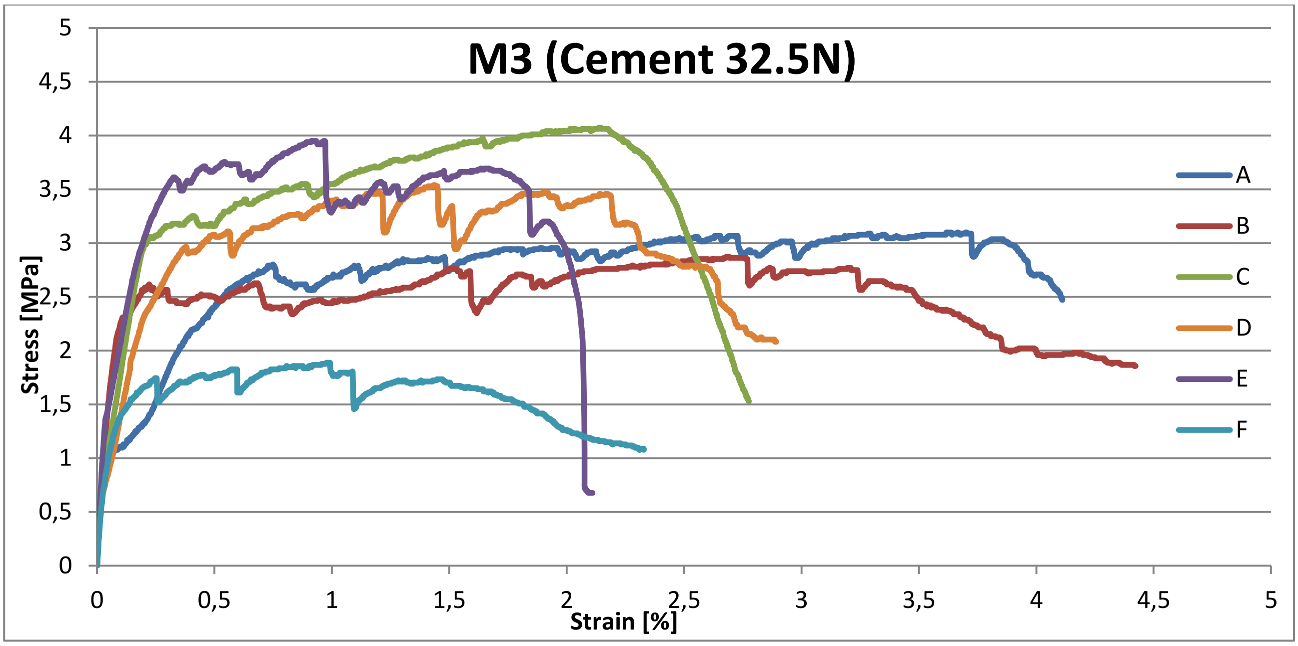

Figure 5.18: Tensile stress-strain responses obtained for mixture M3-3N.

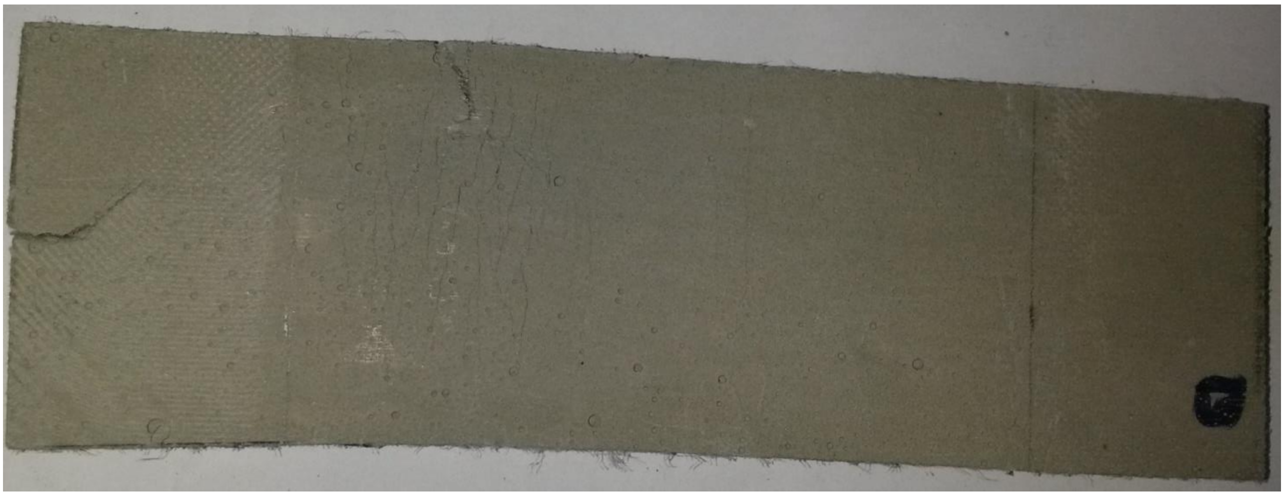

Figure 5.19: M3B-3N specimen.

Finally, the responses obtained for “M4-3N” and “M5-3N” mixtures are shown in figures 5.20 and 5.21. These mixtures contained smaller amounts of fly ash. The tensile responses obtained exhibited a smaller variability of results, but the post-cracking stages were in general less satisfactory than previously. Some of the specimens of “M4-3N” mixture showed strain-hardening behaviour but the localization started early, for tensile strains between 0,8% and 1,6 %, which is quite low when compared with the previous results. The M5-3N mixture did not perform well. After the first crack, all the specimens have presented a fragile rupture, with the formation of few micro-cracks and a premature localization of the deformation.

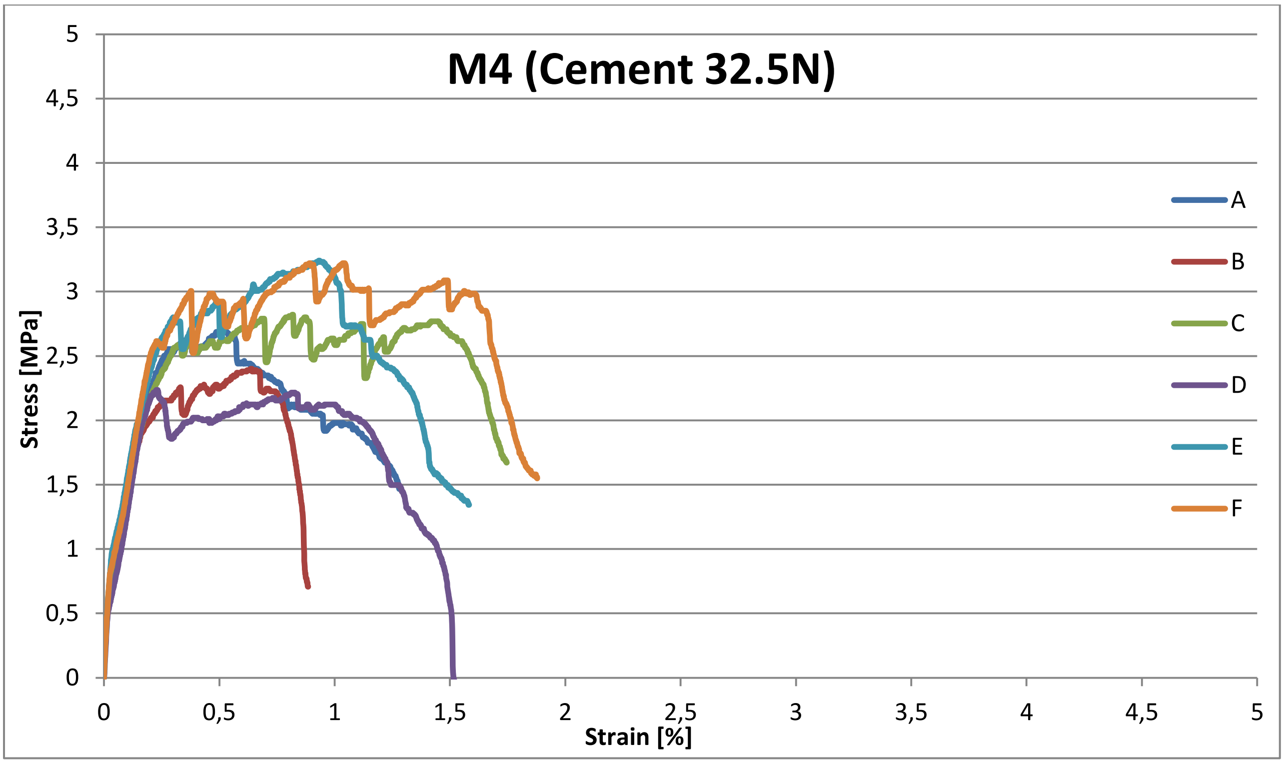

Figure 5.20: Tensile stress-strain responses obtained for mixture M4-3N.

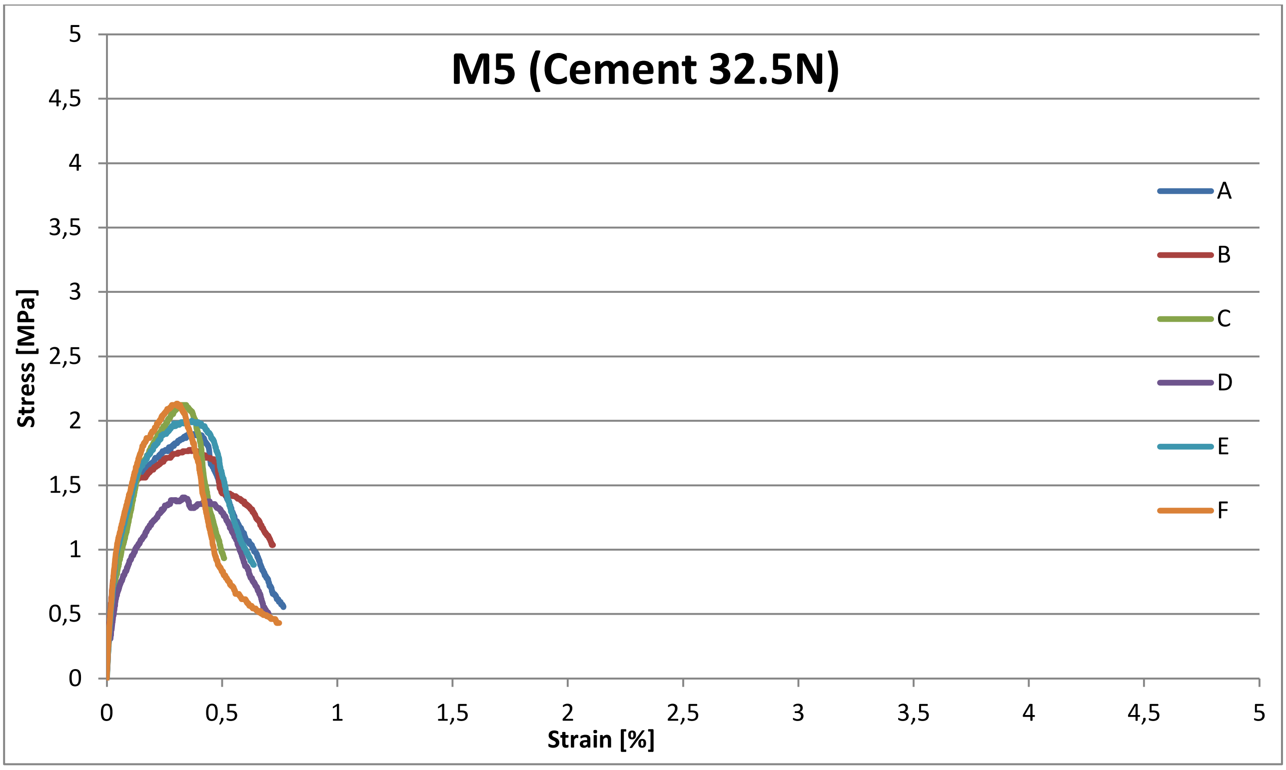

Figure 5.21: Tensile stress-strain responses obtained for mixture M5-3N.

5.1.6 Discussion of the Results

The results previously presented have shown that the composite performance in tension is sensitive to the composition components like water, fly ash or VMA. Also the utilization of different cements leads to differences in the behaviour obtained, which may be attributed mostly to their influence at the level of the interface between matrix and fibres. The characteristics of this material must be engineered carefully and at several levels, because they depend not only on the percentage of the components in the mixture, but also on the mixing procedure, curing, casting conditions among other factors. After comparing the average ultimate strain capacity (figure 5.22) of all mixtures and other characteristics visually determined, mixtures leading to lower content of air bubbles and uniform distribution of the fibres on the matrix typically lead to higher number of cracks Among all the mixtures tested, the mixture “M3-4R” was chosen to continue with the experimental programme.

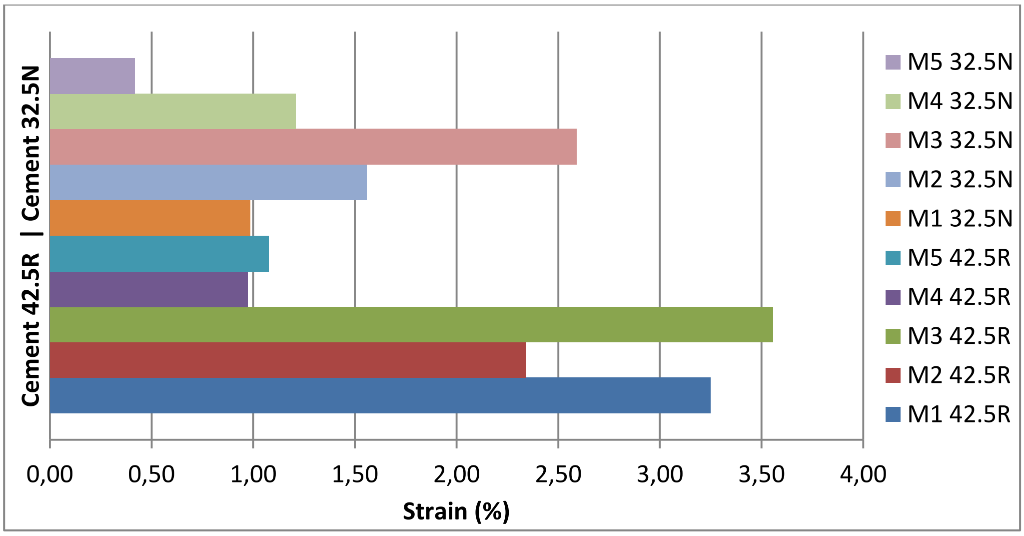

Figure 5.22: Comparison between the average ultimate strain of the mixtures.

5.2 Characterization of M3-4R Mixture

5.2.1 Fresh properties

After testing several mixtures under tensile loading, the “M3-4R”, as shown in table 5.5, was chosen to proceed with a more detailed experimental plan with the purpose of characterizing its behaviour not only in tension but also in compression and flexure. Nine specimens for compression testing, 12 specimens for flexural testing and 9 specimens for tensile testing have been prepared.

M3 -4R	
Material	Mass [g]
Cement 42.5R	876
Fly Ash	1753
Sand	307
Limestone Filler	307
Water	580
SP Sika 2002HE	33
VMA	2
Fiber PVA	52

Table 5.5: Composition of M3-4R.

After mixing every batch the fresh behaviour was measured by performing the mini-slump flow test and measuring the t20 and the final spread, as documented in the previous section. Both measurement were carried out before and after adding the fibres. The results obtained are presented in table 5.6.

Characteristics	First mixture	Second mixture	Third mixture
t20 (s)	4,15	4,23	4,5
d x d (cm)	27,5x27,5	26x26	28x27
t20 (s) (w/fiber)	4,46	6	7,69
d x d (cm) (w/fiber)	20,5x21,5	17,5x19	19x23

Table 5.6: Fresh properties of M3-4R mixtures.

5.2.2 Geometry of the Specimens

All specimens produced have matured for 28 days in a 20°C ventilated room. The moulds used to cast the specimens for compression test were cubic, the length of the edges was 5 cm. The moulds used are shown in figure 5.23.

Figure 5.23: Mould used to cast the specimens for compression testing.

The specimens for flexural tests were casted in an acrylic mould 15 mm thick, 1000 mm long and 150 mm wide, already shown in the previous section. After removing the plates from the mould, the resulting plate was cut and 1 cm from the longer edges plus 4 cm from the shorter edges were removed. The resulting plate was cut in order to obtain 6 specimens from every plate. The resulting specimens were 15 mm thick, 65 mm wide and 200 mm long.

The specimens for tensile testing were casted using Dogbone-shaped moulds, as shown in figure 5.24. The dimension of the moulds were:

- Thickness: 10 mm
- Total Length: 370 mm
- Total Width: 100 mm
- Length Central Part: 110 mm
- Width Central Part: 50 mm

Figure 5.24: Dogbone-shaped mould.

5.2.3 Compression Test

Nine cubic specimens were tested. An actuator connected to a steel cylinder was used to transfer the load to the specimen, the set-up is shown in figure 5.25. The tests were carried out at a constant displacement increment of 0,02 mm/sec.

Figure 5.25: Test setup used for the compression tests. The cross-head displacement was measured using one LVDT.

The values of the compression stress were calculated using equation 3, while the values of the compressive strain were calculated using equation 4.

$$\sigma = \frac{F}{A} \quad [3]$$

$$\varepsilon = \frac{\delta}{h} \times 100 \quad [4]$$

Where: F is the applied force, σ is the stress, A is the area of the section of the specimen, ε is the strain, δ is the displacement measured by the LVDT and h is high of the specimen.

Since it was not possible to measure the displacement between the top and the bottom surface of the compression specimens during testing, the compressive strain obtained with the displacement of the cross-head overestimates the real compressive strain.

Observing the results obtained for the *compression tests* on table 5.7, it is possible to verify that this mixture reached an ultimate stress between 32 MPa and 40 MPa, with an average value of 37 MPa. These values are typical for this kind of material, as reported in the previous chapters. Even if the strain values are high, due to the sum of the deformation of the frame, it is still possible to confirm that this material is also very deformable in compression.

Specimen	Max stress [Mpa]
1	36,46
2	38,91
3	38,53
4	37,56
5	40,18
6	32,39
7	35,84
8	35,72
9	39,85
Average	37,27

Table 5.7: Maximum compression stress obtained for the 9 specimens

Figure 5.26 shows three specimens after testing. The specimens exhibited multiple cracks even before reaching the compressive strength. One of the main features of this material is that even after the failure, which is typically obtained and high strains, the behaviour is not explosive and does not lead to the separation of the specimen in smaller parts .

Figure 5.26: Three cubic specimens after compression test.

5.2.4 Bending Test

Six specimens were tested in flexion. The specimens were positioned over two steel cylindrical supports at a distance of 16 cm, as shown in figure 5.27. The force was applied at the mid-section of the specimens through one steel cylinder connected to the actuator. Increasing displacement at a constant rate of 0,02 mm/sec was imposed by the actuator. Flexural strength was calculated with equations n. 5 and n. 6:

$$\sigma = \frac{M}{W} \ [5]$$

$$W = \frac{b \times h^2}{6} \ [6]$$

Where: σ is the flexural strength; M is the applied moment; b is the width of the specimen and h is the thickness of the specimen.

The results of the *flexural tests* showed an increase of the flexural stress due to the formation of micro-cracks at the lower surface of the specimen. In figures 5.28 and 5.29 it is possible to observe the formation of the cracks which occur much before the failure of the specimens. The flexural responses obtained, which are shown in figure n. 5.30, present a deflection-hardening behaviour. This type of behaviour was expected, considering that this material exhibited tensile hardening under direct tension. The flexural strengths obtained varied between 11 MPa to 14 MPa, which are typical values for this kind of strain-hardening cementitious composite.

Figure 5.27: ECC specimen during flexural testing.

Figure 5.28: Formation of micro-cracks on the bottom of the specimen.

Figure 5.29: Formation of a large crack and failure of the specimen.

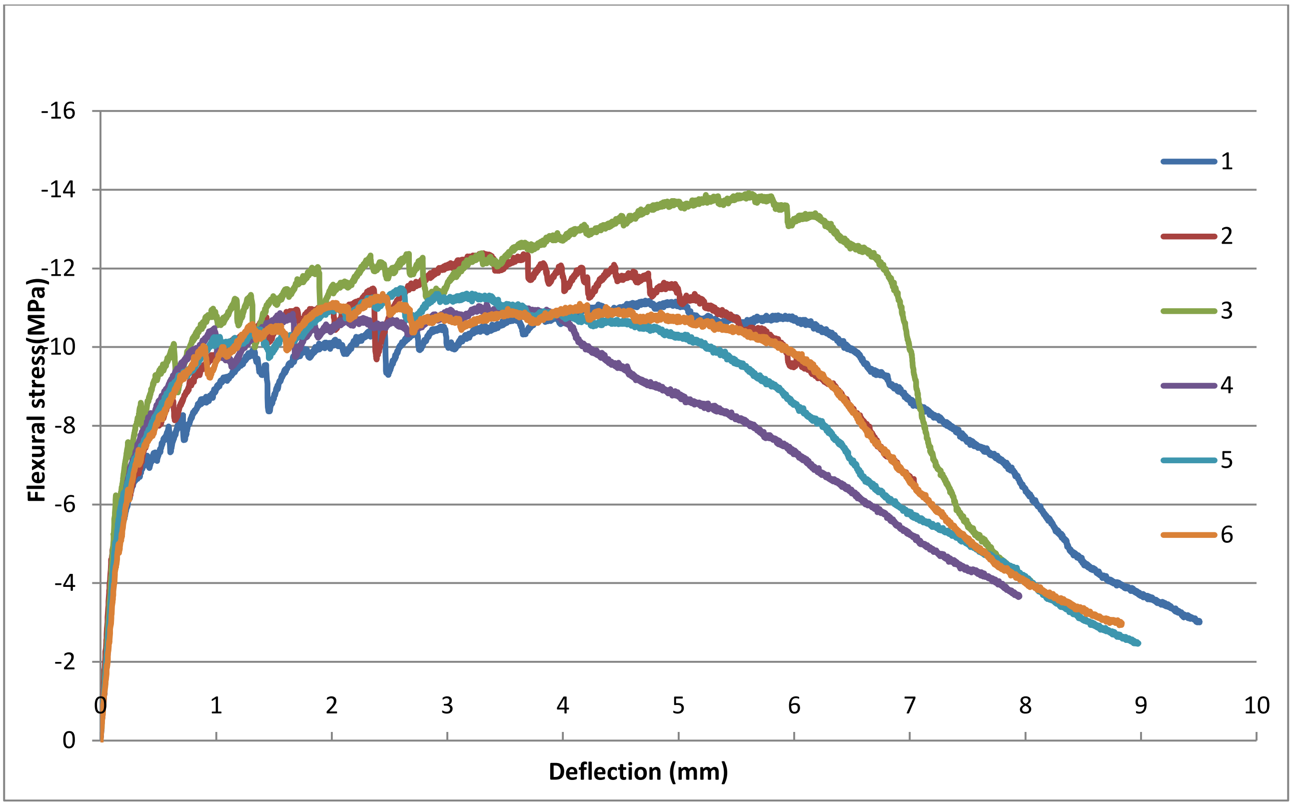

Figure 5.30: Flexural stress-deflection responses obtained.

5.2.5 Tensile Test

Ten specimens have been tested in direct tension. The specimens were clamped in both opposite edges, where one clamp was connected to an actuator and the other fixed to the reaction frame, as shown in figures 5.32 and 5.33. The specimens were rectified before testing, in order to improve the adherence with the surface of the grips and maximise the friction to avoid the slip of the specimen during the test. In order to increase even further the friction between the clamps and the specimens, two layers of thick sandpaper were also used. Three LVDTs were used to measure the displacement between the two clamps and displacement between two fixed points in the specimen at a distance of 10,5 cm, as shown in figure 5.31. The axial force applied was measured using a load cell.

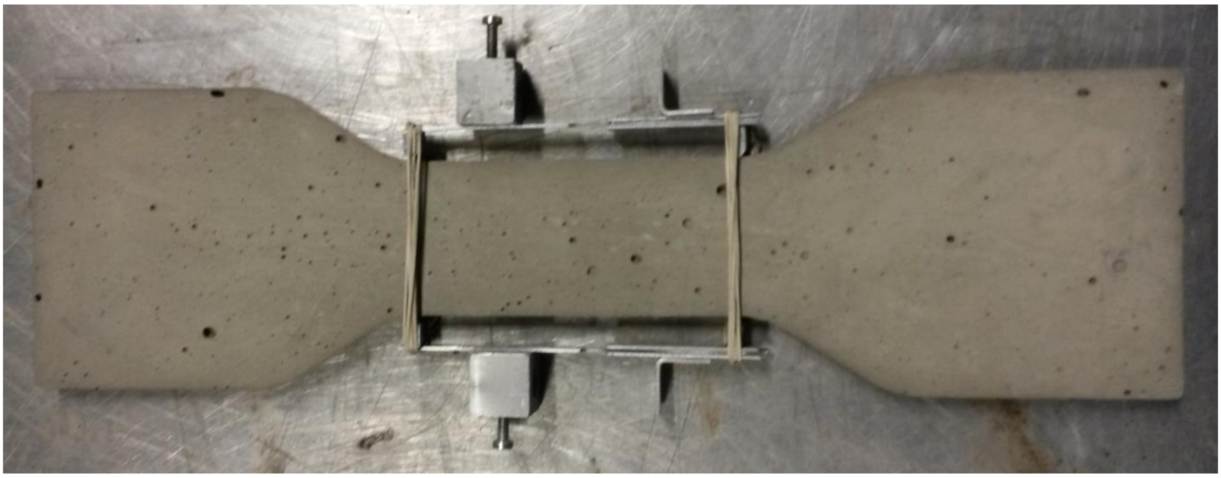

Figure 5.31: Dogbone-shaped specimen before testing and the 2 devices used to place the 2 LVDT.

The subsequent testing procedures have been carried out:

- Monotonic tensile testing under displacement control.

- Cyclic testing (1%): initial loading of the specimen in tension until 1% strain was reached, under displacement control, and subsequent unloading until 0% strain was reached also under displacement control. the same procedure was repeated 4 times, after which the specimen was subjected to an imposed tensile deformation under displacement control until failure.
- Cyclic testing (2%): the same procedure as before, but now the loading cycles are stopped at a tensile strain of 2%.
- Cyclic (+1%)DCL-FCU: the specimen was loaded in tension until 1% of strain was reached, under displacement control, then unloading occurred by reducing the tensile stress applied 2,5 MPa under force control. Subsequently, the specimen was subjected to a second loading stage until an additional tensile strain of 1% was reached, under displacement control. Subsequently, unloading occurred by reducing the tensile stress applied 2,5 MPa under force control . The same cyclic procedure was repeated four times, after which the specimen was subjected to a tensile displacement increment under displacement control until failure was reached.
- Cyclic (+1%) DC: initial loading of the specimen in tension until 1% strain was reached, under displacement control, and subsequent unloading until 0% strain was reached also under displacement control. The same sequence was repeated but reaching the tensile strain of 2%, 3% and 4%, and finally the specimen was loaded in tension until failure, under displacement control.

All tests which were carried out under displacement control subjected the specimens to displacement increments at a constant rate of ±0,015 mm/s. All tests which were carried out under force control subjected the specimens to force increments at a constant velocity of 0,02 KN/s. Tensile stresses and strains have been computed using the equations 7 and 8:

$$\sigma = \frac{F}{A} \quad [7]$$

$$\varepsilon = \frac{\delta}{h} \times 100 \quad [8]$$

Where: F is the applied force, σ is the tensile stress, A is the area of the cross-section of the specimen, ε is the tensile strain, δ is the displacement measured by the LVDT and h distance between two fixed point where the LVTD's were positioned.

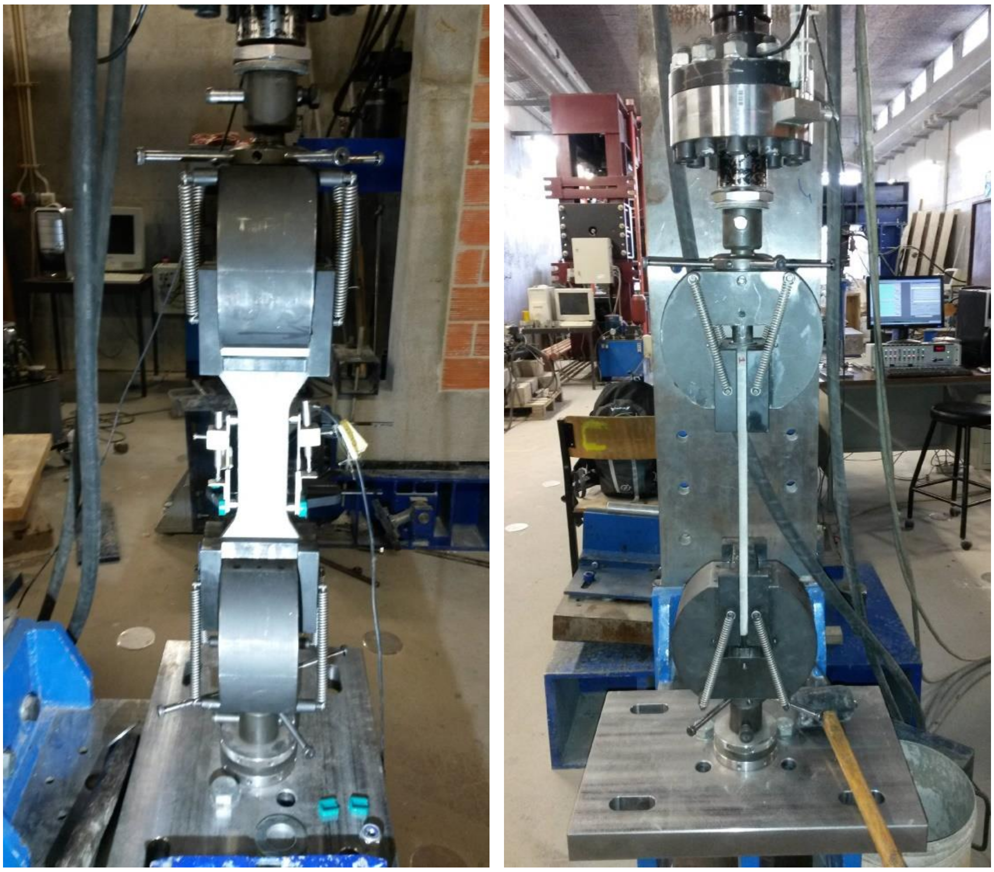

Figure 5.32: Test setup used for tensile testing.

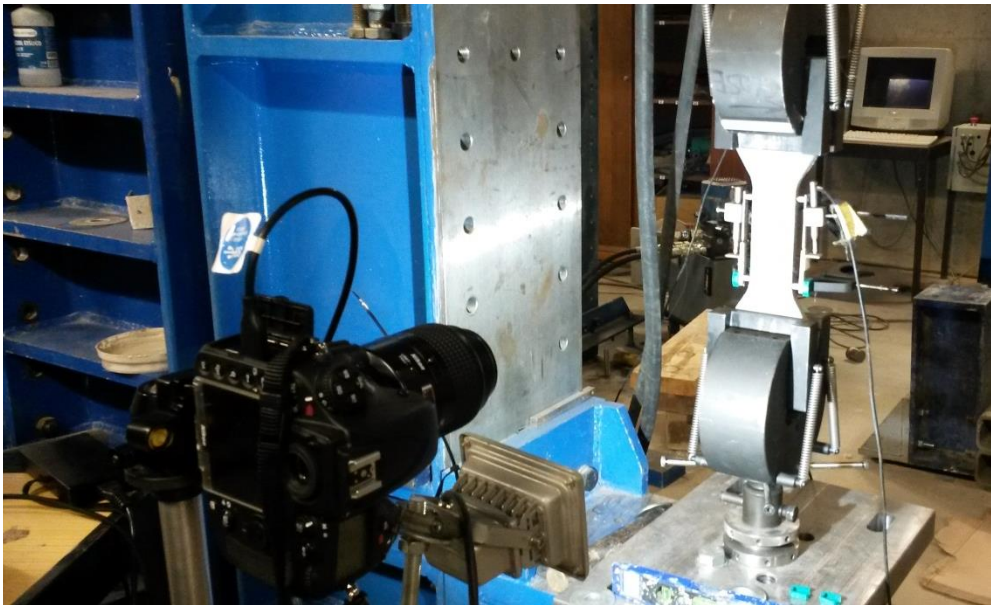

Figure 5.33: Setup for capturing high resolution images of the tensile specimens' surface.

The results obtained for the monotonic tensile tests are presented in figure 5.34. As shown, the responses presented high stiffness before the formation of the first crack, apparently at about 0,10-0,15% of tensile strain. After the formation of the first crack, the specimens exhibited pronounced plastic deformation due to the formation of several micro-cracks at increasing tensile stresses, reaching values higher than 3,5 MPa (in one case it reached 4,5 MPa). In figures 5.38 and 5.39 it is possible to observe the crack pattern at the surface of the specimen 5 during testing. The specimens reached ultimate tensile strains between 4% and 5,25%. The response obtained for specimen 5 presents some "noise" in the results between the tensile strains of 0,5% and 2%. The reason of this electrical noise could be the use of other heavy electrical equipments in the laboratory at the same time.

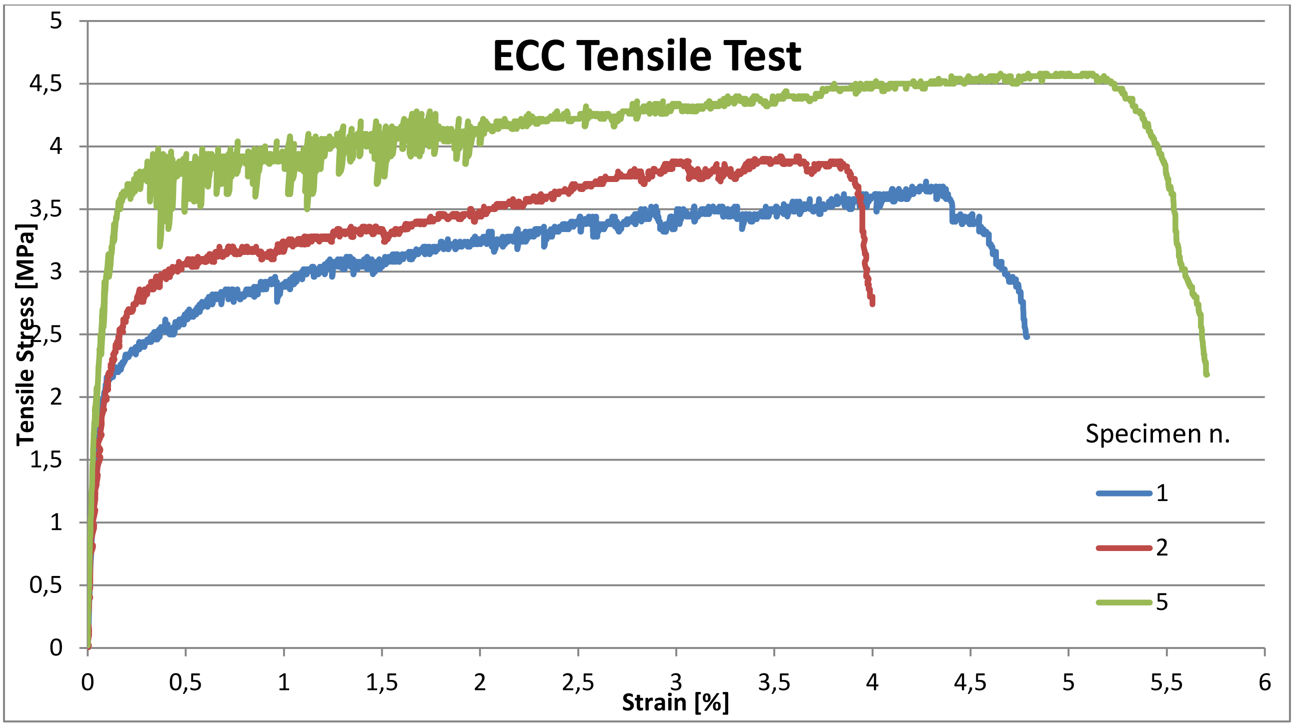

Figure 5.34: Monotonic tensile stress-strain responses.

The specimen tested under *cyclic tension* showed approximately the same features as the specimens tested under monotonic tension: the ultimate tensile stress reached 4 MPa, and the ultimate tensile strain reached 4,5%. This means that if the material undergoes cycles of pure tension, its strain-hardening properties remain unchanged. In fact, during the unloading, the micro-cracks didn’t have the possibility to close completely, keeping unchanged the characteristics of the matrix surface. One characteristic that is possible to observe in the stress-strain diagram shown in figure 5.35 is that the slope of the unloading cycle at 1% strain is higher than the slopes at 2%, 3% and 4%, which means that the composite loses stiffness with the increasing of the strain, as a result of the formation of more cracks. The slope of the loading stages also decreases with the increase of the strain. In every loading cycle, the specimen returns to the typical tensile strain hardening envelope observed in the monotonic tests when the maximum strain previously reached is attained. Unfortunately the curve presents some artefact peaks: due to the control procedure, when changing from displacement control during loading, to force control during unloading, there is a pressure peak that produced these tensile loading peaks. However the expected behaviour can be easily inferred, by extrapolating the behaviour observed immediately before the control alteration was produced, for each cycle, as shown in figure 5.35.

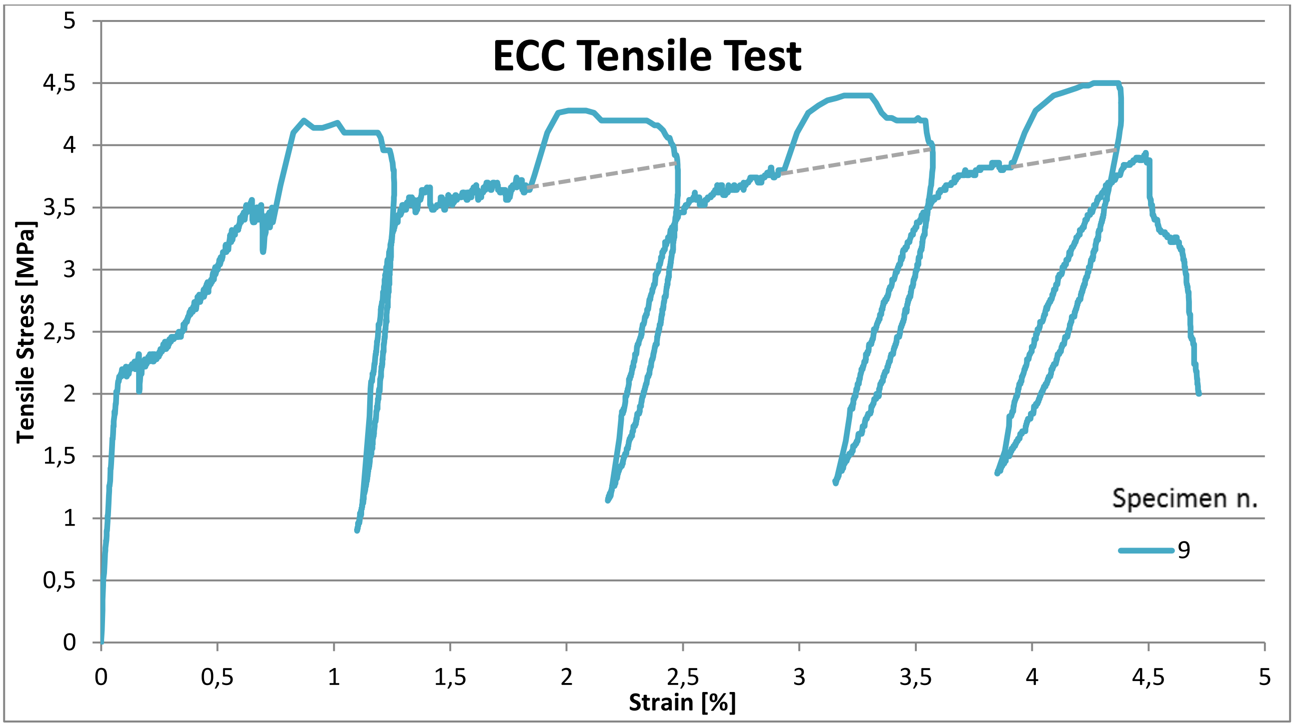

Figure 5.35: Cyclic tensile stress-strain response for displacement controlled loading and force controlled unloading test.

The *cyclic* tests, which were carried out entirely under displacement control, included four cycles of loading and unloading. The duration of the tests varied between 15 and 25 minutes, which can be considered as representative of the duration of an earthquake event.
The specimen 4 underwent four loading cycles up to a tensile strain of 1%, and then it was loaded in tension until failure under displacement control. During the loading cycles the specimen reached stress values of approximately 4 MPa, as observed in the previous specimens. During the unloading ramps the specimen underwent compression loading, in order to close the micro-cracks and return to the initial length. Maximum compression stresses of about 4 MPa have been reached. During the last loading cycle the specimen showed a reduction of plastic deformation and failed at 2,8% strain. This ultimate tensile strain is 30%-40% lower than the ultimate strain of the previous specimens tested under monotonic tension and cyclic tension. The reason for this loss of ductility may be attributed to the effect of the compression stresses on damaging the matrix and most likely the PVA fibres partially pulled out from the matrix. Is important to consider this behaviour because during a seismic event the structural elements could undergo cycles of tension and compression, although probably not as severe as the ones imposed in this experimental programme.
The specimen number 10, that underwent four loading cycles from 0% to 2% tensile strain and then taken to failure in tension showed the same mechanical features, although with a more pronounced decrease of the ultimate tensile strain (2,1%), probably because it underwent higher compression stresses (almost 6 MPa). This reduction of ductility may again be caused by the compression stresses during the unloading cycles.
The last specimen (number 8) was subjected to 4 loading cycles at different imposed tensile strains. The tensile stress-strain response reached the ultimate strain of 3,9% with a reduction of the carried tensile stress in the last cycle from almost 4 MPa to 2,5 MPa. During the unloading cycles the specimen underwent compression stresses due to the need to close the cracks. The maximum compressive stress registered in each cycle increased from 4 MPa in the first cycle, to 7,5 MPa in the last cycle. Nevertheless, the specimen number 8 revealed the formation of several cracks, as shown in figures 5.40 and 5.41. In figures 5.36 and 5.37 the tensile stress-strain responses of specimens number 4, 8 and 10 are reported.

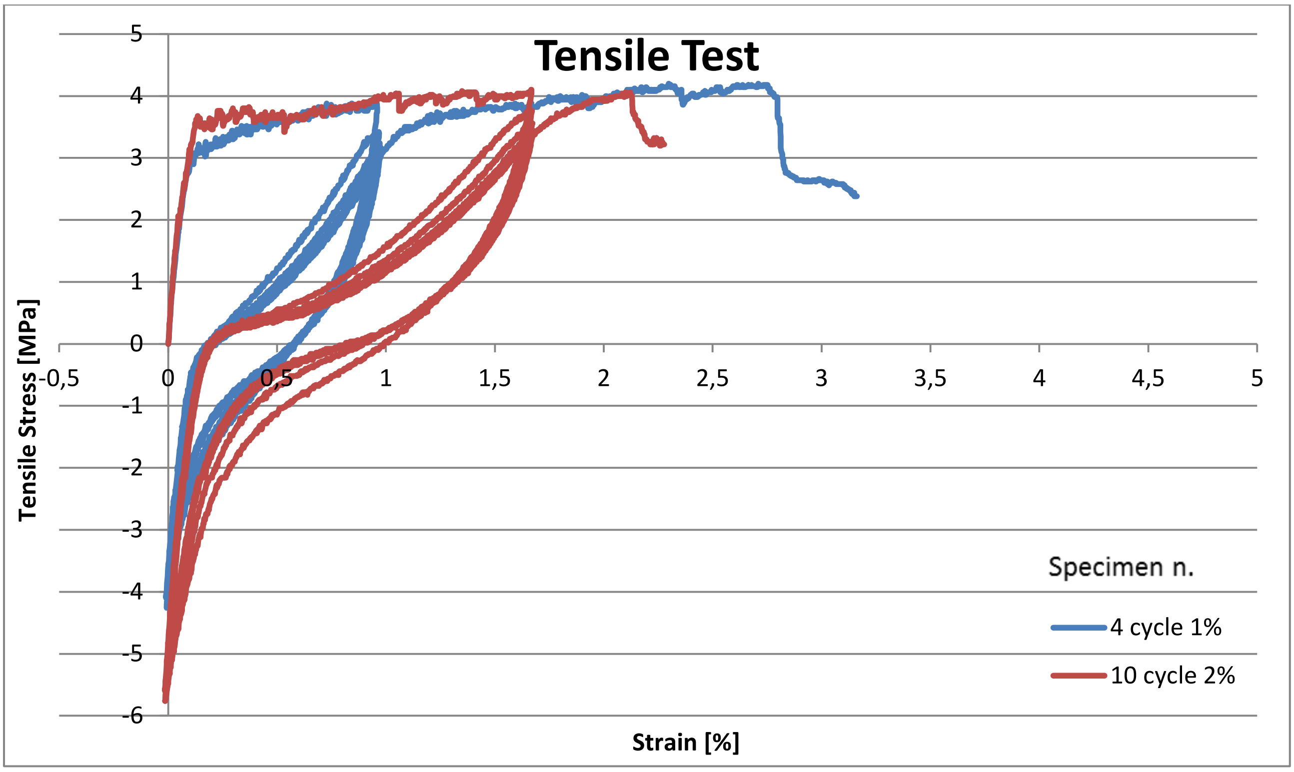

Figure 5.36: Cyclic stress-strain response for 1% and 2% strain cyclic tests under displacement control.

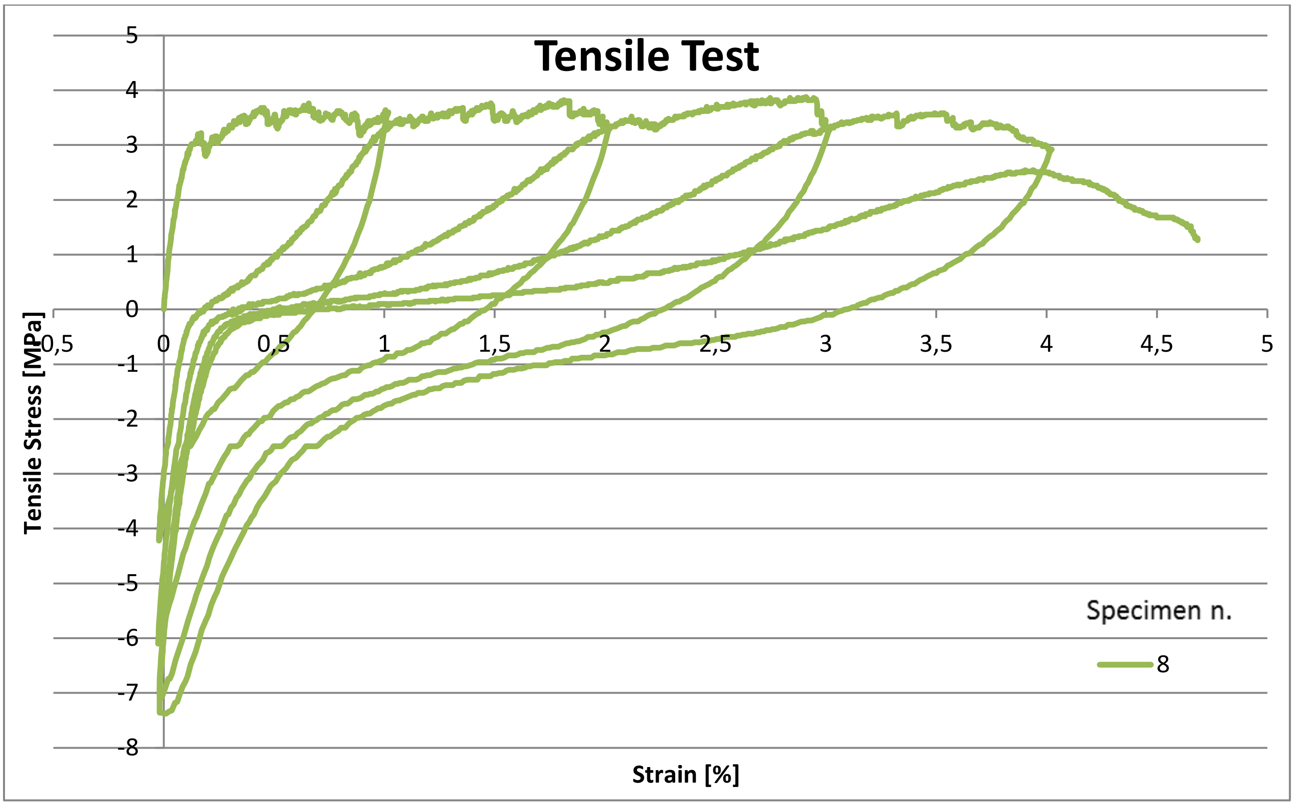

Figure 5.37: Cyclic stress-strain response for 1%, 2%, 3% and 4% strain cycles under displacement control.

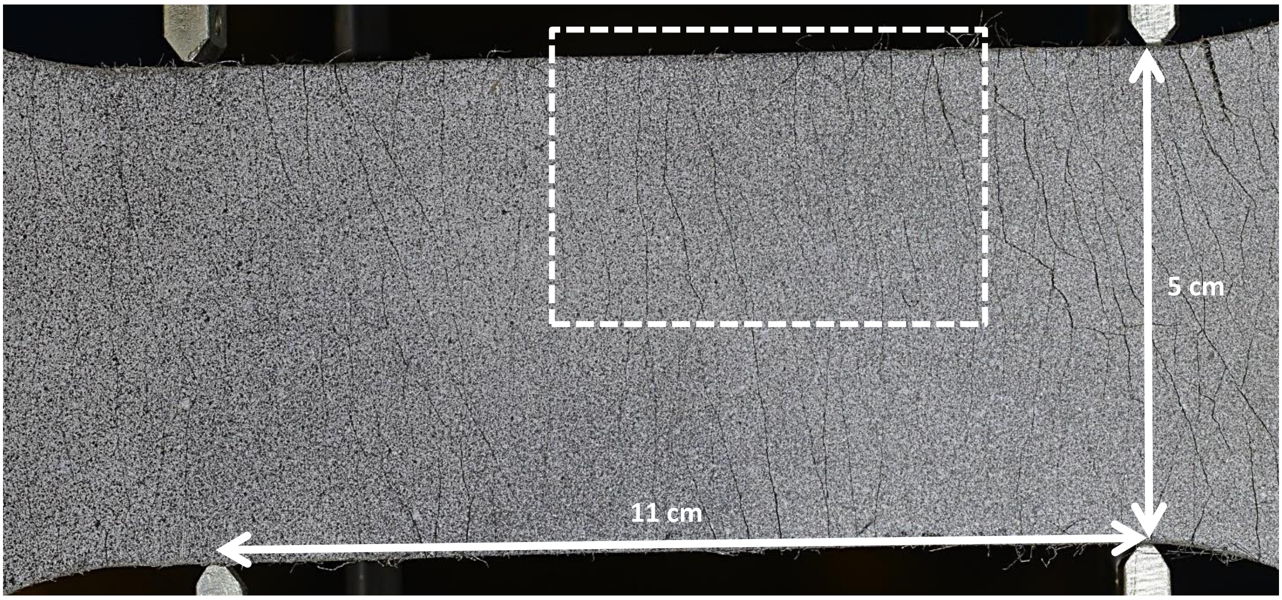

Figure 5.38: ECC dogbone-shaped specimen during monotonic tensile test, showing several micro-cracks formed at the surface.

Figure 5.39: Zoom at the surface of the specimen shown in figure 118.

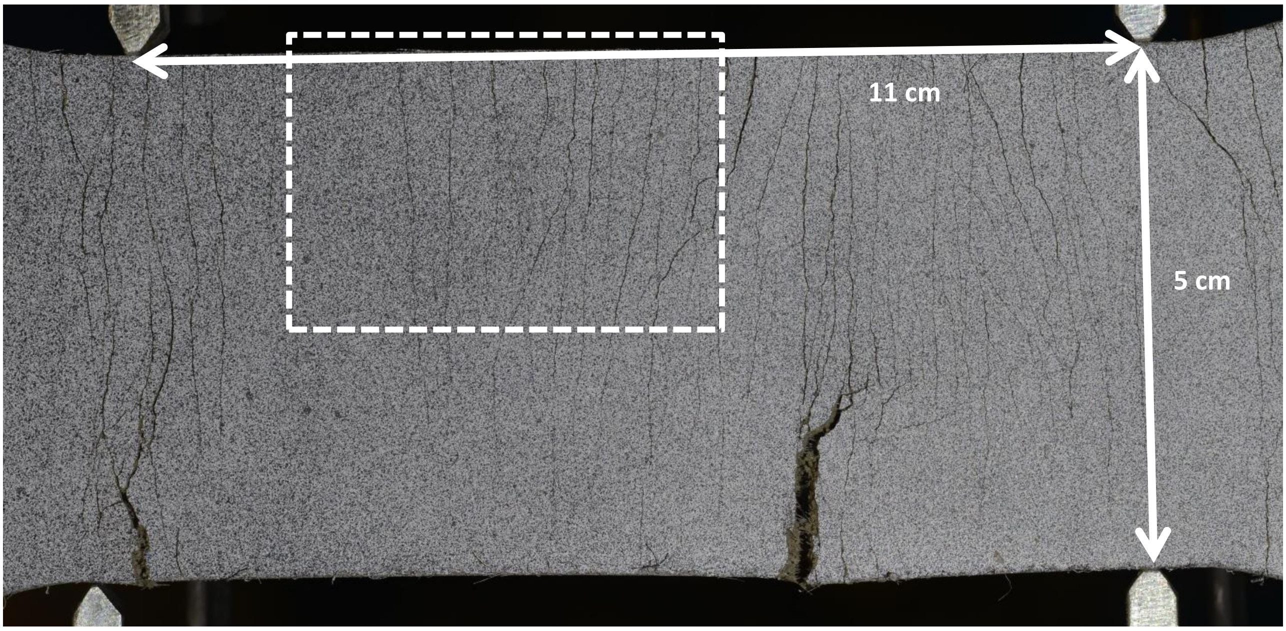

Figure 5.40: ECC dogbone-shaped specimen during cyclic test, showing several micro-cracks formed at the surface.

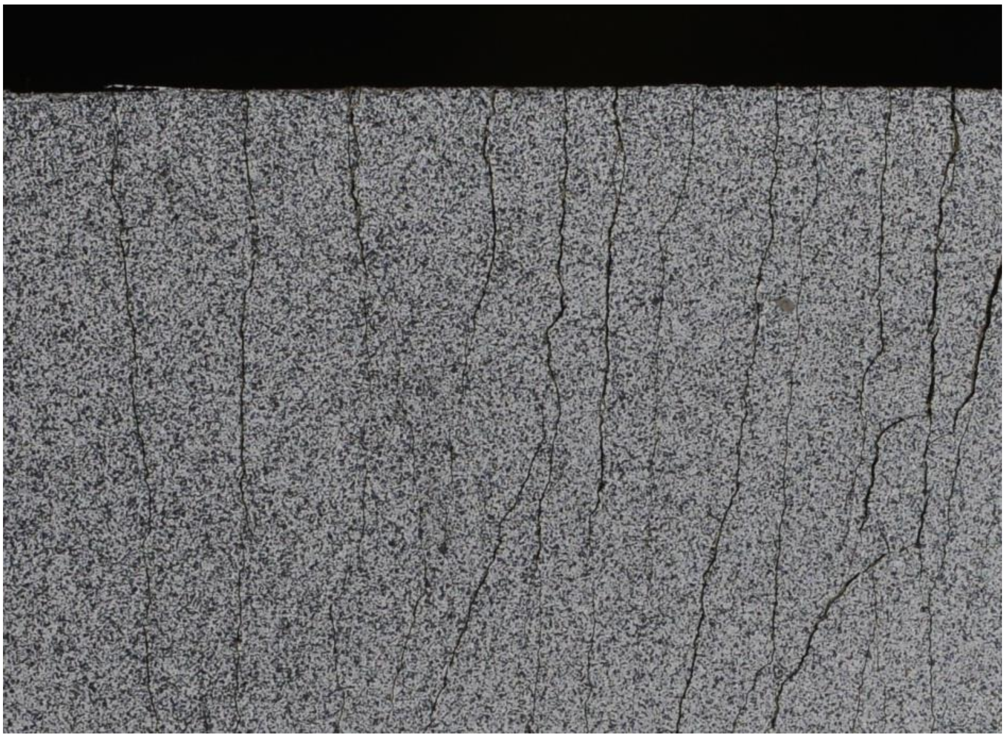

Figure 5.41: Zoom at the surface of the specimen shown in figure 120.

5.3 Characterization of Nitinol

5.3.1 Test Set-up and Samples

Among all the available materials showing Super-Elastic and Shape-Memory effect, Nitinol was selected because of its characteristic temperature range. It is especially interesting for civil engineering applications where both the Super-Elastic and the Shape-Memory effects can be exploited. Two different types of Nitinol were obtained and characterized in tension. The first was a 0,02795 inches diameter wire (0,71 mm) produced by "Furukawa Electric Group". The second was a 1,5 mm diameter wire, produced by "Euroflex" company.

The tests have been carried out following the international "ASTM designation: F2516-07" [1], which suggests that the Nitinol wire should be pulled up to 6% tensile strain, then unloaded until a stress lower than 7 MPa is reached and then finally pulled up to failure. The recommended velocity for the test depends on the wire thickness, as illustrated in table 5.8.

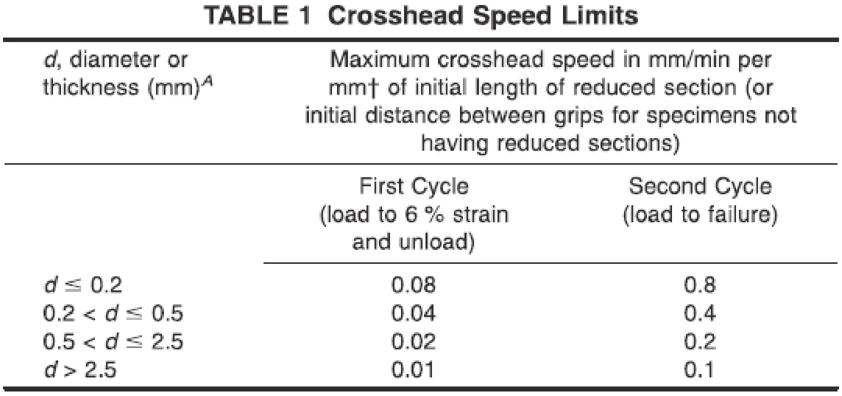

TABLE 1 Crosshead Speed Limits

d, diameter or thickness (mm)^A	Maximum crosshead speed in mm/min per mm† of initial length of reduced section (or initial distance between grips for specimens not having reduced sections)	
	First Cycle (load to 6 % strain and unload)	Second Cycle (load to failure)
$d \leq 0.2$	0.08	0.8
$0.2 < d \leq 0.5$	0.04	0.4
$0.5 < d \leq 2.5$	0.02	0.2
$d > 2.5$	0.01	0.1

Table 5.8: Testing parameters depending on the wire diameter according to ASTM F2516-07[1].

The Nitinol samples of two different types were subjected to the following experimental procedure:

- Wire with 0,71 mm of diameter, 150 mm long: the specimens were subjected to a first cycle of imposed tensile elongation at a constant rate of 0,05 mm/s and a second cycle at a constant rate of 0,5 mm/s.
- Wire with 1.5 mm of diameter, 150 mm long: the specimens were subjected to a first cycle of imposed tensile elongation at a constant rate of 0,033 mm/s and a second cycle at a constant rate of 0,333 mm/s.

The wire specimens were tested in tension using two clamps to fix both edges of the specimen. One of the edges was connected to a load cell and the actuator, and the other was fixed to the reaction frame. The embedded length into the grips of the specimens edges was 50 mm. Different types of sandpaper, epoxy glue and Araldite have been tried to increase the friction between the grips and the wire during tensile testing. The thinnest sandpaper and the epoxy glue resulted in the best conditions for tensile testing without the occurrence of slippage at the grips. Sandpaper was finally chosen to continue with all the tests. Sample number 4 from the first type of wires (0,71 mm diameter) was tested with a different procedure: it was pulled until 1% strain, unloaded, pulled until 2% strain, unloaded, pulled until 3% strain, unloaded, pulled until 4% strain, unloaded and finally pulled up to failure. All the loading and unloading sequences were carried out under displacement control with a constant displacement rate of 0,05 mm/s. Samples number 2 and number 3, from the second type of wire (1,5 mm diameter), were tested following a different procedure that included only a displacement controlled loading sequence at a constant displacement rate of 0,033 mm/s until failure.

5.3.2 Results

The tensile stress-strain responses obtained for the two wires are discussed in this chapter. The stress and the strain were calculated based on the equations number 9 and 10:

$$\sigma = \frac{F}{A} \quad [9]$$

$$\varepsilon = \frac{\delta}{h} \times 100 \quad [10]$$

Where: F is the applied force, σ is the stress, A is the area of the cross-section of the sample, ε is the strain, δ is the displacement measured by the LVDT and h is the length of the specimen (excluding the length embedded in the grips) .

According to ASTM F2526-07, the upper plateau strength (UPS), the lower plateau stress (LPS), the residual elongation (El_r), the uniform elongation (El_u) and the ultimate strength (US) of each samples have been characterized. All of these properties are illustrated in figure 5.42.

- Upper plateau strength (UPS): the stress at 3% strain during the loading sequence.
- Lower plateau stress (LPS): the stress at 2,5% strain during the unloading sequence after the loading up to 6% strain is finalized.
- Residual elongation (El_r): the difference between the strain at a stress of 7 MPa during unloading and the strain at a stress of 7 MPa during loading.
- Uniform elongation (El_u): the elongation determined at the maximum force sustained by the specimen just prior to necking, or fracture, or both.
- Ultimate stress (US): the maximum stress before failure.

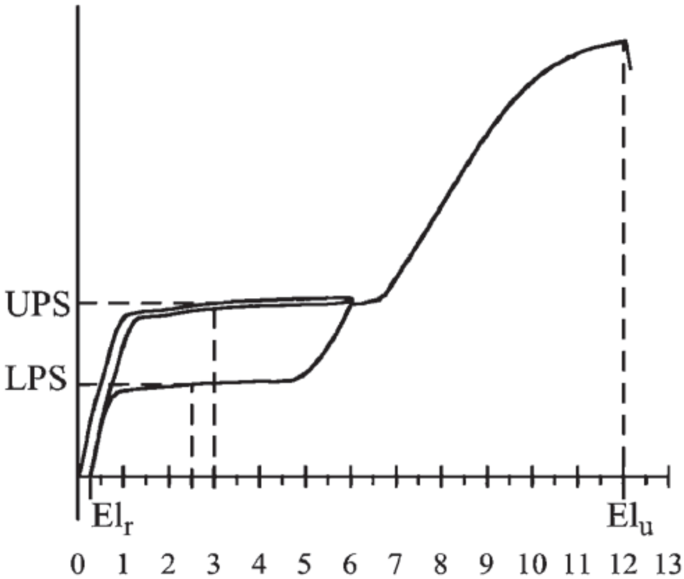

Figure 5.42: Typical stress-strain response and main characteristics of super-elastic Nitinol [1].

The results obtained for the *0,71 mm* diameter wire are shown in table n. 5.9:

Sample	UPS (Mpa)	LPS (Mpa)	US (Mpa)	Elr (%)	Elu (%)
1	417	9	1315	0,1	13
2	384	13	1367	0,43	13,6
3	414	29	1369	0,46	13,5
4	432	35	1344	1,17	13,1

Average	412	21,50	1348,8	0,54	13,3

Table 5.9: Properties of the 0.71 mm Nitinol wires, according to ASTM F2526-07.

Observing the tensile stress-strain responses presented in figures 5.43 to 5.46, it is possible to conclude that the first type of wire shows a tensile behaviour which may be considered as super-elastic. After subjecting the samples to 6% of tensile strain and subsequent unloading, it is possible to verify that the wires recovered most of the deformation and a residual tensile strain between 0,43% and 1,17% remained. However, the definition of the lower plateau stress is not clear, because all the specimens exhibited low stresses at 3% strain during unloading. This is probably caused by high Austenitic phase transition temperatures, so that at the temperature conditions during the tests, the ratio between Austenitic and Martensitic phases in the wires was not 100%. In Nitinol the presence of 100% Austenitic phase is reflected into Super Elastic Effect. In contrast, 100% Martensitic would have as outcome the Shape Memory Effect. The upper plateau stress for all the samples varied between 384 MPa and 466 MPa, while the ultimate stress reached approximately 1360 MPa at an ultimate strain of about 13%. The slope of the first loading stage of the response, the Elastic modulus, was calculated following the equation 11. The results are shown in table 5.10:

$$E = \frac{f_y}{\varepsilon_y} \text{ [11]}$$

Where: f_y is the stress before first plateau zone during loading and ε_y is the strain associated to f_y during loading.

Sample	f_y (Mpa)	ε_y (%)	E (MPa)
1	/	/	/
2	349	0,85	41059
3	363	0,84	43214
4	359	0,85	42235
Average	357	0,85	42169

Table 5.10: First elastic stage properties for 0.71 mm Nitinol wires.

The secant modulus (Es) in the last (plastic-hardening) phase of the test, was calculated using the stress at 7% strain and the stress at failure (US) following the equation 12. The results obtained are shown in table 5.11:

$$E_s = \frac{US - f_{7\%}}{El_u - 7\%} \text{ [12]}$$

Sample	$f_{7\%}$ (Mpa)	US (Mpa)	El_u (%)	E_s (Mpa)
1	478	1315	13	13950
2	519	1367	13,6	12848
3	517	1369	13,5	13108
4	520	1344	13,1	13508
Average	509	1348,8	13,3	13354

Table 5.11: Secant modulus of the Nitinol first type of wires.

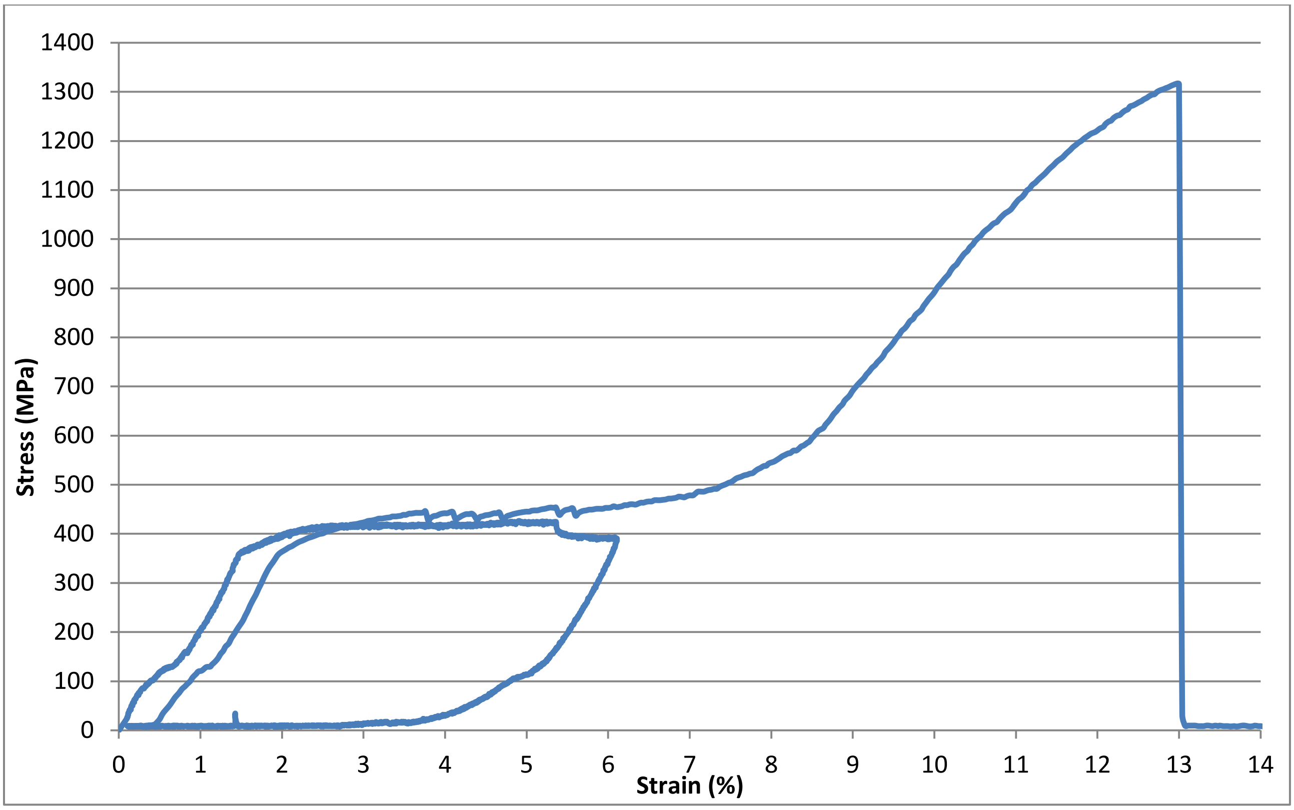

Figure 5.43: Stress-Strain response for specimen 1.

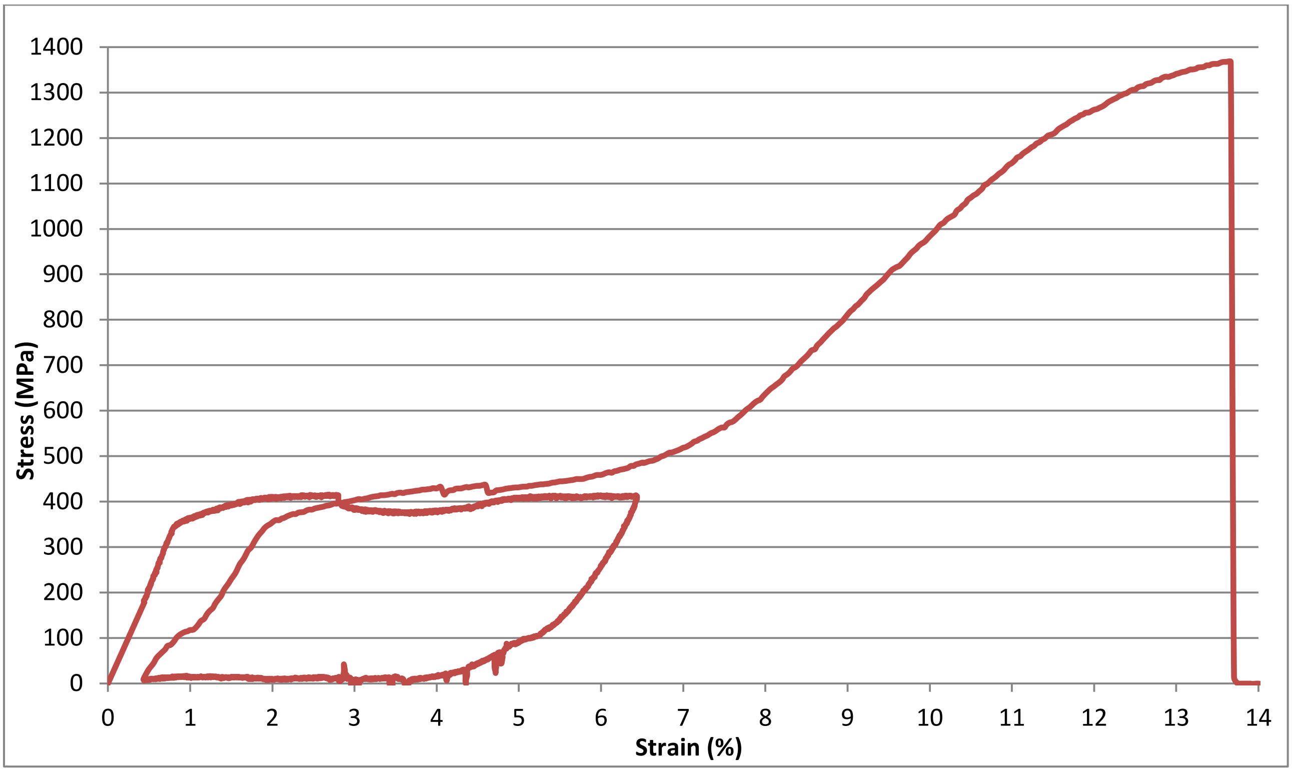

Figure 5.44: Stress-Strain response for specimen 2.

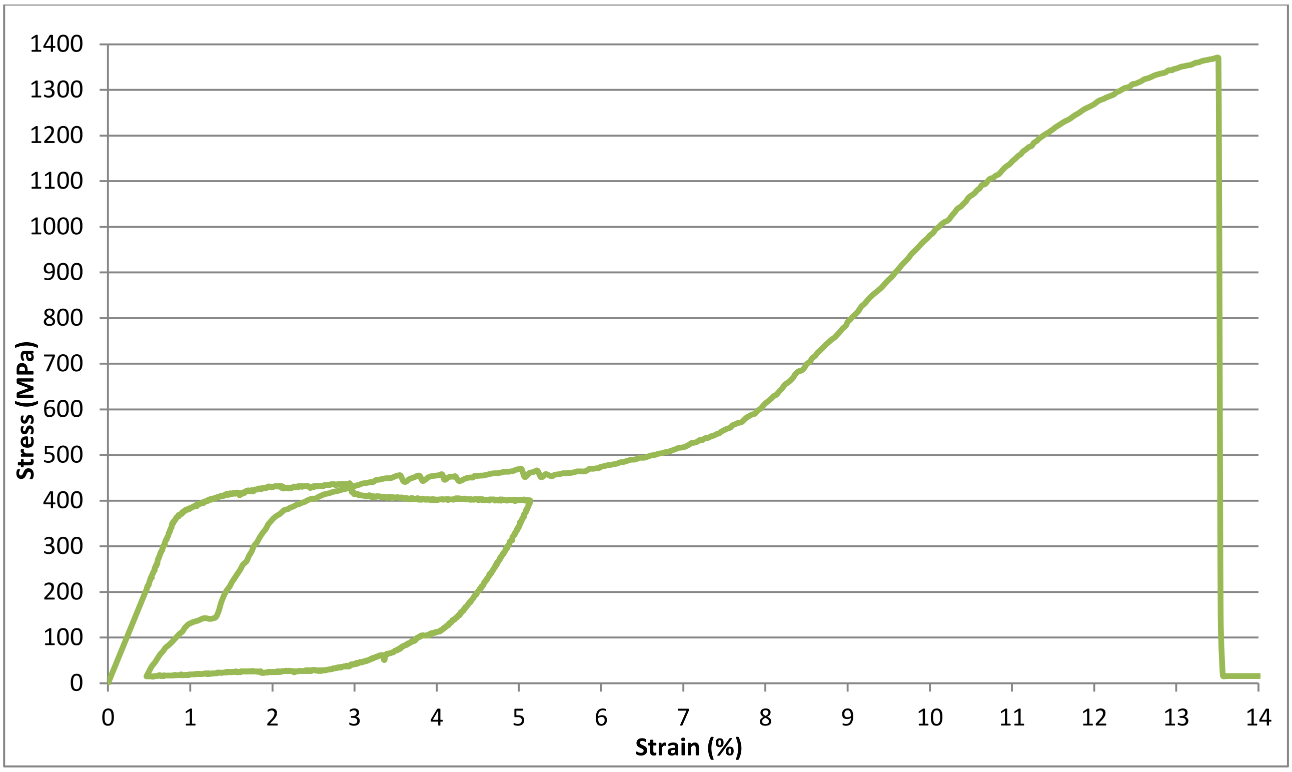

Figure 5.45: Stress-Strain response for specimen 3.

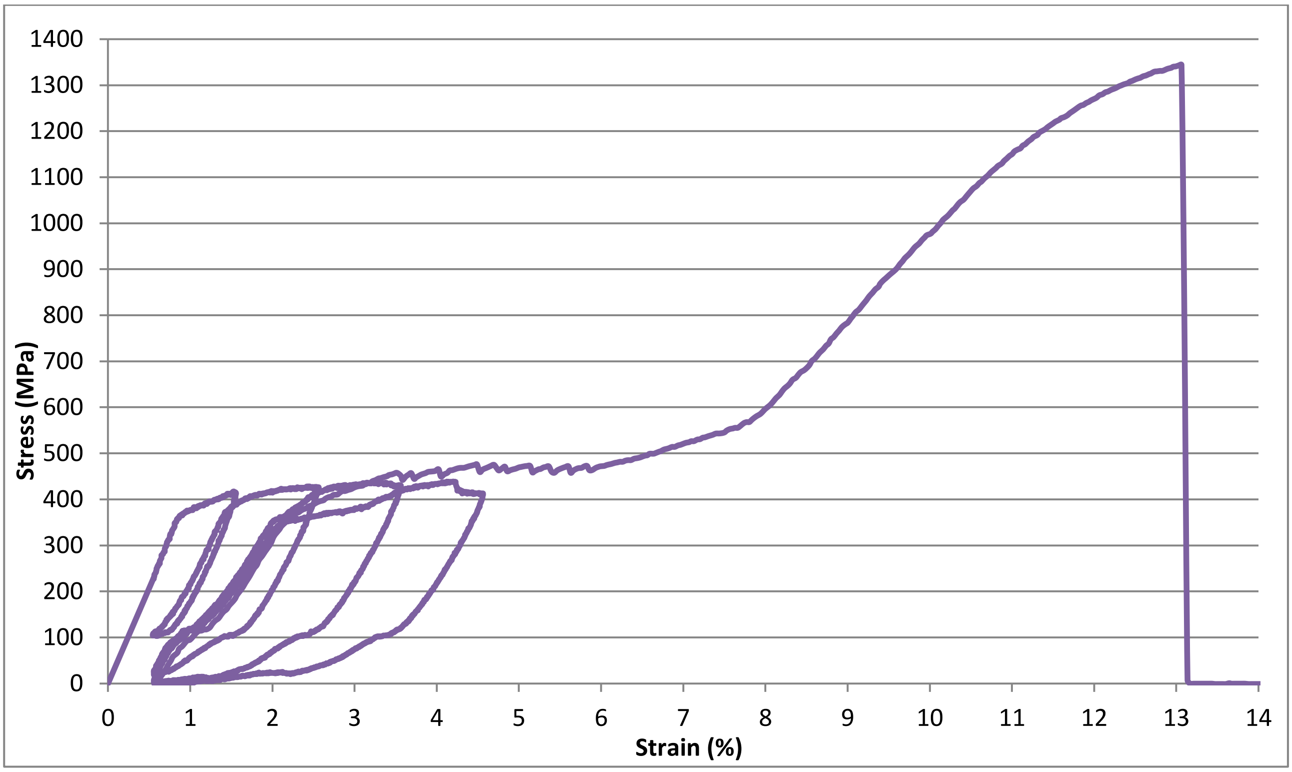

Figure 5.46: Stress-Strain response for specimen 4.

Based on the experimental responses obtained, it is possible propose a simplified tensile stress-strain diagram for numerical modelling, that could be used to predict the behaviour of this wire in the context of structural applications. The diagram is presented in figure 5.51 and includes two linear loading stages, one between 0% to 0,85% of tensile strain and the other between 0,85% and the recoverable strain of 7%, another linear unloading stage from 6% to 0%, and a final linear loading stage to simulate the final plastic hardening part.

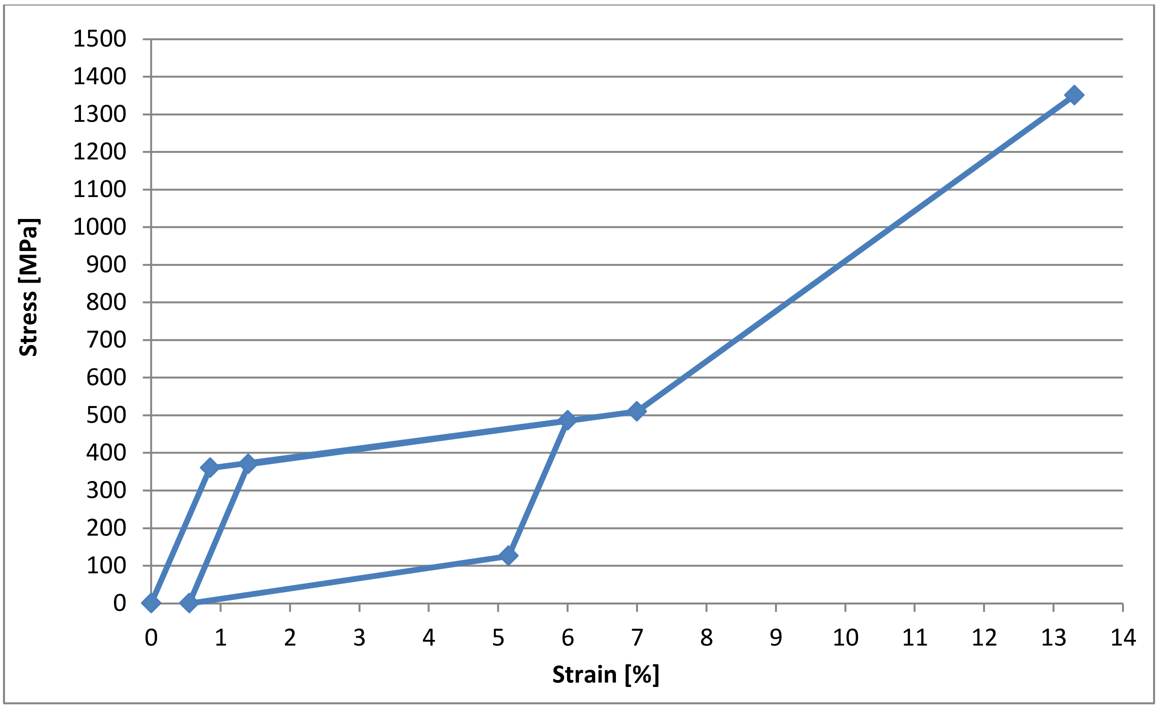

Figure 5.47: Simplified tensile stress-strain diagram for 0.71 mm wire.

Fist loading stage features:
- f_y=360 MPa
- e_y=0,85%
- E=42350 MPa

Second loading stage features:
- $f_{7\%}$=510 MPa
- E_{1-2}=2440 MPa

Third loading stage features:
- f_u=1350 MPa
- e_u=13,3%
- E_s=13333 MPa

First unloading stage:
- Recoverable strain=0,85%
- Slope=-42350 MPa

Second unloading stage:
- Recoverable strain=4,6%
- Slope=-2700 MPa

The *1,5 mm* diameter specimens exhibited slightly different tensile responses, as shown in figures 5.48 to 5.50. During the unloading stage the wire adopted a bended shape because it was unable to recover the original shape, due to the formation of plastic deformations before 6% strain. After the test, by applying heat to the wire it was possible to recover the initial shape. This behaviour is the typical Shape Memory Effect of Nitinol, which manifests when the stresses are applied at temperatures lower than Ms (Martensite start temperature). It is plausible to say that the Martensitic range temperature (Mf-Ms) is lower than in the previous wire. After these results it was decided to continue the tests removing the unloading stage from the procedure. In figures 5.49 and 5.50 the stress-strain diagrams of samples 2 and 3 are shown. In table 5.12 the Upper Plateau Stress, Ultimate Stress and Uniform Elongation for all the samples are reported.

Sample	UPS (Mpa)	US (Mpa)	El_u (%)
1	146	1390	24
2	141	1383	24

3	154	1393	22,5
Average	147	1389	24

Table 5.12: Properties of the first type of Nitinol wires, according with ASTM F2526-07.

In addition, it is possible to identify other differences when comparing with the first type of wire tested: a lower value of the upper plateau stress is obtained in the second case, and the ultimate strain reaches a much higher value (about 24%). This second type of wires was softer than the first one, most likely due to the almost 100% fraction of Martensitic phase at the temperature conditions occurring during the tests. In tables 5.13 and 5.14 the Elastic modulus for the first stage and secant modulus were calculated based on equations n. 11 and 12.

Sample	f_y (Mpa)	ε_y (%)	E (MPa)
1	135	1,5	9000
2	134	1,24	10806
3	138	1,31	10534
Average	136	1,35	10114

Table 5.13: first loading trait properties.

Sample	$f_{6\%}$ (Mpa)	US (Mpa)	El_u (%)	E_s (Mpa)
1	206	1390	24	6578
2	200	1383	24	6572
3	218	1393	22,5	7121
Average	208	1388,7	23,5	6747

Table 5.14: third loading trait properties.

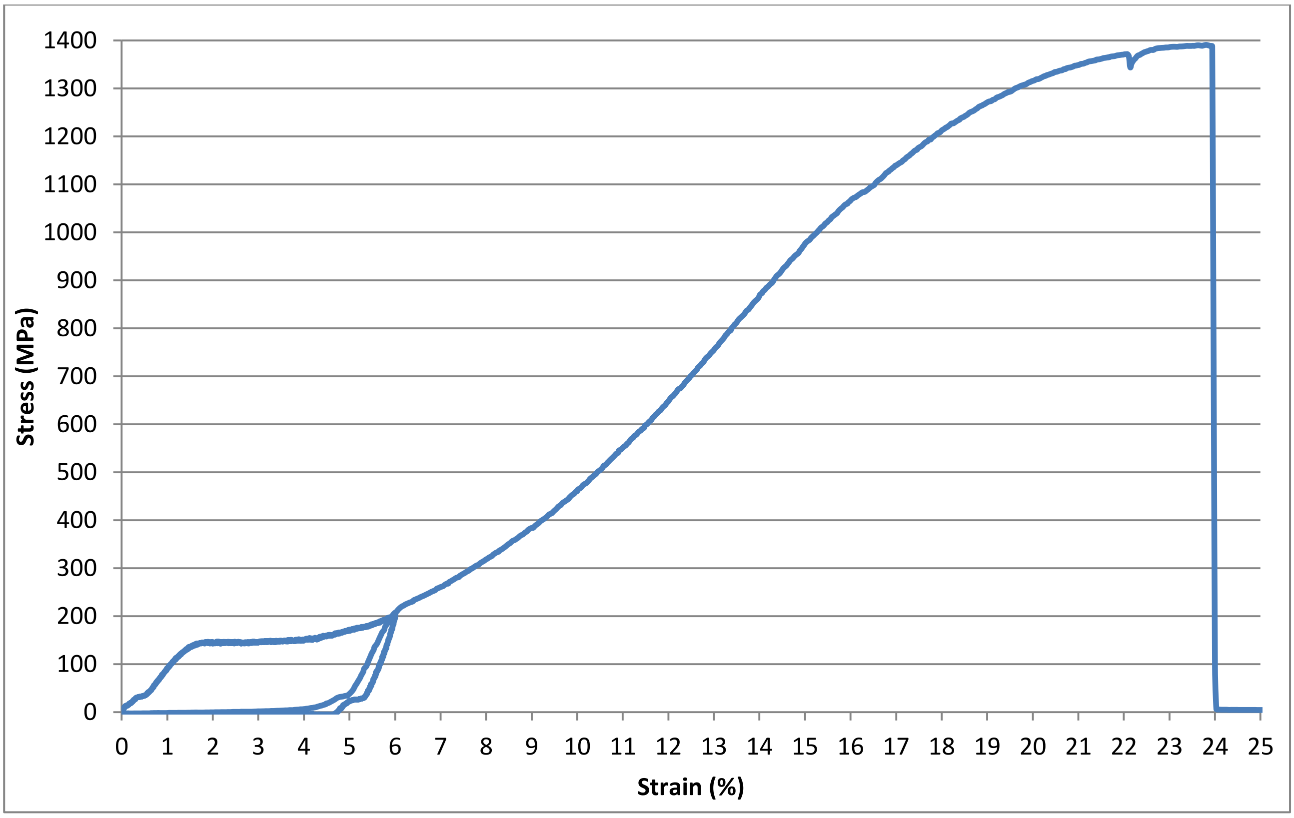

Figure 5.48: Stress-Strain response for specimen 1.

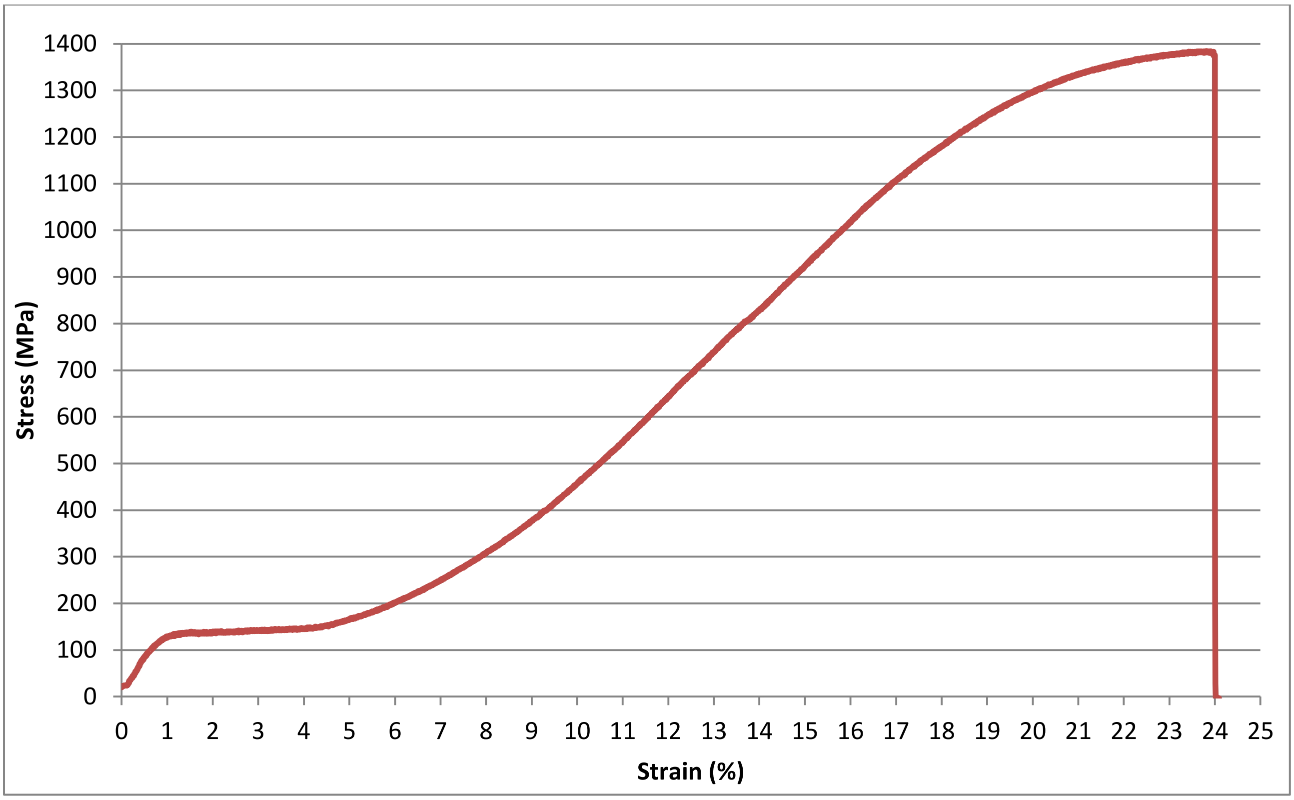

Figure 5.49: Stress-Strain response for specimen 2.

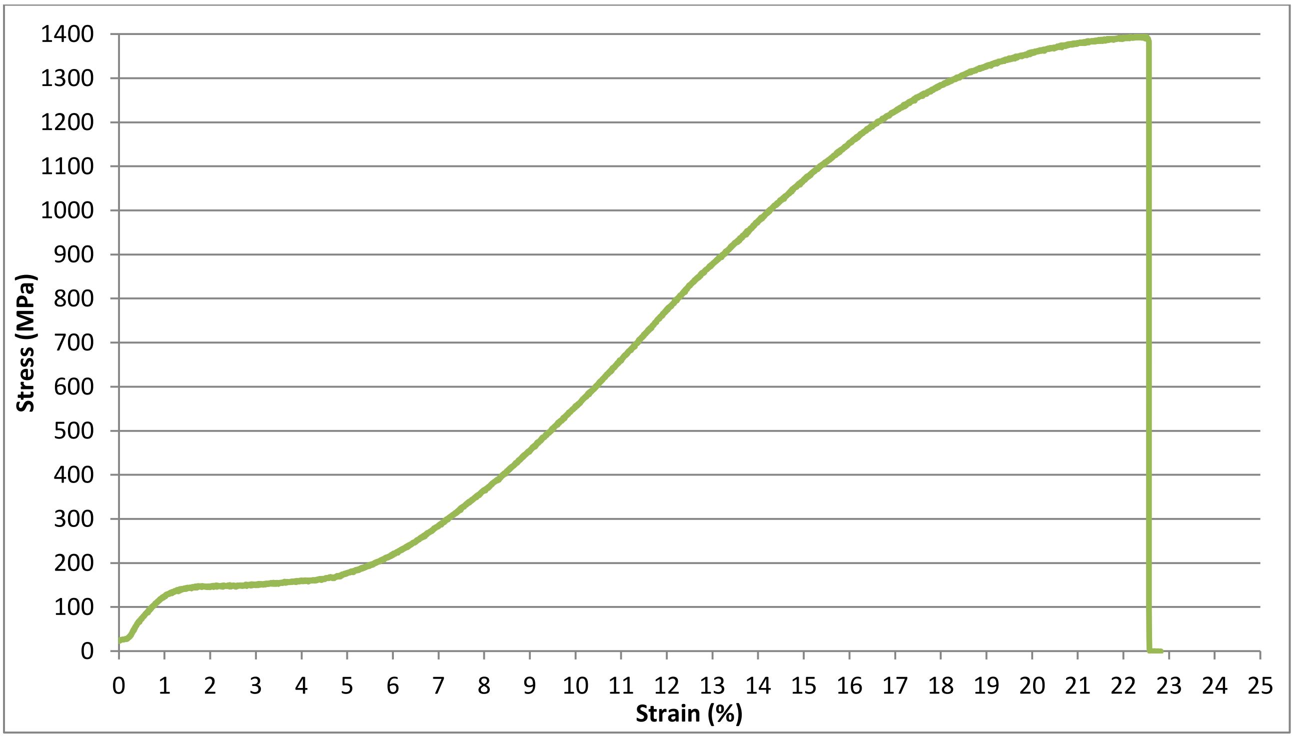

Figure 5.50: Stress-Strain response for specimen 3.

With these data, is possible to obtain a simplified diagram, that could be used to predict the behaviour of this second type of wires in future applications. The diagram showed on figure 5.55, includes three linear traits from 0% to 1,35%, from 1,35% until 6% and from 6% to failure, and two unloading traits.

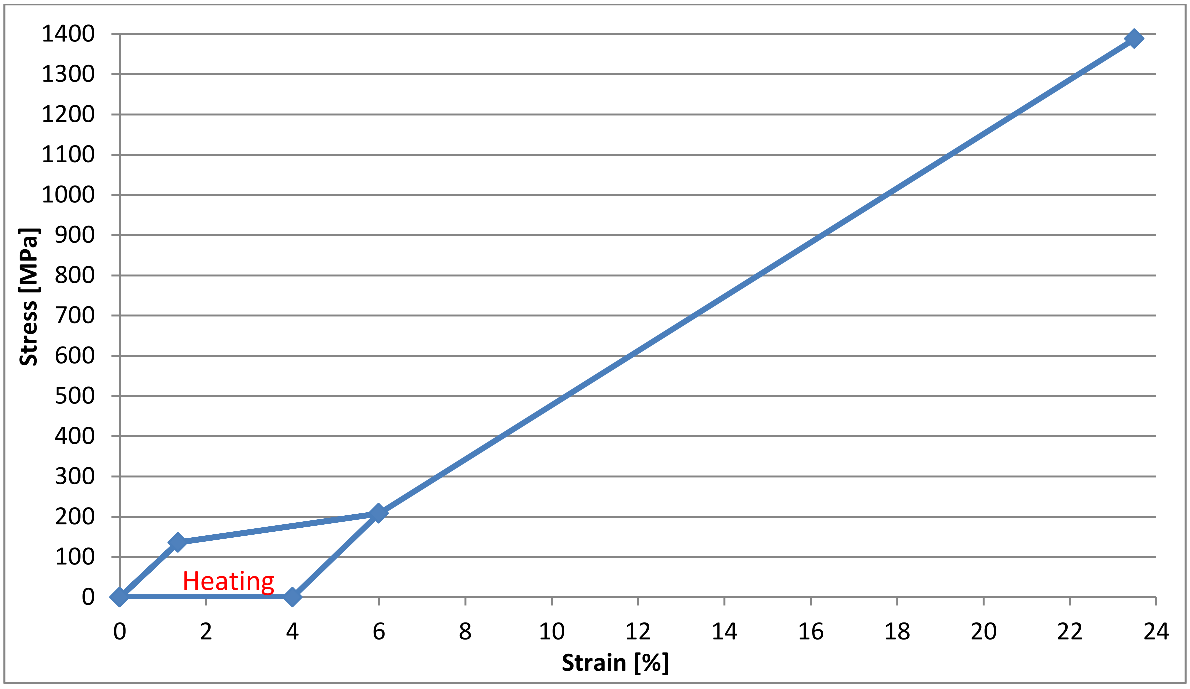

Figure 5.51: Simplified tensile stress-strain diagram for 1.5 mm wire .

Fist loading stage features:

- f_y=136 MPa
- e_y=1.35%
- E=10074 MPa

Second loading stage features:

- $f_{6\%}$=208 MPa
- E_{1-2}=1548 MPa

Third loading stage features:

- f_u=1388 MPa
- e_u=23,5%
- E_s=6743 MPa

First unloading stage :

- Recoverable strain=2%
- Slope=-10074 MPa

Second unloading stage (heating):

- Recoverable strain=4%
- Slope=0 MPa

After comparing the results of the two wires, the first wire (0,71 mm diameter) was chosen to proceed with this investigation, since it exhibited a tensile behaviour that is closer to the optimal super-elastic effect desired. The wire was used as reinforcement of M3-4R composite specimens and to prepare the specimens used to characterize the adherence between ECC and Nitinol.

Bibliography

[1] ASTM International (2008); ASTM F2516-07: Standard Test Method for Tension Testing of Nickel-Titanium Superelastic Materials.

6. ECC-NiTinol Composite for Strengthening

ECC and SMA are innovative materials that possess interesting features for extreme applications in Civil Engineering, as studied in the previous chapters. In the subsequent sections the concept of joining these two materials in a hybrid composite will be explored. The main objective is to obtain structural elements that can undergo *high deformations* and allow *greater energy dissipation*, with a *greater damage tolerance* than common reinforced concrete elements and with self-recentring capabilities. The main idea is to use NiTinol as reinforcement for ECC composite, exploiting the super-elastic effect of NiTinol wires to help ECC composite to increase the strength, the ultimate strain and to partially recover the plastic deformation under tensile loading.

To develop this composite, first the interaction between SMA wire and ECC mortar will be characterized through pull-out tests. The pull-out test allow to describe the mechanical interaction between the two materials at the level of the interface. This characteristic is fundamental for a truly composite and combined interaction of the two materials in the hybrid composite. Afterwards, the behaviour of the composites will be studied under tensile and cyclic loads. Finally a scaled model of a bridge column will be tested under cyclic loading, as a proof of concept in a seismic scenario.

6.1 Pull-Out Test: Friction between ECC Mortar And Nitinol

6.1.1 Geometry of the Specimens

The aim of these tests was to characterize the interaction between ECC mortar and Nitinol wires at the level of the interface. For this purpose the specimens were casted, using square tubes made of plastic with four different lengths: 30 mm, 60 mm, 90 mm, 120 mm. A wide range of different embedment lengths were planned because the information about the friction properties between smooth Nitinol and concrete are scarce. The first group of specimens contained one 0,71 mm diameter Nitinol wire, which was immersed in the ECC mortar throughout the entire length of the tube and with an additional length of free wire of approximately 80 mm. In order to keep the wire in the right position during casting and before the mortar has hardened, four steel clips have been used, as shown in figure 6.1.

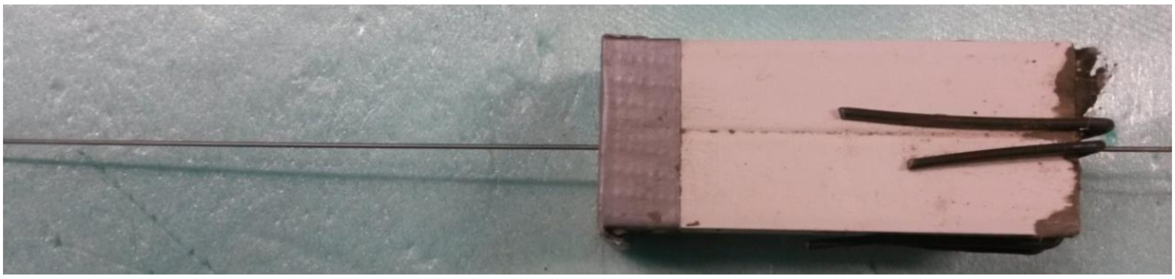

Figure 6.1: 60 mm pull-out specimen containing 1 wire.

The second group of specimens contained two 0,71 mm diameter wire twisted, with a twist spacing of10 mm. These specimens were produced with the purpose to evaluate the possible increase of friction between the wire and the mortar due to twisting. In order to keep the wire twisted and straight until the mortar has hardened, it was necessary to use once more four steel clips and other improvised connectors made of electrical current connectors and hot glue, as shown in figure 6.2.

Figure 6.2: 60 mm pull-out specimen containing 2 twisted wires.

The mixture M3-4R was used to cast the specimens in both cases. After casting, the specimens were kept for 28 days in a 20°C ventilated room.

6.1.2 Test Set-up

Before testing, the specimens were cut and 10 to 20 mm were subtracted to the lower edge of the specimens in order to obtain two parallel and rectified edges, as well as to remove the less homogeneous part of the casted specimens. In figures 6.3 and 6.4 the final specimens are shown.

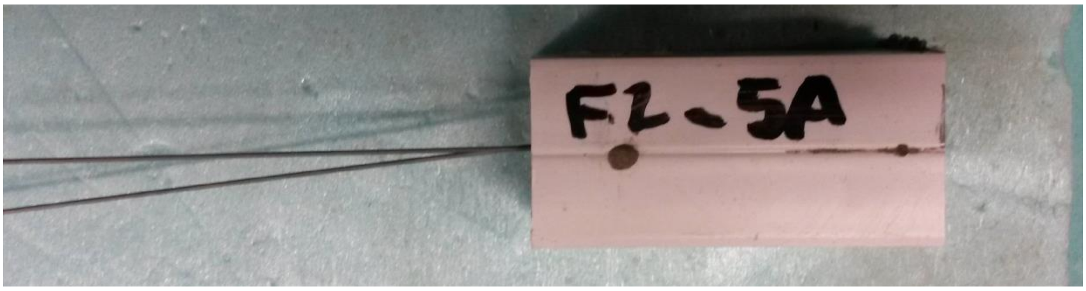

Figure 6.3: 50 mm pull-out specimen after cutting, containing 2 twisted wires.

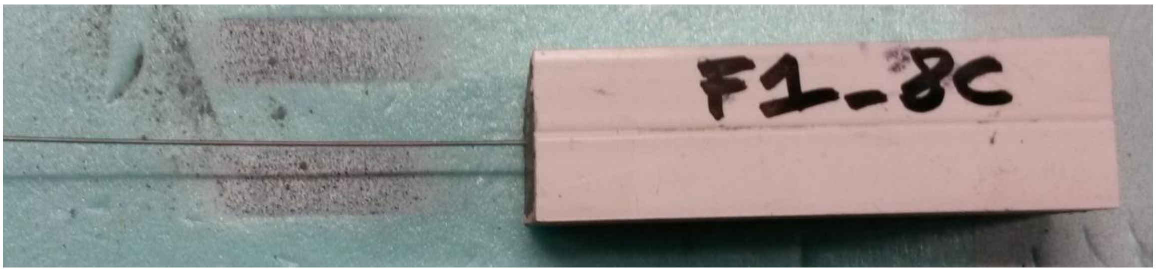

Figure 6.4: 80 mm pull-out specimen after cutting, containing 1 wire.

The test setup consisted on fixing the specimens in two clamps: one clamp was used to fix the plastic tube and the other clamp was used to fix the wire edge. In order to increase the friction between the grips and the wire, thin sandpaper was used, as previously reported. One 10 KN load cell was connected to an actuator, and one LVDT was used to measure the displacement in in the loaded end of the wire. All tests were carried out under displacement control, with an imposed displacement at a constant displacement rate of 0,05 mm/sec. Figures 6.5 and 6.6 show the test set-up in detail.

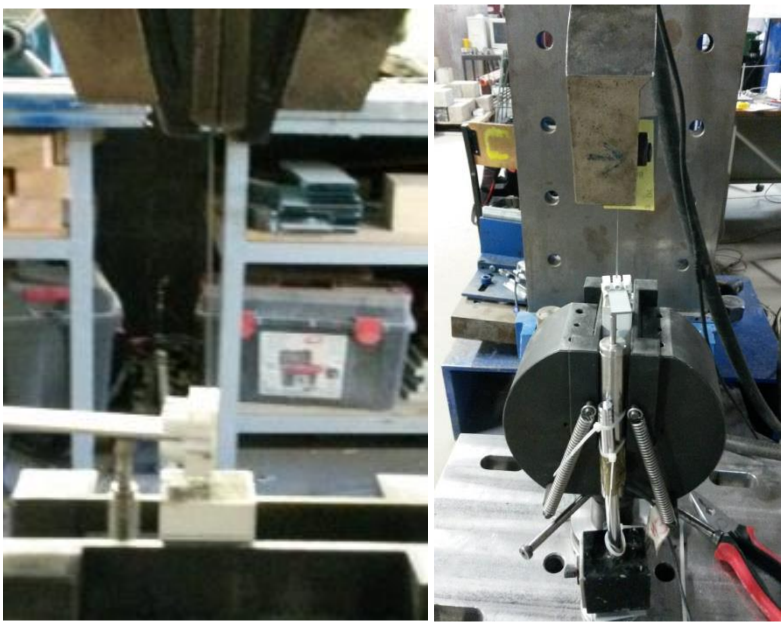

Figure 6.5: Close-up of the pull-out test setup.

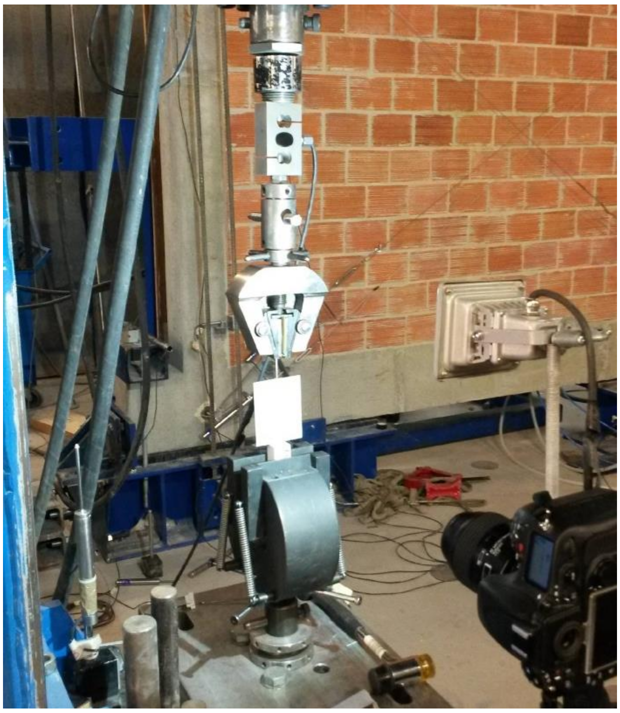

Figure 6.6: Setup used to capture high resolution images during pull-out testing.

6.1.3 Results

Figures 6.7 to 6.14 show the results the results obtained in terms of the tensile stress on the wire versus the displacement of the actuator. The tensile stress on the wires was calculated using equation 13:

$$\sigma = \frac{F}{A_w} \quad [13]$$

Where: F is the applied force, σ is the stress, A_w is the area of the cross-section of the wire.

The responses obtained for the first specimens, containing 1 wire, showed in general a first stage where the stresses on the wire increase linearly until the peak stress of about 380-400 MPa was reached. After this peak the wires started slipping and the force necessary to pull the wires from the ECC mortar decreased, most of the time with a pseudo-linear behaviour. Sudden increases or decreases of the pull-out force during the second stage were not expected. The explanation for these results may lye on a differentiated phase transition occurring throughout the embedded or the free zones of the wires, or to non-perfectly straight alignment of the wire inside the matrix. Further tests would be necessary to clarify the responses obtained.

Based on the results obtained, it seems that the friction between one smooth wire and the ECC was not sufficient to completely fix the wire and cause its failure, even with the longer specimens. In fact, the maximum stress reached in the wires did not exceed 400 MPa while the NiTinol wires tested in tension reached tensile strengths higher than 1350 MPa. This behaviour could be attributed not only to the very smooth type of surface that the wires possess, but also to the high Poisson coefficient of this alloy, that is 0,33. In fact during the test, while the wire undergoes significant tensile strains, for a high Poisson coefficient the reduction of the cross-section area increases the detachment effect of the wire from the matrix, therefore reducing the friction and making it easier for the wire to slip out of the matrix.

Another important observation is that the maximum stresses reached by the wires varied in range between 310 to 400 MPa, even when the length of the ECC specimen was increased. This could be attribute to the presence of some air bubbles in the tubes. This problem was solved in the subsequent specimens by performing small holes along the plastic tube, in order to allow the release of the air during casting.

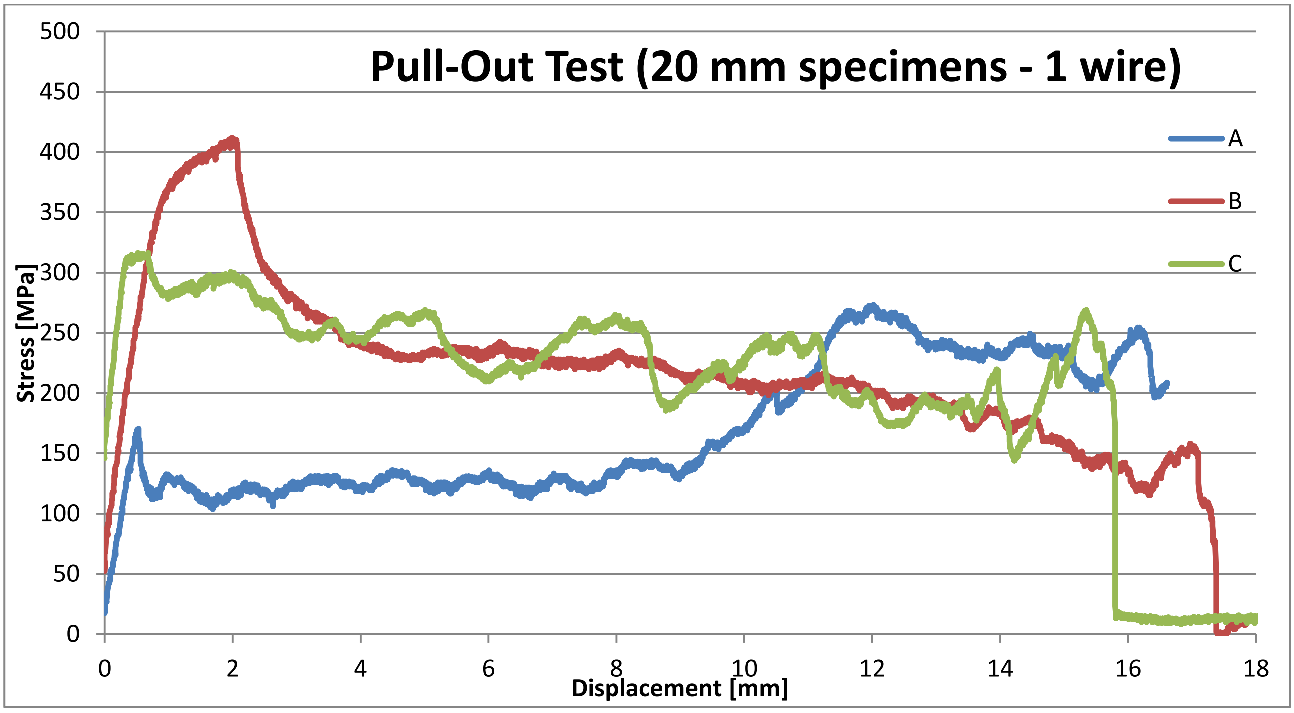

Figure 6.7: Tensile stress versus loaded end displacement responses for the 20 mm pull-out specimens containing 1 wire.

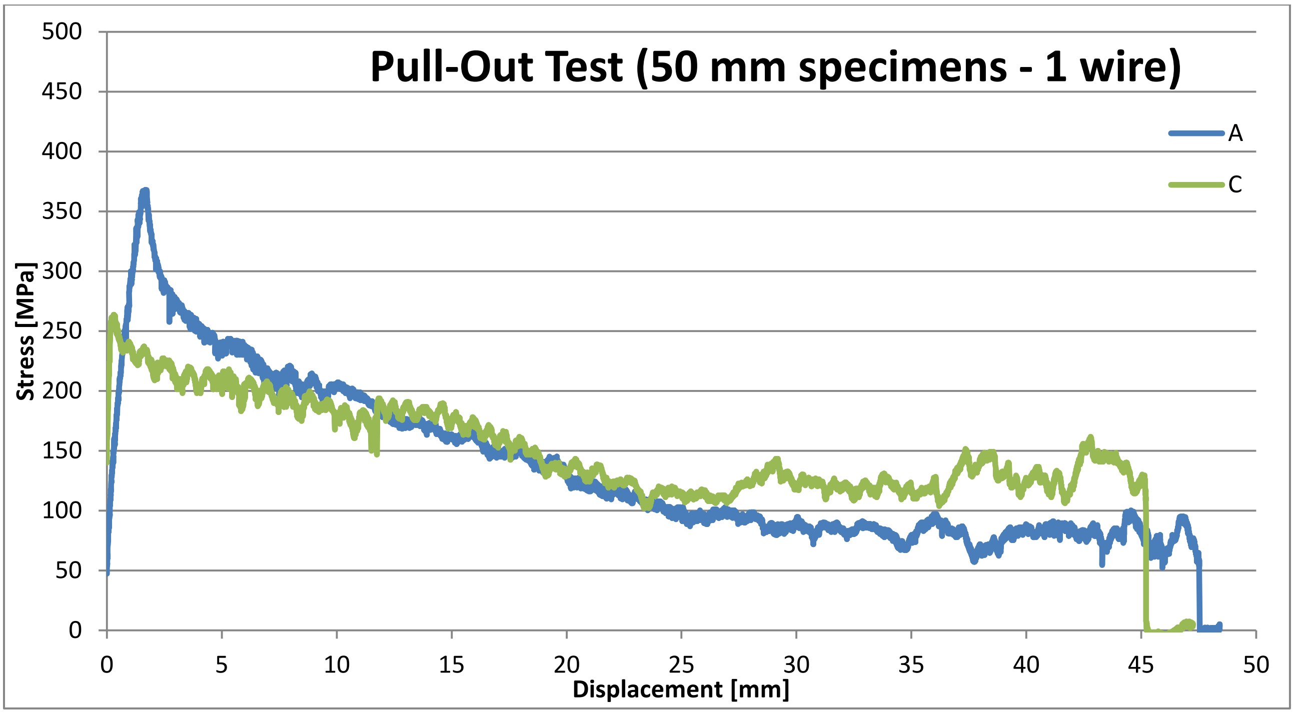

Figure 6.8: Tensile stress versus loaded end displacement responses for the 50 mm pull-out specimens containing 1 wire.

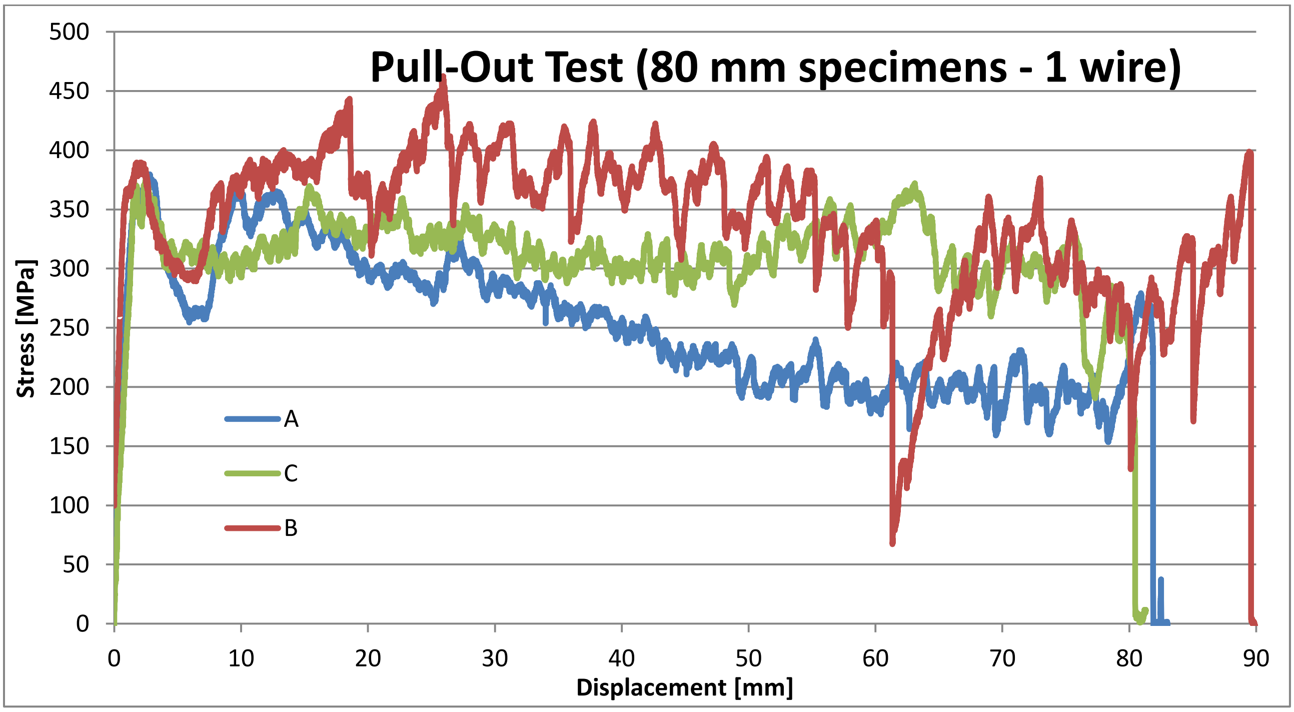

Figure 6.9: Tensile stress versus loaded end displacement responses for the 80 mm pull-out specimens containing 1 wire.

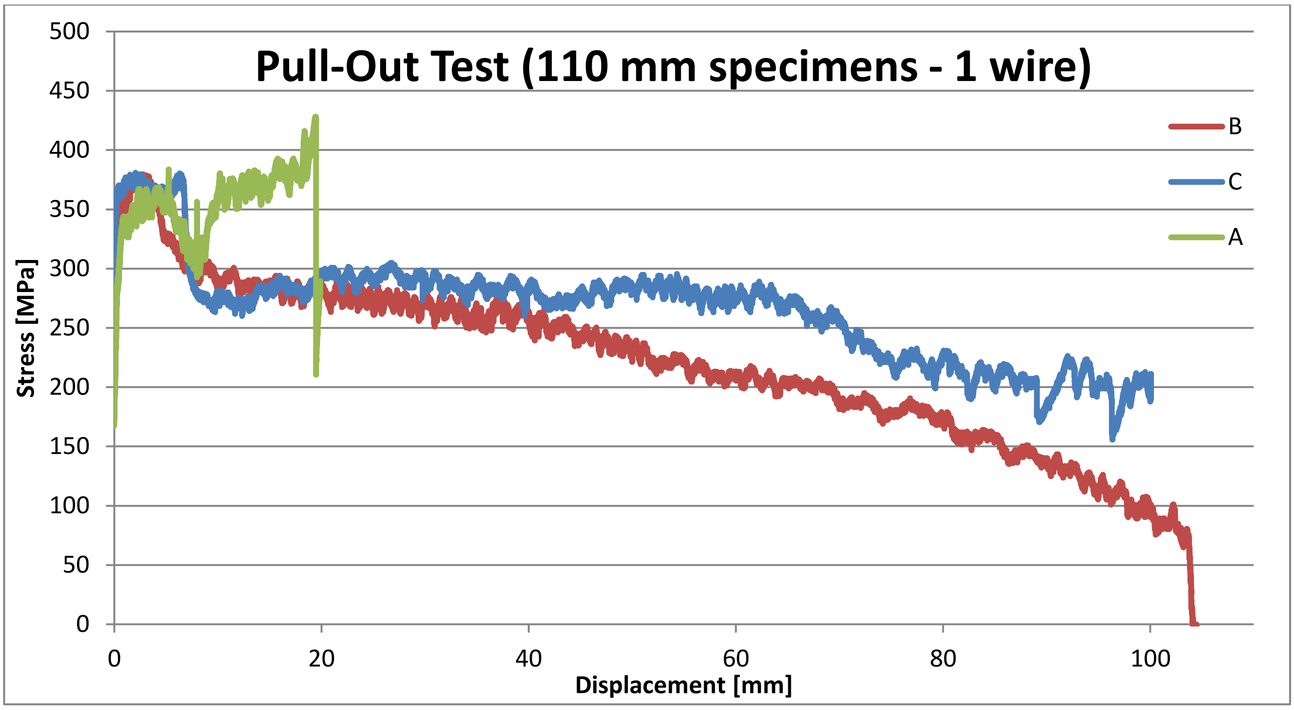

Figure 6.10: Tensile stress versus loaded end displacement responses for the 110 mm pull-out specimens containing 1 wire.

The second series of pull-out tests was performed using twisted wires. In this case the obtained responses showed an increase of the maximum stresses experienced by the wires with the increase of the length of the embedded length. In fact the 20 mm specimens reached only a tensile stress of 175 MPa in the first stage, while the 40 mm specimens reached 400 MPa, also in the first stage. The specimens with lengths of 70 mm, 90 mm and 110 mm have reached even higher tensile stresses on the wires. In contrast to what was observed with the single wire specimens, the peak stresses on the wires were reached in the second stage for stresses between 600 MPa and 900 MPa. The peak stress was reached by following closely the typical shape of the tensile stress-strain responses obtained previously for the single wires, which means that only the free part of the wire is deforming and the embedded part remains undeformed. After reaching the peak the wire started to slip from the mortar and the force necessary to pull it out decreased slowly.

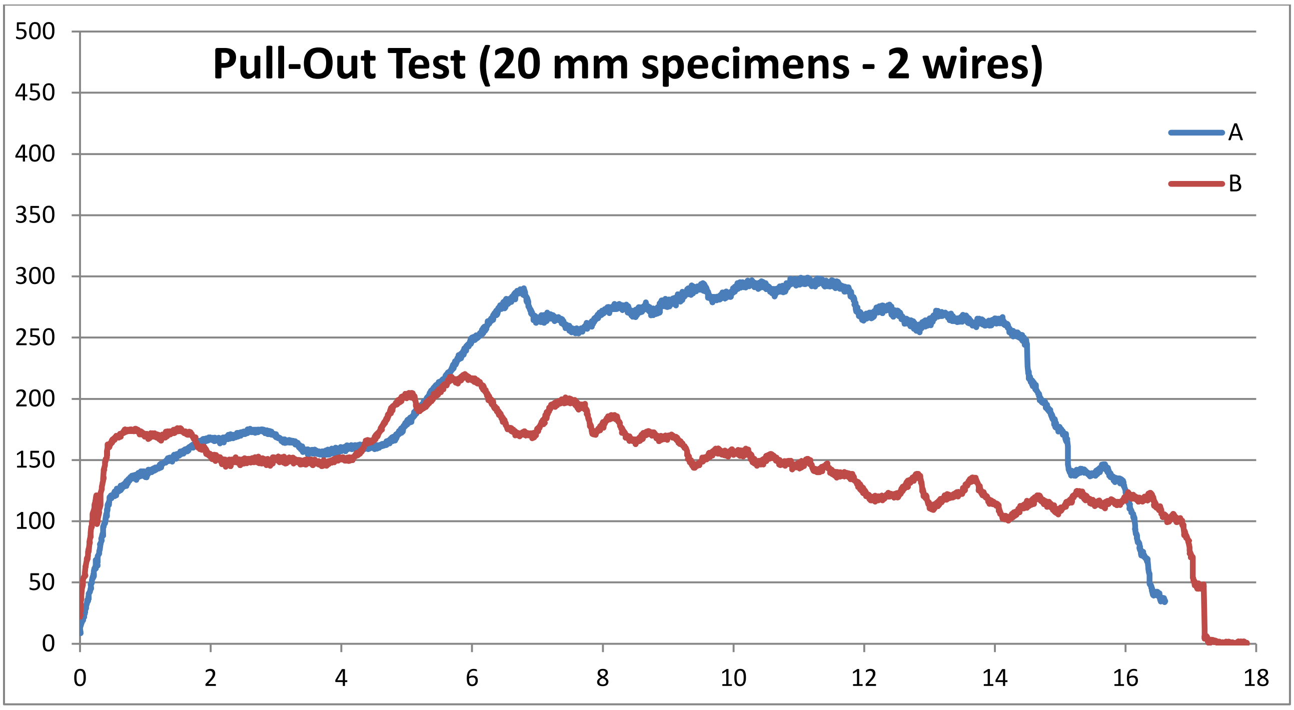

Figure 6.11: Tensile stress versus loaded end displacement responses for the 20 mm pull-out specimens containing 2 wires.

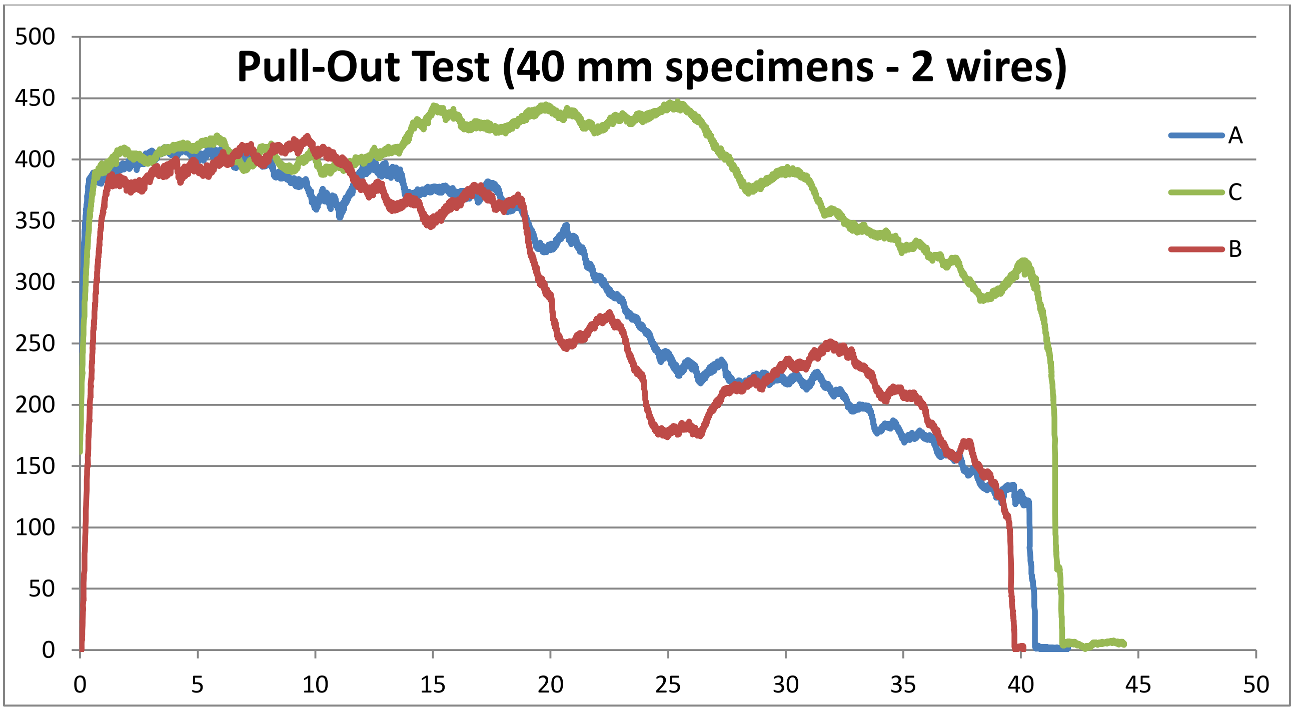

Figure 6.12: Tensile stress versus loaded end displacement responses for the 40 mm pull-out specimens containing 2 wires.

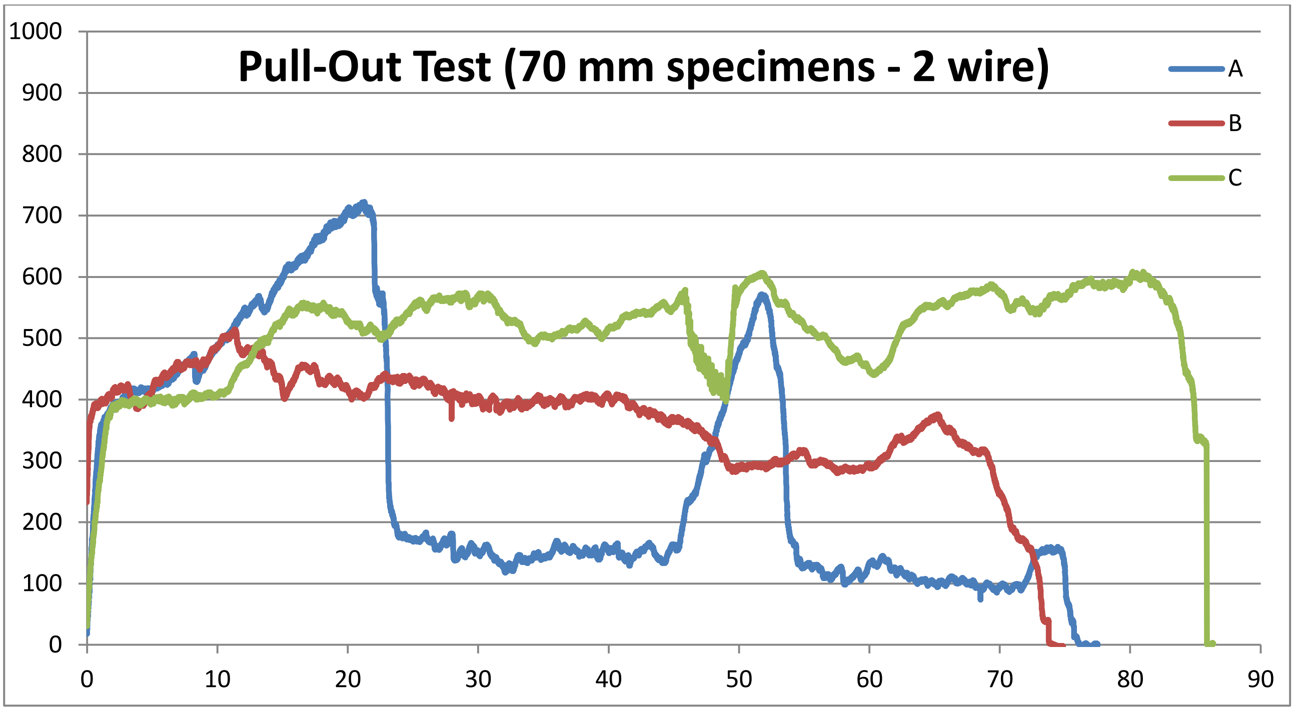

Figure 6.13: Tensile stress versus loaded end displacement responses for the 70 mm pull-out specimens containing 2 wires..

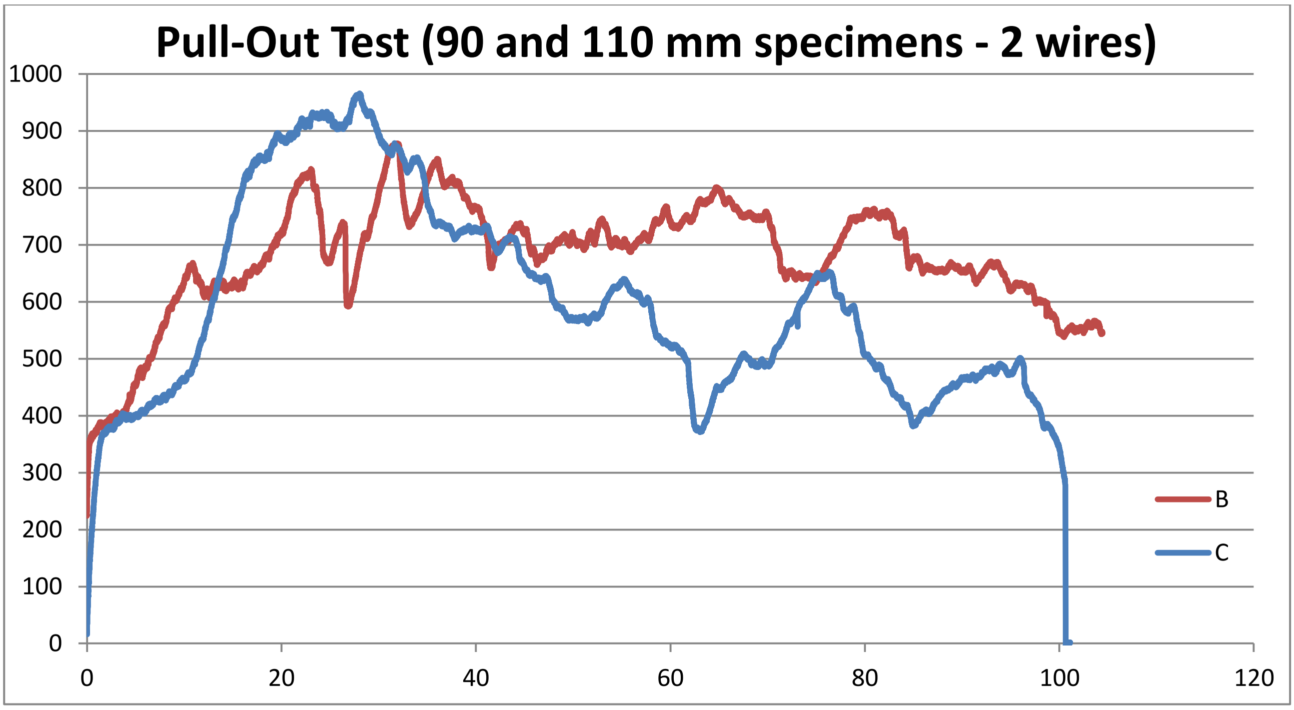

Figure 6.14: Tensile stress versus loaded end displacement responses for the 90 mm (C) and 110 mm (B) pull-out specimens containing 2 wires.

Considering all the results obtained, it is possible to estimate that, even if the length of the specimens containing one wire was increased, it would be very difficult to reach enough bonding force to completely fix the wire and pull it until it ruptures. The maximum stress that the wire can reach in the single wire pull-off specimens before starting to slip is approximately 350 MPa, which should be a good estimate of the adhesion stress. By twisting the wire it was possible to increase the friction stress between the two materials beyond the adhesion. The maximum stresses in the wire increased with the length of the specimen and reached 800-900 MPa in the longer specimens, as shown in figures 6.15 and 6.16. It is possible to anticipate that, with a slightly longer specimen, it would be possible to reach the twisted wire rupture, which would allow to obtain directly the stress transfer length required to fully mobilize the wire in the hybrid composite.

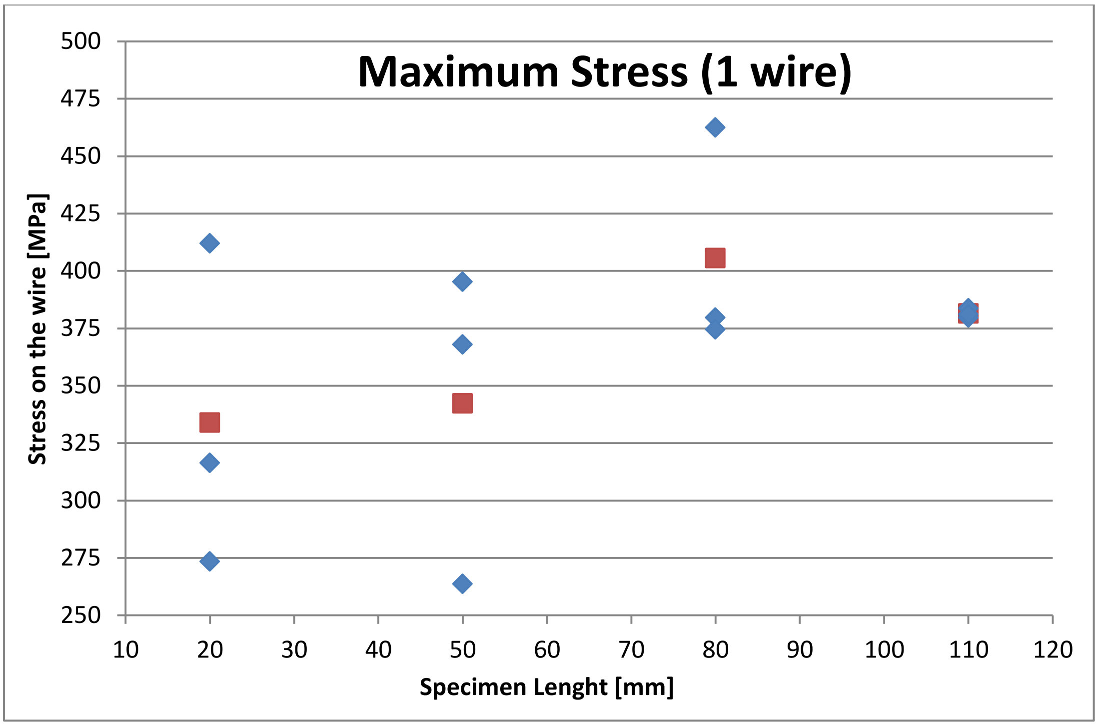

Figure 6.15: Maximum wire stresses attained in the single wire pull-out specimens.

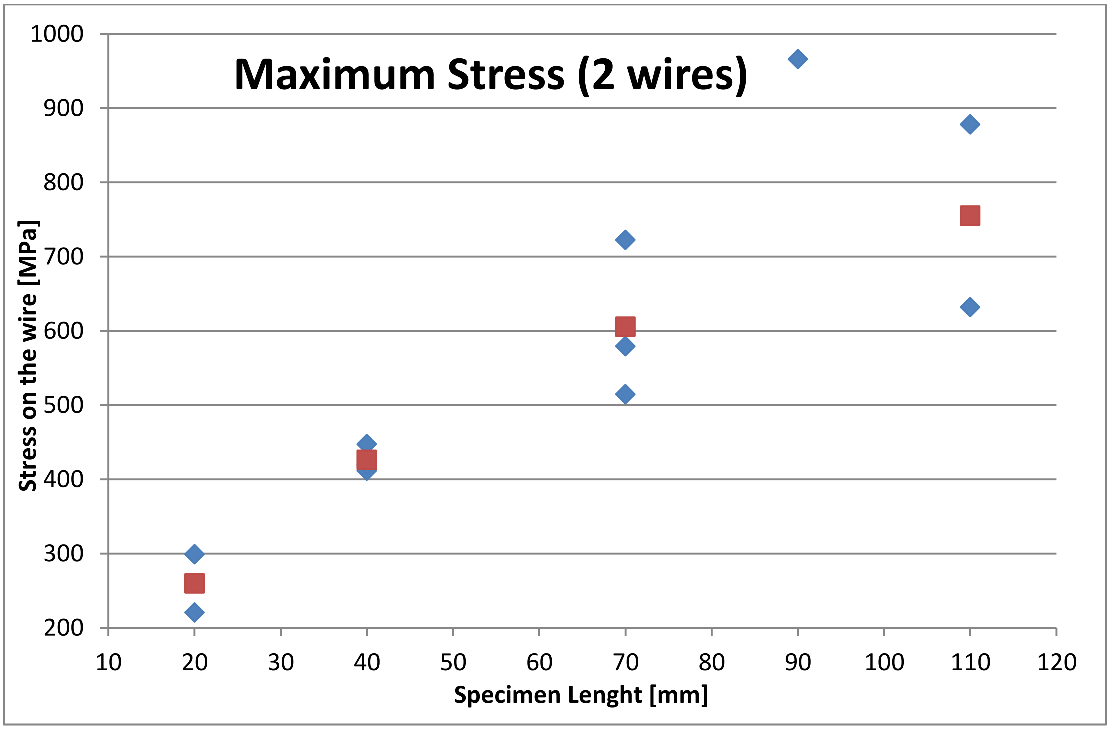

Figure 6.16: Maximum wire stresses attained in the twisted wire pull-out specimens.

6.2 Hybrid Specimens of ECC Reinforced With NiTinol

6.2.1 Aims

Hybrid specimens of ECC reinforced with NiTinol were characterized in direct tension in order to verify the compatibility of these two materials. The initial objectives were to increase the ductility of the composite under tensile loading, as well as to enhance even further the pseudo strain hardening behaviour typical of ECC by improving the multiple cracking behaviour and the tensile strength by using a ductile reinforcement with super-elastic behaviour. The ability to partially recover the deformation after large imposed tensile strains by exploiting the Super-Elastic effect of the NiTinol was also searched.

6.2.2 Production of the Specimens

The ECC composite was poured into the acrylic moulds previously used for casting the dogbone-shaped tensile specimens. Four dogbone-shaped specimens reinforced with 6 NiTinol wires, which represent 0,47% of the cross-section of the cementitious composite, were casted. The procedure followed to fix the 6 wires in the mould was carefully developed in order to avoid the entanglement of the wires and their correct placement in the section during casting and vibration, which was particularly difficult due to the super-elastic effect. The procedure was composed by the following steps:

- The wires were placed in a wood plate and fixed with 12 improvised connectors made of electric current connectors, located at the edges of the plate as shown in figure 6.17.

Figure 6.17: Wood plate with the connectors fixed at the edges using super glue and hot glue.

- The stretched wires were glued between two plastic plates using hot glue and epoxy glue, in order to assure the correct position of the wires in the final section. After 48 hours of glue curing the wires were removed from the wood plate, as shown in figure 6.18.

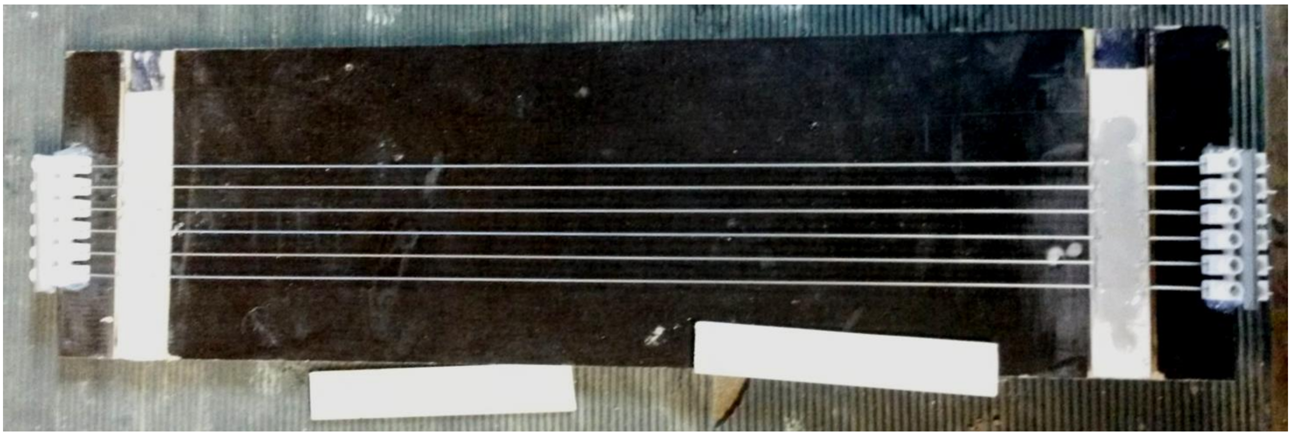

Figure 6.18: Wires stretched and fixed on the edge connectors during the addition of epoxy glue to the anchoring plastic plates.

- The wires were placed in the mould using a temporary mechanical device that avoids the entanglement of the wires. The plastic plates were fixed to the mould using L screws glued with hot glue while the wires were kept stretched, as shown in figure 6.19.

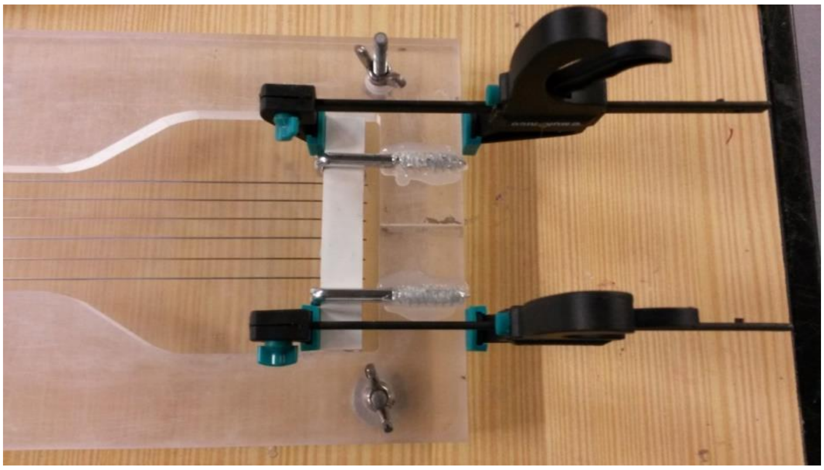

Figure 6.19: Plastic plate fixed at the edge of the mould using mechanical devices to stretch and hold it, while the “L” screws were fixed to the mould using hot glue.

- The mechanical devise were removed and the ECC composite was poured into the moulds. The air bubbles were removed from the composite by placing the mould in the shaking table for 2 minutes.
- The specimens were placed in a 20°C ventilated room for 28 days. After one day of curing the“L” screws were removed.

Three dogbone-shaped specimens containing 6 twisted wires, which represent 0,94% of the cross-section of the cementitious composite, were casted. The procedure to fix the twisted wires in the mould was practically identical to the one previously reported for the case of the 6 single wires, but it was necessary to proceed with more precaution in order to avoid the wire entanglement and the damage of the specimens and the equipment. The procedure included:

- The twisting of the wires, which were twisted 10 times on each edge using a screwdriver.
- To remove the wires from the wood-plate, it was necessary to use a wood device that kept immobilized the stretched wires between the two plastic plates due to the increased rotational force and the risk of entanglement of the wires.
- Small pieces of wood and steel wires were used to tighten the “L” screws and keep them in the right position during gluing operations, as shown in figure 6.20.

Figure 6.20: Twisted wires placed in the mold. The plastic plates were fixed using “L” screws, hot glue, small wood pieces and steel wire.

6.2.3 Test Set-Up

The tests on the hybrid ECC dogbone specimens were carried out using the same set-up as before, for the case of the tensile tests on ECC dogbone specimens. The subsequent testing sequences were carried out:

The subsequent testing procedures have been carried out:
- Monotonic tensile testing under displacement control.
- Cyclic testing (1%): initial loading of the specimen in tension until 1% strain was reached, under displacement control, and subsequent unloading until 0% strain was reached also under displacement control. the same procedure was repeated 4 times, after which the specimen was subjected to an imposed tensile deformation under displacement control until failure.
- Cyclic (+1%) DC: initial loading of the specimen in tension until 1% strain was reached, under displacement control, and subsequent unloading until 0% strain was reached also under displacement control. The same sequence was repeated but reaching the tensile strain of 2%, 3% and 4%, and finally the specimen was loaded in tension until failure, under displacement control.

All tests were carried out under displacement control subjected the specimens to displacement increments at a constant rate of ±0,015 mm/s. Tensile stresses and strains have been computed using the equations 7 and 8:

6.2.4 Results and Discussion

As shown in figure 6.21, the monotonic tensile tests on two ECC dogbone specimens reinforced with six 0,71 mm diameter NiTinol wires resulted in a reduction of the ultimate strain with respect to the unreinforced ECC specimens. The multiple cracking observed previously in the unreinforced ECC specimens was much less evident. The localization of tensile deformations occurred much sooner than in the previous specimens, and a fully open crack was obtained for a tensile strain of 2% strain. After this point the specimens still have strength, due to the presence of the wires which remain intact. The ultimate stress reached 4 MPa, the same value obtained before with the unreinforced ECC specimens.

The reason behind the reduction of ductility lies on the *low bonding* between Nitinol and ECC material, which was observed experimentally with the pull-out tests. Once a new crack appears on the specimen, part of the force transmitted previously by the intact composite must be transferred into the wires. Because the bonding stress between the matrix and the wires is so low, the stress transfer length is very large compared with the length of the specimen. For this reason, the new peak of stress which could originate new cracks lies too far from the original crack. For example, if the ECC before cracking is undergoing 4 MPa stress, if the contribution of the fibre bridging is neglected that means that a force of 2 KN must be transferred to the wires, which translates into a tensile stress of about 800 MPa. This stress level is very difficult to transfer back to the ECC mortar considering the low friction coefficient between these two materials. Therefore the hybrid composite loses efficiency and the stresses reached do not increase, as well as the formation of new micro-cracks is reduced.

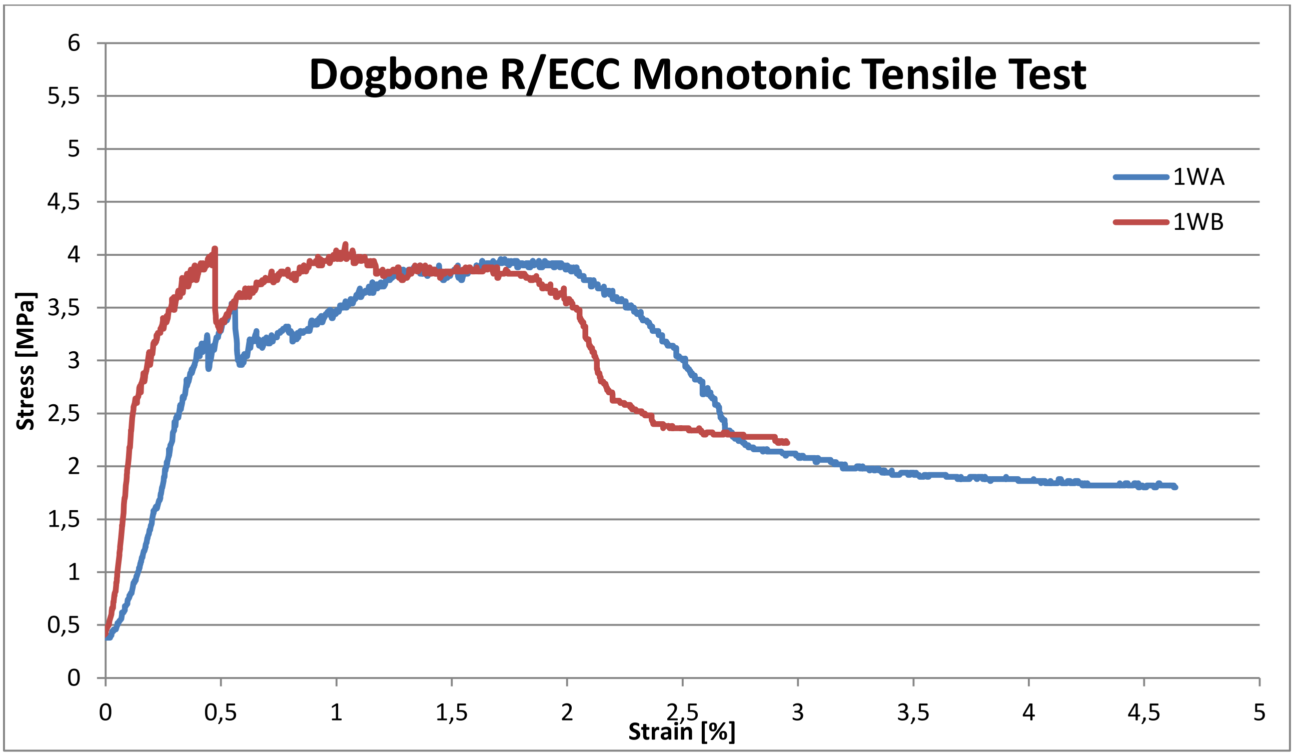

Figure 6.21: Monotonic tensile stress-strain response of Hybrid ECC specimens reinforced with 6 wires.

The cyclic tests on hybrid ECC specimens reinforced with six NiTinol single wires showed the same reduction of ductility. In fact the tensile strains reached only 2-2,5%. Ultimate tensile strength remained in the same range of the previous tests. However there is still an interesting feature that results from the contribution of the NiTinol reinforcement: in figure 6.22 it is possible to observe that the unloading stages occur at a significantly smaller steepness. In fact, when unloading from 1% strain, the specimen recovered 0,5% of the initial strain without applying any compression, and the recovered strain is much larger if the unloading stage starts from a higher initial tensile strain. From an initial tensile strain of 2%, 1% was recovered, and from an initial tensile strain of 3%, 1.5% was recovered. This effect in part reveals the self-recentring capabilities that may be reached with this type of hybrid composites.

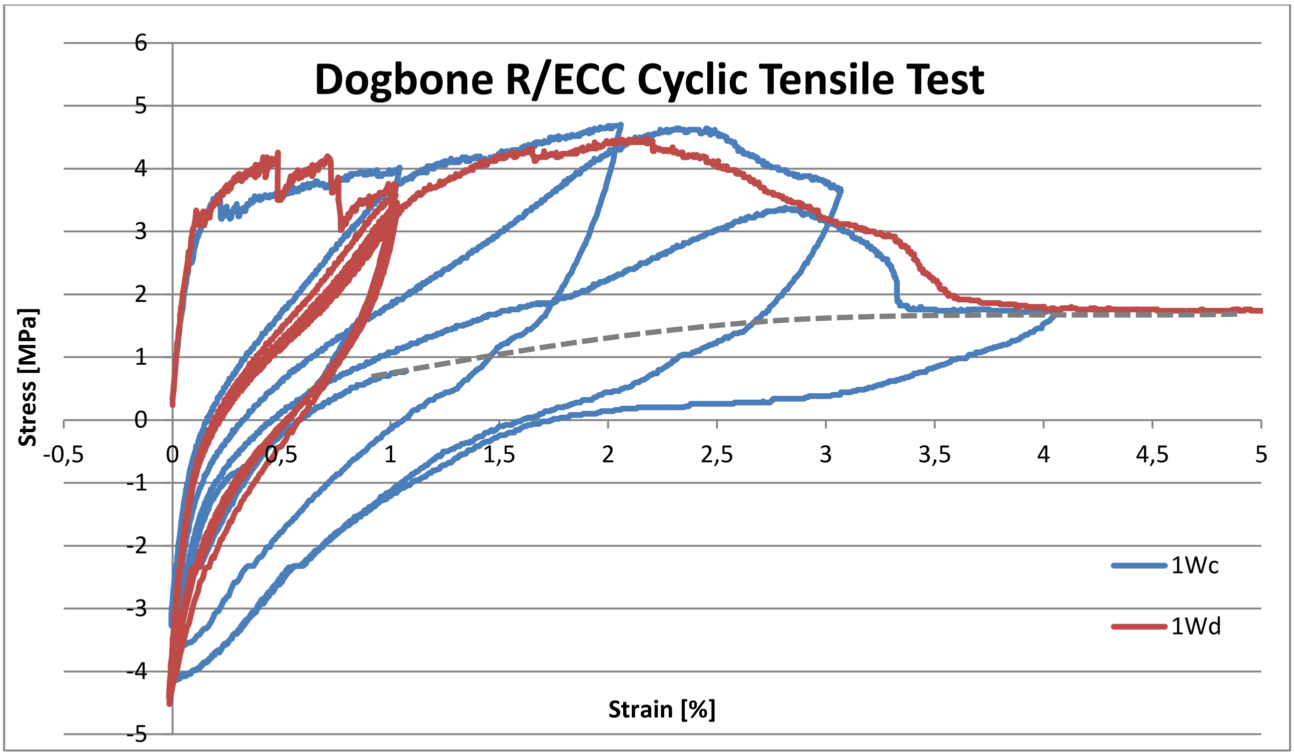

Figure 6.22: Cyclic stress-strain responses of Hybrid ECC specimens reinforced with 6 wires.

The monotonic tensile responses obtained for two hybrid ECC dogbone specimens reinforced with six twisted NiTinol wires (0,71mm diameter) are shown in figure 6.23. The responses obtained show an increase of ultimate tensile strain and stress, when compared with the specimens containing single wires and the unreinforced ECC specimens. The formation of multiple cracks is fundamental for obtaining the optimal strain-hardening behaviour, and in these two specimens the quantity of cracks formed was clearly larger than in the precedent case where the specimens have been reinforced with 6 single wires. Ultimate tensile strains between 3% and 3,5% were reached . The twisted wires have contributed to increase the bond between the wires and the matrix, and to increase the strength of the composite, reaching now 5,5 MPa.

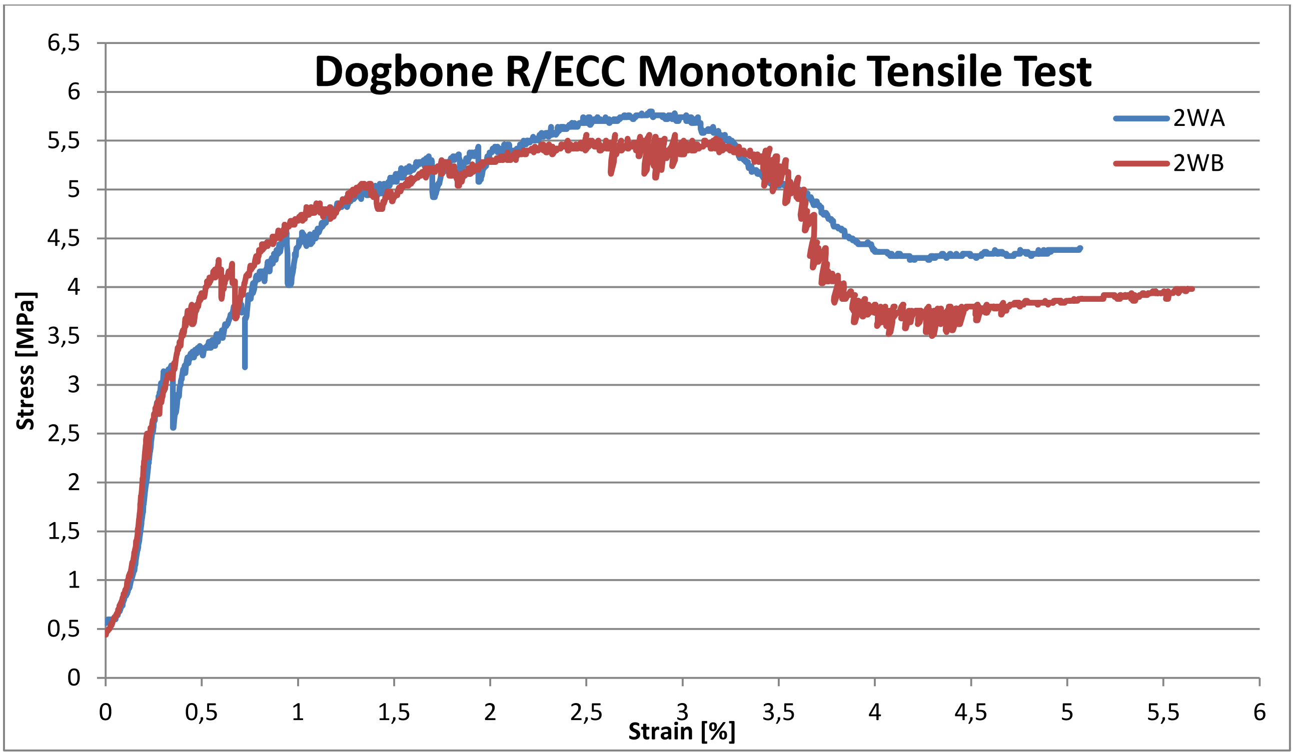

Figure 6.23: Monotonic tensile stress-strain response of Hybrid ECC specimens reinforced with 6 twisted wires.

The response obtained during the cyclic test on one hybrid ECC dogbone specimen reinforced with six twisted wires is shown in figure 6.24. Besides the features already discussed in the previous case, it was possible to observe that the strain-hardening behaviour was preserved up to a tensile strain of 3,25% and the ultimate strength exceeded 5,5 MPa. During the unloading stages the specimen was able to recover most of the initial plastic strain: when unloading from 1% strain it recovered 0,5%, when unloading from 2% strain it recovered 1% and when unloading from 3% strain it recovered 1,5%. The localization of tensile deformations led to the formation of a macro-crack near one of the edges of the specimen (figure n. 6.25), however the specimen still preserved a residual strength of 3,5 MPa provided by the contribution of the twisted wires, which even showed a slight increase. In figure 6.26 the cracking pattern obtained at the surface of the specimen during testing is shown.

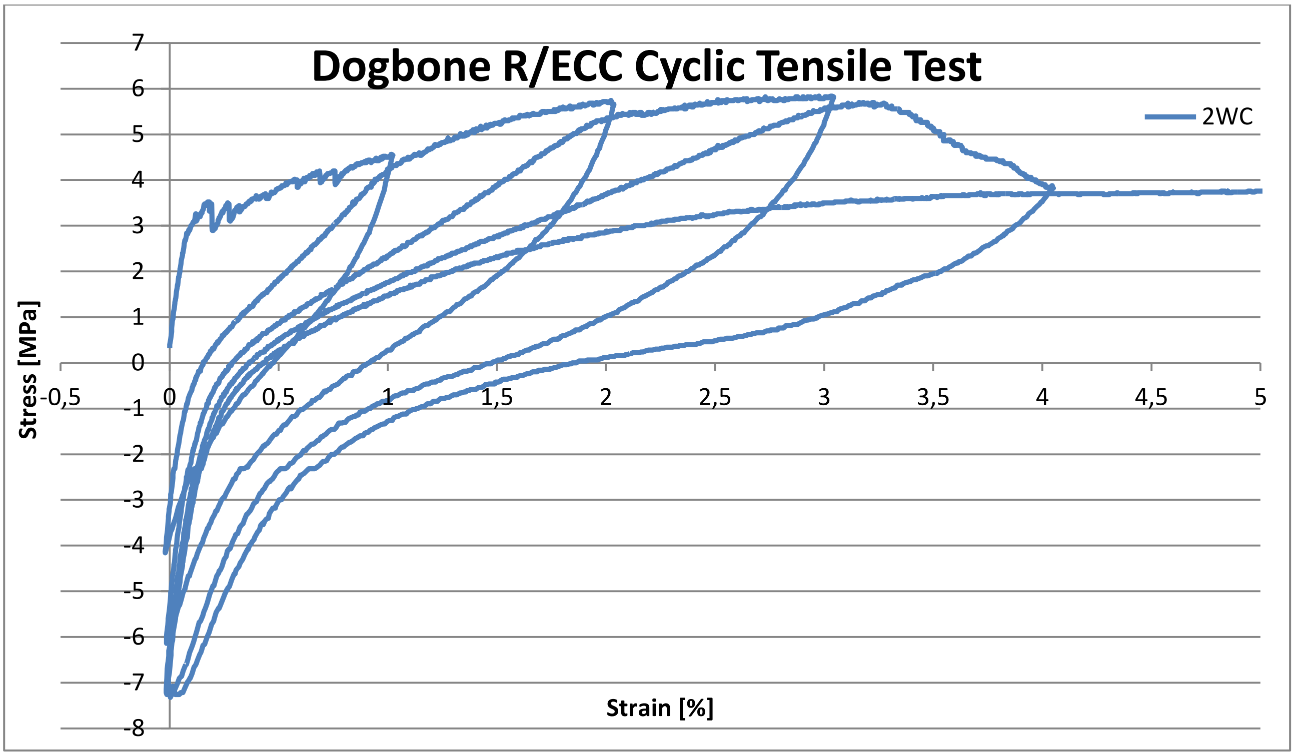

Figure 6.24: Cyclic stress-strain response of Hybrid ECC specimens reinforced with 6 twisted wires.

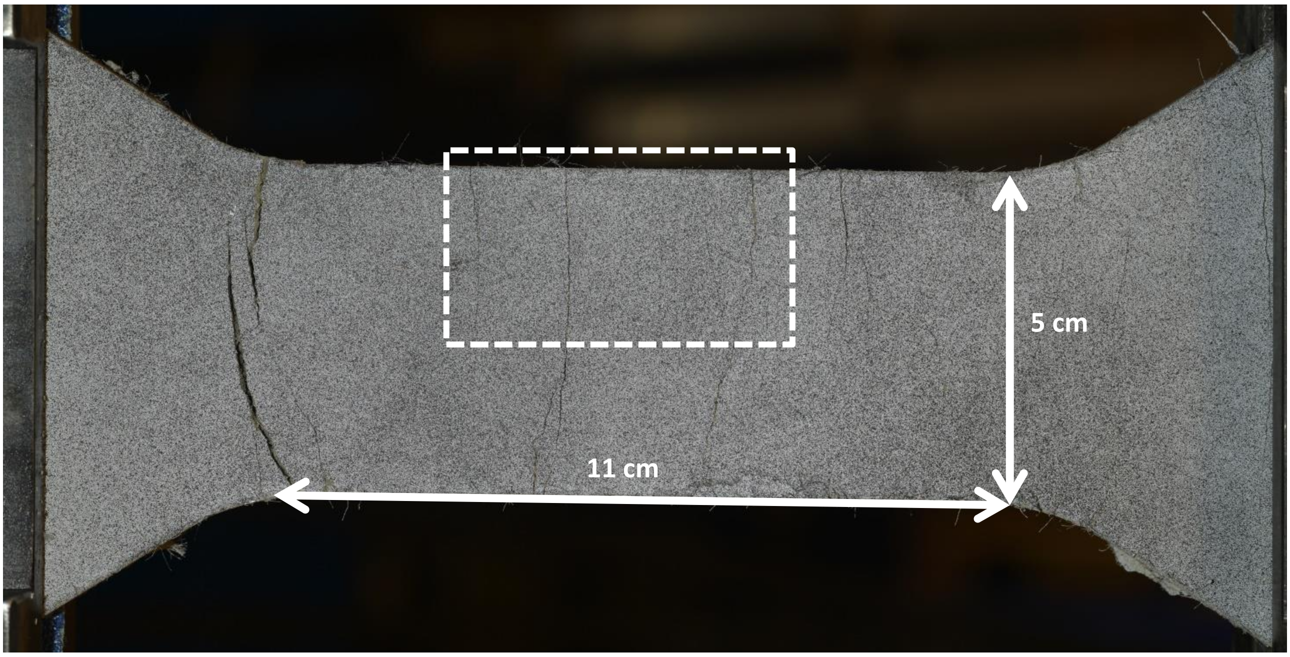

Figure 6.25: Crack pattern at the surface of specimen C.

Figure 6.26: Close-up of the crack pattern shown in figure 6.25.

6.3 Column Scale Model

6.3.1 Aims

The final experimental test of this research concerns a scale model of a bridge column, adopting a geometry that is typical of the bridges most recently built using the balanced cantilever method by overhead or underslung movable scaffolding system. Two examples are presented in figure 6.27. The scaled model of the column was tested under horizontal cyclic loads. The purpose of this test is to compare the seismic behaviour of a typical RC column with a Shape Memory Ally reinforced ECC (SMA R/ECC) column in terms of ultimate strength, displacement capacity, damage tolerance and dissipation of energy.

Figure 6.27: Two examples of balanced cantilever method.

6.3.2 Production of the Scaled Model

In order to produce the scaled models of the conventional and the SMA R/ECC columns the subsequent steps were undertaken:

- Two dogbone specimens of “M3-4R” composite reinforced with twisted Nitinol wires were casted, according to the detailing presented in figure 6.28. The procedure followed to cast these specimens was the same as the one used to cast the specimens for tensile testing explained previously in this chapter.
- After removing the specimens from the mould these were cut and rectified in order to obtain two parallelepiped specimens 10 mm thick, 50 mm wide and 320 mm long.
- The foundation was casted using a wood mould and holders to keep the two laminar sub-columns in vertical position.
- After two days of curing, the top of the column was casted, using a plastic box as a mould.
- The model scaled column representing the conventional reinforced concrete solution was produced by following the same procedure using steel wires instead of Nitinol wires, and using the same composition of ECC but without fibres.

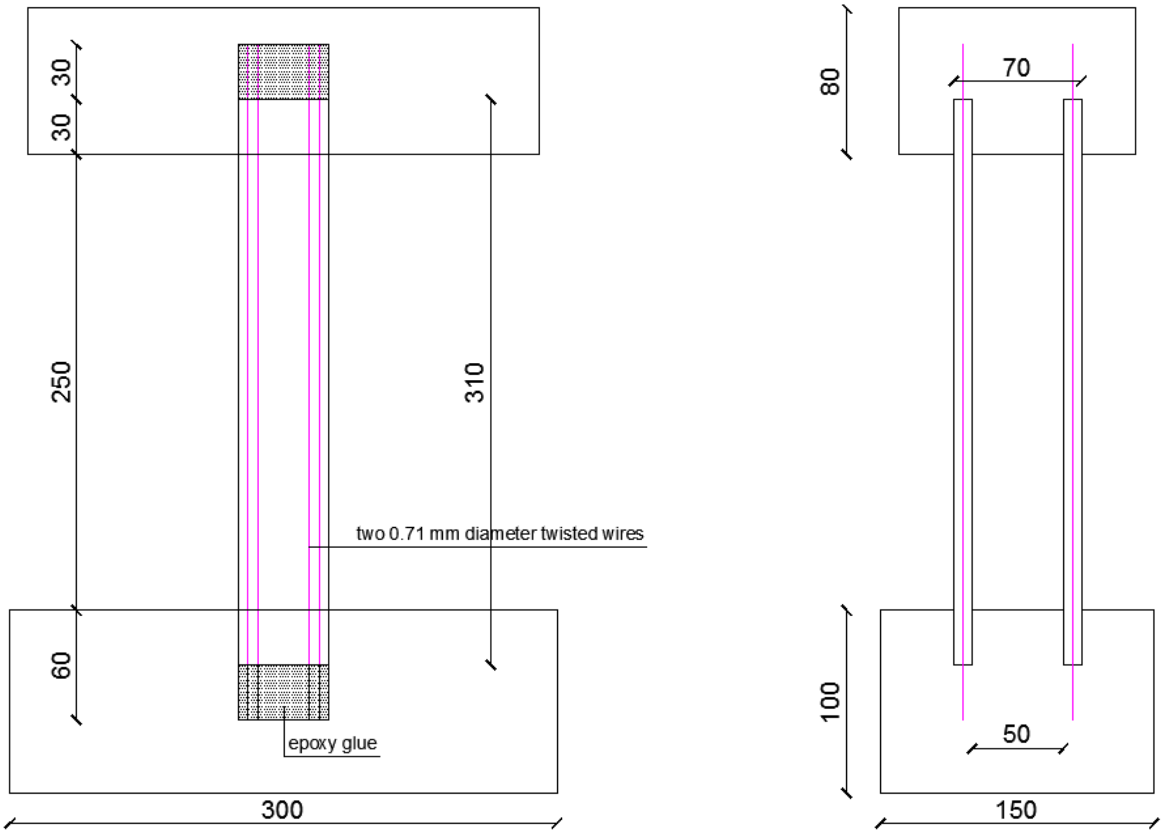

Figure 6.28: Dimensions (in millimetres) and reinforcement details of the scaled column models.

6.3.3 Testing Procedure

The tests were carried out using an actuator with a 50 KN load cell. The scale model was fixed to the actuator with a steel device, and was fixed to the frame with some bolts as is possible to see in the figure 6.29. Applied force and displacement were measured. The tests were made in displacement control with 18 sinusoidal cycles with different amplitude and frequency, reported in the table 6.1.

Figure 6.29: Column and actuator.

Equation n.14 was used to calculate the drift of the column:

$$\Delta = \frac{d}{h} \times 100 \ [14]$$

Where: Δ is the drift, d is the displacement and h is the height of the column.

Cycle	Amplitude [mm]	Period [s]	Frequency [Hz]
1	0,5	5	0,2000
2	1	10	0,1000
3	2	20	0,0500
4	3	30	0,0333
5	4	40	0,0250
6	5	50	0,0200
7	6	60	0,0167
8	8	80	0,0125
9	10	100	0,0100
10	12	120	0,0083
11	14	140	0,0071
12	16	160	0,0063
13	20	200	0,0050
14	25	250	0,0040
15	30	300	0,0033
16	35	350	0,0029
17	40	400	0,0025
18	60	600	0,0017

Table 6.1: Amplitude and frequency of the cycles.

6.3.4 Results and Discussion

The model made with the ECC reinforced with Nitinol twisted wires was the first one to be tested. As shown in figure 6.30, several cracks have formed at the base of the column during testing. After the localization of the deformations at the level of a single crack, which occurred at the eleventh cycle, the column exhibited a reduction of the carried force for three cycles, and subsequently the force increased again during the next four cycles. The column was also able to recover most of the accumulated deformation, due to the NiTinol super-elastic behaviour. The failure of the element has occurred at the seventeenth cycle. In the case of the R/C model, some cracks have formed at the base of the column and in other parts of the specimen. However these cracks suggest more the spalling of some of the concrete regions than the formation of flexure cracks. The load carried by the model sharply decreased after six cycles, due to the excessive damage at the base of the column, as shown in figure 6.31. The failure of the column occurred after four additional cycles due to the rupture of the steel wires.

Figure 6.30: Formation of several cracks near the base of the Nitinol R/ECC column.

Figure 6.31: Cracking pattern obtained near the base of R/C column.

Considering the results discussed previously and the force-drift responses obtained, which are shown in figure 6.32, the first column performed significantly better than the second column. The first column, showed the following features:

- Formation of multiple cracks near the base of the column, where the bending stresses are maximum;
- better damage tolerance and delayed localization of deformations;
- Ultimate strength more than two times higher;
- Displacement capacity four times higher;
- Less degradation at the level of the plastic hinge formed;
- Higher energy dissipation ability;
- Ability to recover the initial position even after several cycles;
- Increase of the load carrying capacity after 6% drift.

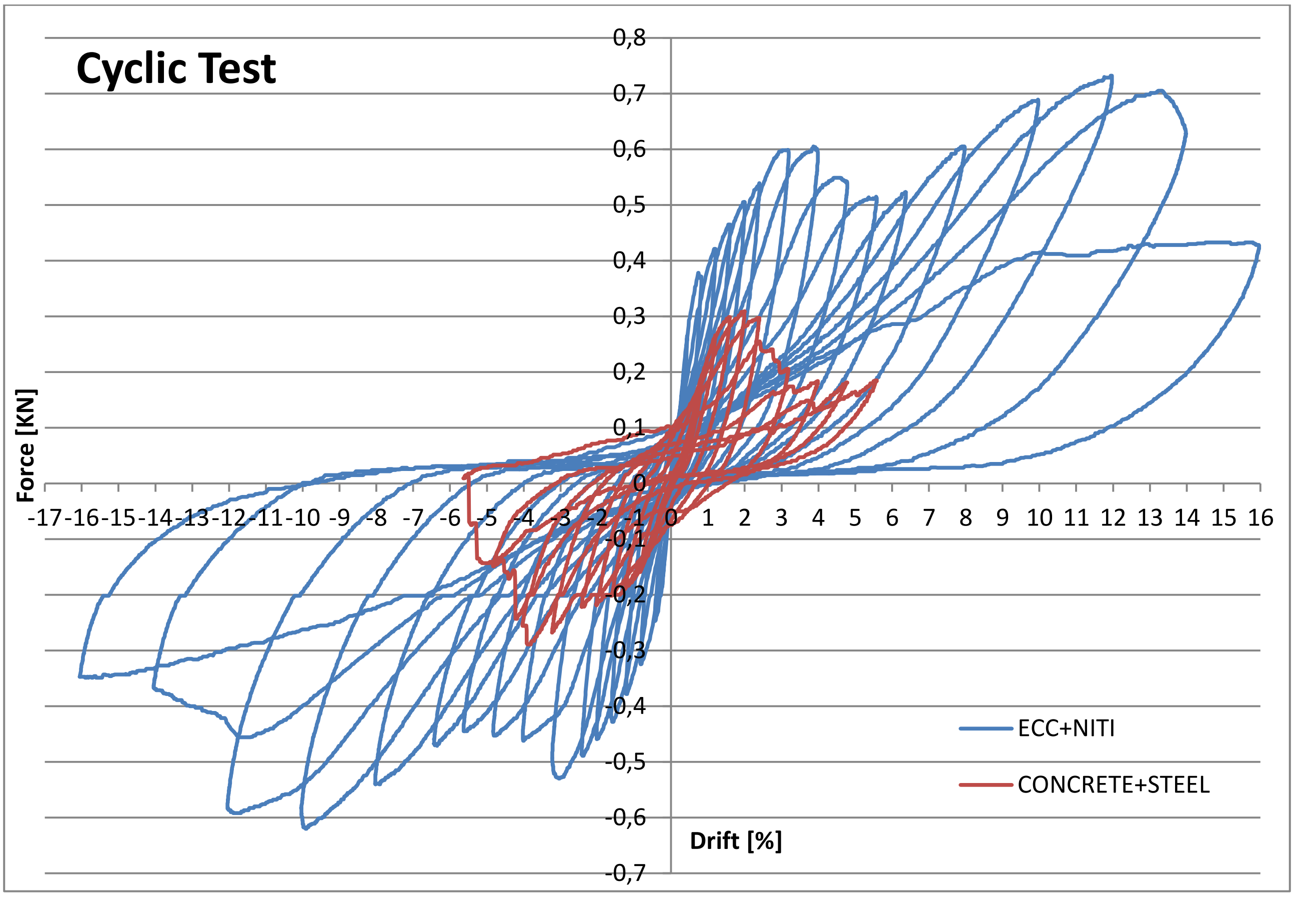

Figure 6.32: Force-drift responses of the two models.

7. Conclusions

This research was dedicated to the study of Engineered Cementitious Composites and Shape Memory Alloys, separately or combined into hybrid composites. These materials present unprecedented potential for especially demanding applications in engineering constructions, as is the case of structures subjected to severe seismic loading. In this context, these two materials have been tested separately and combined in order to better understand their behaviour and define possible innovations in civil engineering applications, both for the design of new constructions and for strengthening existing structural elements.

The experimental tests carried out on various ECC mixtures showed that the design of this material is complex and needs to consider both the fresh and the hardened properties simultaneously. In fact by varying slightly any of the components of the mixture, the fresh and hardened properties can change, reducing for example the tensile strength or changing the tensile strain hardening behaviour. In addition, the properties of the mixture depend not only on the quantities of the components, but also depend on the curing procedure, the mixing procedure and the environmental conditions, such as temperature and humidity. However, after a meticulous mixture design it is possible to obtain a composite that can undergo tensile loads, showing exceptional strain-hardening behaviour in direct tension. It was possible to obtain a composite that presented a tensile strength of about 4 MPa and an ultimate tensile strain exceeding 5%. An important observation is that this large deformation may be reduced if the composite is subtected to significant compressive stresses. In fact, cyclic tests that forced the specimens to return to their initial form, leading to significant compression stresses, resulted in the reduction of the number of cracks formed and a decrease of the deformation capacity, reducing it from 5% to 2,5-3%.
The use of ECC is recommended in a lot of civil applications such as:

- Structural elements that may be subjected to *large deformations*, because it increases the displacement capacity and avoids the spalling of the concrete in the highly deformed regions of the structure;
- Structural elements that may be subjected to *cycles of freezing and thawing,* or exposition to *chloride and alkali-silicate reaction*, because despite the large deformations reached the crack openings remain small and the fibre bridging effect contributes to increase the *durability* of the elements;
- Damaged structural elements that need to be *retrofitted*, for example by applying an external strengthening layer that can increase the confinement of the concrete, the strength, the energy dissipation ability and preserve the integrity and the ductility of the element during cyclic loading.

Tensile tests on two types of the Shape Memory Alloy Nitinol wires showed the main features of this type of material, such as the Shape Memory Effect and the Super-Elastic Effect. The Shape Memory effect is obtained when the material is loaded at a temperature lower than the Austenitic phase transition starting temperature, because most of the material is at the Martensitic phase and can recover plastic deformation when heat is applied to the material. The Super-Elastic Effect is obtained when the material is loaded at a temperature higher than the Austenitic phase transition starting temperature, because most of the material is at the Austenitic phase and shows recoverable deformation until 6% strain. Both effects can be exploited in civil engineering applications by using this material in applications such as:

- Seismic dissipators, exploiting the high energy dissipation of the Shape Memory Effect;
- Seismic isolators that can easily recover the initial position, exploiting the Super-Elastic Effect;
- Restrainers, exploiting both effects.

Two Engineered Cementitious Composites reinforced with single and twisted Nitinol wires (SMA R/ECC) have been tested in tension. The composite that included single wires did not show a significant enhancement of its mechanical properties, while the composite that included twisted wires showed an increase of tensile strength and the ability to significantly recover the accumulated deformations. Pull-out tests showed also that the adherence between these two materials is low, which is not desirable for an optimal hybrid composite effect. This explains the less impressive results obtained with the single wires reinforcement. Cyclic tests on two scaled model columns, one produced with normal steel and unreinforced cementitious matrix, and the other produced with the SMA R/ECC composite, showed that significant increases of strength, displacement capacity, damage tolerance and the ability to recover the initial position even after large displacements can be obtained.

Having in mind all these results, it is possible to draw the following conclusions:

- For future developments, having in mind the great potential of the solutions studied in this research, it is possible to *improve the mechanical properties* of the hybrid composites developed by increasing the adherence between the NiTinol reinforcement and the ECC matrix, for example using rough rebars instead of wires or treating the surface of the alloy. By promoting a better interaction between the alloy and the cementitious composite the stress transfer length is reduced, resulting in increased ductility of the composite through the formation of much more cracks. It should be possible to exceed the tensile strain value of 5%, considering the results obtained with the unreinforced ECC specimens. The tensile strength can also surpass the 6 MPa and the recovering ability of the composite can also be enhanced.
- After improving the mechanical properties of SMA R/ECC through a better interaction between the reinforcement and the matrix, this composite could be used in civil applications, both in the design of new structures and in retrofitting existing structural elements which may be subjected to large deformations or have to easily recover the initial position after extreme events. The strength, the energy dissipation capacity, the displacement capacity, the damage tolerance and in general the safety of the structures can be improved by this means, while keeping the structure functional after extreme events.